

การดูซ้ำและการเปลี่ยนของแก่นขนาดเล็บบนอนุภาคระดับนาโนเมตรของไทเทเนียมไดออกไซด์  
และผิวของไทเทเนียมไดออกไซด์คัดแปร



บทคัดย่อและแฟ้มข้อมูลฉบับเต็มของวิทยานิพนธ์ตั้งแต่ปีการศึกษา 2554 ที่ให้บริการในคลังปัญญาจุฬาฯ (CUIR)  
เป็นแฟ้มข้อมูลของนิสิตเจ้าของวิทยานิพนธ์ ที่ส่งผ่านทางบัณฑิตวิทยาลัย

The abstract and full text of theses from the academic year 2011 in Chulalongkorn University Intellectual Repository (CUIR)  
are the thesis authors' files submitted through the University Graduate School.

วิทยานิพนธ์นี้เป็นส่วนหนึ่งของการศึกษาตามหลักสูตรปริญญาวิทยาศาสตรดุษฎีบัณฑิต  
สาขาวิชาเคมี ภาควิชาเคมี  
คณะวิทยาศาสตร์ จุฬาลงกรณ์มหาวิทยาลัย  
ปีการศึกษา 2559  
ลิขสิทธิ์ของจุฬาลงกรณ์มหาวิทยาลัย

ADSORPTION AND CONVERSION OF SMALL GASES ON TiO<sub>2</sub>  
NANOPARTICLES AND SURFACES OF MODIFIED TiO<sub>2</sub>

Miss Waranyu Pipornpong



A Dissertation Submitted in Partial Fulfillment of the Requirements  
for the Degree of Doctor of Philosophy Program in Chemistry  
Department of Chemistry  
Faculty of Science  
Chulalongkorn University  
Academic Year 2016  
Copyright of Chulalongkorn University



วรัญญู พิพรรณพงษ์ : การดูดซับและการเปลี่ยนของแก๊สขนาดเล็กบนอนุภาคระดับนาโนเมตรของไทเทเนียมไดออกไซด์และผิวของไทเทเนียมไดออกไซด์ดัดแปร (ADSORPTION AND CONVERSION OF SMALL GASES ON TiO<sub>2</sub> NANOPARTICLES AND SURFACES OF MODIFIED TiO<sub>2</sub>) อ.ที่ปรึกษาวิทยานิพนธ์หลัก: ศ. ดร.วิทยา เรืองพรวิสุทธิ, หน้า.

การดูดซับของก๊าซขนาดเล็กและปฏิกิริยาของก๊าซบนผิวที่ถูกดัดแปลงของไทเทเนียมไดออกไซด์ คือผิว ZnOSL ที่อยู่บนอนาเทส (001) และผิวบนอนาเทส (001) ที่ถูกโคปด้วยแมงกานีสได้รับการศึกษาโดยวิธีดีเอฟที การคำนวณโดยใช้แบบจำลองทั้งแบบคลัสเตอร์ และแบบพีริออดิก พบว่าตำแหน่ง Ti<sub>5c</sub> และ O<sub>2c</sub> บนอนาเทส TiO<sub>2</sub> (001) มีความว่องไวต่อคลัสเตอร์ ZnOSL ปฏิกิริยาเปลี่ยนแก๊สคาร์บอนมอนอกไซด์ด้วยแก๊สออกซิเจนเกิดเป็นแก๊สคาร์บอนไดออกไซด์บนคอมโพสิต ZnOSL/TiO<sub>2</sub> ได้รับการศึกษา นอกจากนี้คลัสเตอร์ของ ZnOSL และ ZnOSL ที่ถูกโคปด้วยโลหะทรานสิชัน และอโลหะได้ถูกศึกษาเพื่อความเข้าใจสมบัติของพื้นผิวดังกล่าว ผลการศึกษาการดูดซับของแก๊สขนาดเล็กบน Sc-ZnOSL พบการดูดซับแก๊สซัลเฟอร์ไดออกไซด์เสถียรที่สุด และการดูดซับแก๊สไดไนโตรเจนออกไซด์โครงสร้างแบบบริดจ์บน Sc-ZnOSL พบว่าช่องว่างพลังงานลดลงมากที่สุด จึงได้รับการแนะนำให้ใช้เป็นวัสดุตรวจจับแก๊สไดไนโตรเจนออกไซด์ หรือแก๊สซัลเฟอร์ไดออกไซด์ สำหรับระบบผิวอนาเทสที่ถูกโคปด้วยแมงกานีสพบว่าเพิ่มความว่องไวของการดูดซับออกซิเจน และคาร์บอนมอนอกไซด์สำหรับปฏิกิริยาเปลี่ยนแก๊สคาร์บอนมอนอกไซด์เป็นก๊าซคาร์บอนไดออกไซด์ ดังนั้นผลลัพธ์บ่งชี้ว่าผิวที่ถูกดัดแปรของอนาเทส (001) สามารถใช้สำหรับปฏิกิริยาการเปลี่ยนแก๊สคาร์บอนมอนอกไซด์ด้วยแก๊สออกซิเจนเกิดเป็นแก๊สคาร์บอนไดออกไซด์ได้

ภาควิชา เคมี

สาขาวิชา เคมี

ปีการศึกษา 2559

ลายมือชื่อนิติต .....

ลายมือชื่อ อ.ที่ปรึกษาหลัก .....

# # 5472849123 : MAJOR CHEMISTRY

KEYWORDS: DFT / ADSORPTION / GASES / ANATASE TiO<sub>2</sub> (001) / ZnOSL / ZnOSL/TiO<sub>2</sub> / Mn-DOPED TiO<sub>2</sub> (001)/ PERIODIC BOUNDARY CONDITION

WARANYU PIPORNPONG: ADSORPTION AND CONVERSION OF SMALL GASES ON TiO<sub>2</sub> NANOPARTICLES AND SURFACES OF MODIFIED TiO<sub>2</sub>. ADVISOR: PROF. VITHAYA RUANGPORNVISUTI, Dr.rer.nat., pp.

Adsorptions of small gases and their reactions on modified anatase TiO<sub>2</sub> (001) as ZnOSL supported on anatase TiO<sub>2</sub> (001), (ZnOSL/TiO<sub>2</sub>), and Mn-doped TiO<sub>2</sub> (001) surfaces have been studied by density functional theory (DFT) method. The calculation models relied on both of clusters and periodic boundary conditions (PBCs). It was found that Ti<sub>5c</sub> and O<sub>2c</sub> sites on anatase TiO<sub>2</sub> (001) are active for ZnOSL supporting. The conversion of carbon monoxide by oxygen forming carbon dioxide gas over the ZnOSL/TiO<sub>2</sub> composite was studied. Moreover, ZnOSL, transition metals, and non-metals doped-ZnOSL clusters have studied to understand the properties of their surfaces. Resulting from the study of small gases on the Sc-ZnOSL, the most stable adsorption configuration is SO<sub>2</sub> adsorption. The most decreasing of energy gap for N<sub>2</sub>O bridge-structured adsorption on Sc-ZnOSL was found. The Sc-ZnOSL used as N<sub>2</sub>O or SO<sub>2</sub> sensing material was suggested. For the system of Mn-doped anatase (001) surface, Mn-doped anatase (001) surface enhances the activity of O<sub>2</sub> pre-adsorption and CO adsorption for CO to CO<sub>2</sub> conversion. Therefore, the results indicate that modified anatase (001) surface can be used for the conversion of carbon monoxide by oxygen gas forming carbon dioxide gas reaction.

Department: Chemistry

Student's Signature .....

Field of Study: Chemistry

Advisor's Signature .....

Academic Year: 2016

## ACKNOWLEDGEMENTS

I would like to express my deep gratitude to Professor Vithaya Ruangpornvisuti, my research supervisor, for his guidance, useful critiques of this research work, and helping me overcome myself. I would also like to offer my special thanks to my coach, Professor Cristiana Di Valentin for her valuable technical support, proceeding guidance and inspiration. I would like to thank all my research committees, for their advice and insightful comments. My sincere thanks also goes to Japan Student Services Organization (JASSO) for offering me the internship opportunities in Japan Advanced Institute of Science and Technology (JAIST) with a special experience from Professor Taisuke Ozaki and Dr. Chi-Cheng Lee. I would like to thank for financial support from Department of Chemistry, Chulalongkorn University providing my short-term research visitor scholarship at Nanyang Technological University (NTU) in the research group of Professor Hajime Hirao. My grateful thanks are also extended to Mr. Supho Phunnarungsi for his help in doing the data analysis and keeping my progress on schedule, to Ms. Benjawan Keawrukka for her cooperation, to Ms. Wiparat Hotarat, Mrs. Jiraporn Phanich, and Mr. Nontawat Ploysongsri for their valuable supports. I thank Ms. Thrissawan Traijitt and again, Mr. Supho Phunnarungsi for the sleepless nights we were working together.

Special thanks should be given to Dr. Daniele Selli, Mr. Daniele Perilli, Ms. Martina Datteo and all members in nanoqlab group for constructive supports, especially, Ms. Costanza Ronchi for all the fun we have had during my last year of PhD. life.

Last but not least, I wish to thank my family including Mr. Niti Ruengcharoen for all supports and encouragement throughout my study. A last special gratitude I give to my Ph.D. life which let me becomes enlightened the purpose of my life.

## CONTENTS

	Page
THAI ABSTRACT .....	iv
ENGLISH ABSTRACT.....	v
ACKNOWLEDGEMENTS .....	vi
CONTENTS.....	vii
LIST OF TABLES .....	xi
LIST OF FIGURES .....	xiii
LIST OF ABBREVIATIONS AND SYMBOLS .....	xx
CHAPTER I INTRODUCTION.....	1
1.1 RESEARCH BACKGROUND AND RESEARCH RATIONALE.....	3
1.1.1 TiO <sub>2</sub> .....	3
1.1.2 Anatase TiO <sub>2</sub> (001) surface .....	5
1.1.3 ZnOSL cage.....	6
1.1.4 Adsorption and catalytic properties of transition metal oxide .....	7
1.1.4.1 Type of transition metal oxide.....	7
1.1.4.2 Atomic coordination of surface .....	7
1.1.4.3 Acidity and basicity of surface .....	8
1.1.5 Doped metal oxide.....	9
1.1.5.1 LVD .....	9
1.1.5.2 HVD .....	10
1.1.5.3 SVD and FVD .....	10
1.1.6 Research rationale .....	11
1.2 OBJECTIVE .....	11
1.3 SCOPE OF DISSERTATION .....	12
1.4 EXPECTED RESULTS.....	13
CHAPTER II THEORETICAL BACKGROUND.....	14
2.1 Ab initio Calculation.....	14
2.1.1 HF Method .....	14
2.2 DFT Method .....	16

	Page
2.2.1 Hohenberg and Kohn DFT theorems ( HK DFT) .....	16
2.2.2 The Kohn–Sham DFT theorems (KS DFT) .....	17
2.2.2.1 The KS Energy .....	17
2.2.2.2 KS Equation .....	19
2.2.2.2.1 LDA .....	20
2.2.2.2.2 GGA.....	21
2.2.2.2.3 Hybrid functional.....	22
2.2.3 Basis set.....	23
2.2.3.1 Minimal basis set.....	23
2.2.3.2 Split–valence basis set.....	23
2.2.4 Polarization function .....	24
2.2.5 Diffuse function.....	24
2.2.6 Effective core pseudopotential (ECP) .....	24
<b>CHAPTER III FIRST–PRINCIPLES INVESTIGATION OF ZnO SODALITE– LIKE CAGE BINDING ONTO TiO<sub>2</sub> (001) SURFACE AND ITS ABILITY FOR CO OXIDATION TO CO<sub>2</sub> .....</b>	<b>26</b>
3.1 ABSTRACT .....	26
3.2 INTRODUCTION .....	26
3.3 METHODOLOGY .....	27
3.4 RESULTS AND DISCUSSION.....	30
3.4.1 Binding of ZnOSL cage on TiO <sub>2</sub> surface .....	30
3.4.2 Adsorption structures of gases on the ZnOSL–TiO <sub>2</sub> and reaction profile .....	31
3.5 CONCLUSION.....	36
3.6 SUPPLEMENTARY DATA .....	37
<b>CHAPTER IV DFT INVESTIGATION ON MOLECULAR STRUCTURES OF METAL AND NONMETAL–DOPED ZnO SODALITE–LIKE CAGE AND THEIR ELECTRONIC PROPERTIES .....</b>	<b>38</b>
4.1 ABSTRACT .....	38
4.2 INTRODUCTION .....	38

	Page
4.3 COMPUTATIONAL DETAILS .....	41
4.4 RESULTS AND DISCUSSION .....	43
4.4.1 Optimized structures of metal-doped ZnOSLs and their energy gaps.....	43
4.4.2 Optimized structures of nonmetal-doped ZnOSLs and their energy gaps.....	50
4.4.3 Metal and nonmetal binding for doping reactions.....	55
4.4.4 NBO charge analysis for metal- and nonmetal-doped ZnOSL.....	57
4.5 CONCLUSION.....	60
4.6 SUPPLEMENTARY DATA .....	61
<b>CHAPTER V DFT INVESTIGATION ON ADSORPTION OF DI-, TRI- AND TETRA-ATOMIC GASES ON Sc-DOPED ZnO SODALITE LIKE CAGE FOR GAS SENSING PURPOSE .....</b>	<b>67</b>
5.1 ABSTRACT .....	67
5.2 INTRODUCTION .....	67
5.3 COMPUTATIONAL DETAILS .....	69
5.4 RESULTS AND DISCUSSION .....	70
5.4.1 Structure optimizations.....	70
5.4.2 Energetics and thermodynamics.....	76
5.4.3 Density of state and gap energy .....	78
5.4.4 NBO atomic charges .....	80
5.5 CONCLUSION.....	83
5.6 SUPPLEMENTARY DATA .....	84
<b>CHAPTER VI MECHANISM OF CO CONVERSION TO CO<sub>2</sub> OVER THE Mn- DOPED TiO<sub>2</sub> (001) SURFACE UNDER O<sub>2</sub> ATMOSPHERE .....</b>	<b>86</b>
6.1 ABSTRACT .....	86
6.2 INTRODUCTION .....	86
6.3 COMPUTATIONAL DETAILS .....	87
6.4 RESULTS AND DISCUSSION .....	88
6.4.1 Bulk structure of anatase TiO <sub>2</sub> .....	88
6.4.2 The TiO <sub>2</sub> (001) and Mn-doped surfaces .....	88

	Page
6.4.3 Adsorption of adsorbate gases on the Mn-doped TiO <sub>2</sub> surface .....	91
6.4.3.1 Adsorption of oxygen on the Mn-doped TiO <sub>2</sub> surface .....	91
6.4.3.2 Adsorption of CO on the Mn-doped TiO <sub>2</sub> and oxygen-pre- adsorbed Mn-doped TiO <sub>2</sub> surfaces.....	95
6.4.4 The mechanism of the CO oxidation by O <sub>2</sub> to CO <sub>2</sub> on the Mn-TiO <sub>2</sub> .....	95
6.5 CONCLUSION.....	100
CHAPTER VII CONCLUSIONS.....	101
REFERENCES .....	103
VITA.....	119



## LIST OF TABLES

		<b>Page</b>
<b>Table 1.1</b>	Structural parameters of anatase and rutile TiO <sub>2</sub> .....	4
<b>Table 3.1</b>	Binding of the ZnOSL cage onto the TiO <sub>2</sub> (001) surface to afford [ZnOSL/TiO <sub>2</sub> ], its reaction for CO oxidation to CO <sub>2</sub> , and all related adsorption reactions .....	33
<b>Table 4.1</b>	Energy gaps, energetics and dipole moment of undoped, metal- and nonmetal-doped ZnOSLs, computed at the B3LYP/LanL2DZ level of theory .....	48
<b>Table 4.2</b>	Energy gaps, energetics and dipole moment of high-spin undoped, metal- and nonmetal-doped ZnOSLs, computed at the B3LYP/LanL2DZ level of theory .....	49
<b>Table 4.3</b>	Energetic and thermodynamic properties of dopant atoms binding to Zn <sub>v</sub> of [ZnOSL + Zn <sub>v</sub> ] for metal doping and O <sub>v</sub> of [ZnOSL + O <sub>v</sub> ] for nonmetal doping, computed at the B3LYP/LanL2DZ level of theory .....	56
<b>Table 4.4</b>	Selected NBO charges (in e) of metal- and nonmetal-doped ZnOSLs, computed at the B3LYP/LanL2DZ level of theory ...	58
<b>Table 4.5</b>	Selected NBO charges (in e) of high-spin metal- and nonmetal-doped ZnOSLs, computed at the B3LYP/LanL2DZ level of theory .....	59
<b>Table S4.1</b>	Selected geometrical data for the metal-doped ZnOSLs, computed at the B3LYP/LanL2DZ level of theory .....	63
<b>Table S4.2</b>	Selected geometrical data for the undoped and nonmetal-doped ZnOSLs, computed at the B3LYP/LanL2DZ level of theory .....	66

	<b>Page</b>
<b>Table 5.1</b> The shortest bond–distances between gas atoms and adsorption atom of the Sc–doped ZnOSL .....	75
<b>Table 5.2</b> Energy gaps, adsorption energies and thermodynamic quantities of gas adsorptions on Sc–doped ZnOSL, computed at the B3LYP/GEN level of theory .....	77
<b>Table 5.3</b> NBO charges of diatomic gases atoms, atoms nearby adsorption area of the Sc–doped ZnOSL and partial charge transfer (PCT) of Sc and neighboring Zn atom, computed at the B3LYP/GEN level of theory .....	81
<b>Table 5.4</b> NBO charges of polyatomicgases atoms, atoms nearby adsorption area of the Sc–doped ZnOSL and partial charge transfer (PCT) of Sc and neighboring Zn atom, computed at the B3LYP/GEN level of theory .....	82
<b>Table 6.1</b> Lattice parameters of the anatase TiO <sub>2</sub> crystals based (I41/amd space group), compared with other computed and observed results .....	93
<b>Table 6.2</b> The adsorption energies ( $\Delta E_{\text{ads}}$ ) of gas adsorbed and co–adsorbed on un– and Mn–doped TiO <sub>2</sub> (001) surfaces .....	94

## LIST OF FIGURES

		<b>Page</b>
<b>Figure 1.1</b>	Structures of <b>(a)</b> anatase and <b>(b)</b> rutile TiO <sub>2</sub> .....	4
<b>Figure 1.2</b>	Structures of <b>(a)</b> clean (101) and <b>(b)</b> (001) surfaces. Ti and O atoms are represented by grey and red spheres, with six-fold Ti, five-fold Ti, three-fold O and two-fold O denoted as Ti <sub>6c</sub> , Ti <sub>5c</sub> , O <sub>3c</sub> , and O <sub>2c</sub> respectively .....	5
<b>Figure 1.3</b>	B3LYP/LanL2DZ-optimized structure of the ZnOSL cage. Bond lengths and angles are in Å and degree, respectively .....	6
<b>Figure 3.1</b>	The molecular structures optimized using the periodic slab model for <b>(a)</b> the anatase TiO <sub>2</sub> (001) surface and <b>(b)</b> the ZnOSL cage adsorbed onto the TiO <sub>2</sub> (001) surface. Left, middle, and right are top, side, and front views, respectively. For clarity, sketch drawing for the top view of ZnOSL on the TiO <sub>2</sub> (001) surface is also shown at the left. Bond lengths are in Å .....	29
<b>Figure 3.2</b>	Potential energy profiles for (a) association of ZnOSL cage onto anatase TiO <sub>2</sub> (001) surface and (b) conversion reaction of CO + O <sub>2</sub> to CO <sub>2</sub> on the ZnOSL/TiO <sub>2</sub> . Bond lengths are in Å. Relative energies are in kcal/mol .....	34
<b>Figure 3.3</b>	Potential energy profile for stepwise adsorption of CO <sub>2</sub> onto ZnOSL surface of ZnOSL/TiO <sub>2</sub> . Bond lengths are in Å. Relative energies are in kcal/mol .....	35
<b>Figure S3.1</b>	The optimized structures of <b>(a)</b> O atom and <b>(b)</b> O <sub>2</sub> molecule adsorbed onto ZnOSL surface of the ZnOSL/TiO <sub>2</sub> . Left and right images are top and front views, respectively .....	37

<b>Figure 4.1</b>	The B3LYP/LanL2DZ-optimized structures of (a) Sc-, (b) Ti-, (c) V-, (d) Cr-, (e) Mn-, (f) Fe-, (g) Co-, (h) Ni-, (i) Cu-doped ZnOSLs, (j) undoped ZnOSL, (k) Pd-, (l) Ag-, (m) Pt- and (n) Au-doped ZnOSLs. The NBO charges for selected atoms are presented in e. a-j, k and l, and m and n are the fourth, fifth and sixth rows transition metal doping structures, respectively. All the metal-doped ZnOSLs are shown based on the periodic table as noted on the bottom left side .....	44
<b>Figure 4.2</b>	Plots of frontier orbitals of the low-spin (a) Sc-, (b) Ti-, (c) V-, (d) Cr-, (e) Mn-, (f) Fe-, (g) Co-, (h) Ni-, (i) Cu-doped ZnOSLs, (j) undoped ZnOSL, (k) Pd-, (l) Ag-, (m) Pt- and (n) Au-doped ZnOSLs. All the orbitals of metal-doped ZnOSLs are shown at the same positions of their corresponding structures shown in <b>Figure 4.1</b> .....	45
<b>Figure 4.3</b>	DOSs of the low-spin (a) Sc-, (b) Ti-, (c) V-, (d) Cr, (e) Mn-, (f) Fe-, (g) Co-, (h) Ni-, (i) Cu-doped ZnOSLs, (j) undoped ZnOSL, (k) Pd-, (l) Ag-, (m) Pt- and (n) Au-doped ZnOSLs. All the DOSs of metal-doped ZnOSLs are shown at the same positions of their corresponding structures shown in <b>Figure 4.1</b> .....	46
<b>Figure 4.4</b>	Plots of energy gaps of (a) the low-spin (-□-) and high-spin (-○-) metal-doped ZnOSLs and (b) Gibbs free energy changes of the binding of metal dopant to Zn vacancy of the low-spin (-□-) and high-spin (-○-) Zn vacancy defect surfaces of ZnOSLs .....	50

	<b>Page</b>
<b>Figure 4.5</b> B3LYP/LanL2DZ-optimized structures of the low-spin <b>(a)</b> B-, <b>(b)</b> C-, <b>(c)</b> N-doped ZnOSLs, <b>(d)</b> undoped ZnOSL, <b>(e)</b> Al-, <b>(f)</b> Si-, <b>(g)</b> P-, <b>(h)</b> Ga- and <b>(i)</b> Ge-doped ZnOSLs. The NBO charges for selected atoms are presented in e. All the nonmetal-doped ZnOSLs are shown based on the periodic table as noted on the bottom right side .....	51
<b>Figure 4.6</b> Plots of the frontier orbitals of the low-spin <b>(a)</b> B-, <b>(b)</b> C-, <b>(c)</b> N-doped ZnOSLs, <b>(d)</b> undoped ZnOSL, <b>(e)</b> Al-, <b>(f)</b> Si-, <b>(g)</b> P-, <b>(h)</b> Ga- and <b>(i)</b> Ge-doped ZnOSLs. Left and right views are their HOMO and LUMO, respectively. All the orbitals of nonmetal-doped ZnOSLs are shown at the same positions of their corresponding structures shown in <b>Figure 4.5</b> .....	52
<b>Figure 4.7</b> DOSs of the low-spin <b>(a)</b> B-, <b>(b)</b> C-, <b>(c)</b> N-doped ZnOSLs, <b>(d)</b> undoped ZnOSL, <b>(e)</b> Al-, <b>(f)</b> Si-, <b>(g)</b> P-, <b>(h)</b> Ga- and <b>(i)</b> Ge-doped ZnOSLs. All the DOSs of nonmetal-doped ZnOSLs are shown at the same positions of their corresponding structures shown in <b>Figure 4.5</b> .....	53
<b>Figure 4.8</b> Plots of energy gaps of <b>(a)</b> the low-spin (–□–) and high-spin (–○–) nonmetal-doped ZnOSLs and <b>(b)</b> Gibbs free energy changes of the binding of nonmetal dopant to O vacancy of the low-spin (–□–) and high-spin (–○–) O-vacancy defect surfaces of ZnOSLs .....	54
<b>Figure S4.1</b> Plots of frontier orbitals of the high-spin <b>(a)</b> Sc-, <b>(b)</b> Ti-, <b>(c)</b> V-, <b>(d)</b> Cr-, <b>(e)</b> Mn-, <b>(f)</b> Fe-, <b>(g)</b> Co-, <b>(h)</b> Ni-, <b>(i)</b> Cu-doped ZnOSLs, <b>(j)</b> undoped ZnOSL, <b>(k)</b> Pd-, <b>(l)</b> Ag-, <b>(m)</b> Pt- and <b>(n)</b> Au-doped ZnOSLs. All the orbitals of metal-doped ZnOSLs are shown at the same positions of their corresponding structures shown in <b>Figure 4.1</b> .....	61

	<b>Page</b>
<b>Figure S4.2</b> DOSs of the high-spin (a) Sc-, (b) Ti-, (c) V-, (d) Cr-, (e) Mn-, (f) Fe-, (g) Co-, (h) Ni-, (i) Cu-doped ZnOSLs, (j) undoped ZnOSL, (k) Pd-, (l) Ag-, (m) Pt- and (n) Au-doped ZnOSLs. All the DOSs of metal-doped ZnOSLs are shown at the same positions of their corresponding structures shown in <b>Figure 4. 1</b> .....	62
<b>Figure S4.3</b> Plots of the frontier orbitals of the high-spin (a) B-, (b) C-, (c) N-doped ZnOSLs, (d) undoped ZnOSL, (e) Al-, (f) Si-, (g) P-, (h) Ga- and (i) Ge-doped ZnOSLs. Left and right views are their HOMO and LUMO, respectively. All the orbitals of non metal-doped ZnOSLs are shown at the same positions of their corresponding structures shown in <b>Figure 4. 5</b> .....	64
<b>Figure S4.4</b> DOSs of the high-spin (a) B-, (b) C-, (c) N-doped ZnOSLs, (d) undoped ZnOSL, (e) Al-, (f) Si-, (g) P-, (h) Ga- and (i) Ge-doped ZnOSLs. All the DOSs of non metal-doped ZnOSLs are shown at the same positions of their corresponding structures shown in <b>Figure 4. 5</b> .....	65
<b>Figure 5.1</b> The B3LYP/GEN-optimized structures of (a) Sc-doped ZnOSL, their adsorption structures with (b) H <sub>2</sub> (toward Sc), (c) H <sub>2</sub> (toward O), (d) N <sub>2</sub> (toward Sc), (e) N <sub>2</sub> (toward Zn), (f) O <sub>2</sub> (toward Sc) and (g) O <sub>2</sub> (toward Zn). Plots for their density of states are located beside their images. NBO atomic charges are in parentheses. Bond distances are in Å. ....	71

	<b>Page</b>
<b>Figure 5.2</b>	72
<p>The B3LYP/GEN-optimized structures of the Sc-doped ZnOSL adsorption with (a) CO (pointing C toward Sc), (b) CO (O toward Sc), (c) CO (C toward Zn), (d) CO (O toward Zn), (e) NO (N toward Sc), (f) NO (NO bond perpendicular to Sc), (g) NO (O toward Sc) and (h) NO (N toward Zn). Plots for their density of states are located beside their images. NBO atomic charges are in parentheses. Bond distances are in Å .....</p>	
<b>Figure 5.3</b>	73
<p>The B3LYP/GEN-optimized structures of the Sc-doped ZnOSL adsorption with (a) N<sub>2</sub>O (pointing O toward Sc and N toward Zn), (b) N<sub>2</sub>O (N toward Sc), (c) N<sub>2</sub>O (O toward Zn and N toward Sc), (d) N<sub>2</sub>O (N toward Zn), (e) NO<sub>2</sub> (O toward Sc and O' toward Zn), (f) NO<sub>2</sub> (O toward Sc), (g) NO<sub>2</sub> (N toward Zn). Plots for their density of states are located beside their images. NBO atomic charges are in parentheses. Bond distances are in Å .....</p>	
<b>Figure 5.4</b>	74
<p>The B3LYP/GEN-optimized structures of the Sc-doped ZnOSL adsorption with (a) H<sub>2</sub>O (O toward Sc), (b) H<sub>2</sub>O (O toward Zn), (c) CO<sub>2</sub> (O toward Sc), (d) CO<sub>2</sub> (C–O bond somewhat parallel to Sc–O bond, O toward Sc and C toward O), (e) CO<sub>2</sub> (C–O bond somewhat parallel to Zn–O bond, O toward Zn and C toward O), (f) SO<sub>2</sub> (O toward Sc and other O toward Zn), (g) SO<sub>2</sub> (O toward Sc), (h) SO<sub>2</sub> (O toward Zn), (i) NH<sub>3</sub> (N toward Sc), (j) NH<sub>3</sub> (N toward Zn). Plots for their density of states are located beside their images. NBO atomic charges are in parentheses. Bond distances are in Å .....</p>	
<b>Figure 5.5</b>	78
<p>Free energy profile of adsorptions of small gas over the Sc-doped ZnOSL. Short symbols indicate atomic site(s) of the Sc-doped ZnOSL of which full notations are defined in <b>Table 5.1</b></p>	

	<b>Page</b>
<b>Figure 5.6</b> Changes in energy gaps (in %) of the Sc-doped ZnOSL while each gas is adsorbed. Adsorption sequences correspond to data tabulated in <b>Table 5.2</b> .....	79
<b>Figure S5.1</b> Plot of frontier orbitals' energies against adsorption structures of Sc-doped ZnOSL with di-atomic gases. HOMO-LUMO gaps are compared with the clean Sc-doped ZnOSL .....	84
<b>Figure S5.2</b> The B3LYP/GEN-optimized structures of the Sc-doped ZnOSL adsorption with (a) CO (pointing C toward Sc), (b) CO (O toward Sc), (c) CO (C toward Zn), (d) CO (O toward Zn), (e) NO (N toward Sc), (f) NO (NO bond perpendicular to Sc), (g) NO (O toward Sc) and (h) NO (N toward Zn). Plots for their density of states are located beside their images. NBO atomic charges are in parentheses. Bond distances are in Å .....	85
<b>Figure 6.1</b> The optimized-structures of (a) un-doped and (b) Mn-doped anatase TiO <sub>2</sub> (001) surfaces modeled by (2 × 3) slab of nine layers, containing altogether 18 Ti and 36 O atoms. Top and side views are shown at the top and bottom images, respectively .....	90
<b>Figure 6.2</b> The adsorption structures of O <sub>2</sub> on Mn-doped TiO <sub>2</sub> surface as (a) V-shape configuration (O <sub>2</sub> <sup>V</sup> /Mn-TiO <sub>2</sub> ) and (b) I-shape configuration (O <sub>2</sub> <sup>I</sup> /Mn-TiO <sub>2</sub> ). Their relative energies (ΔE <sub>rel</sub> ) are in kcal/mol and bond distances are in Å. Top and side views are shown at the top and bottom images, respectively ....	92
<b>Figure 6.3</b> Potential energy profile for CO oxidation to CO <sub>2</sub> on V-shape oxygen-pre-adsorbed on the Mn-TiO <sub>2</sub> (001) (O <sub>2</sub> <sup>V</sup> /Mn-TiO <sub>2</sub> ). Potential energies are in kcal/mol and bond distances are in Å. Top and side views are shown at the top and bottom images, respectively .....	97

	<b>Page</b>
<b>Figure 6.4</b> Potential energy profile for CO oxidation to CO <sub>2</sub> on I-shape oxygen-pre-adsorbed on the Mn-TiO <sub>2</sub> (001) (O <sub>2</sub> <sup>I</sup> /Mn-TiO <sub>2</sub> ). Potential energies are in kcal/mol and bond distances are in Å. Top and side views are shown at the top and bottom images, respectively .....	99



## LIST OF ABBREVIATIONS AND SYMBOLS

TiO <sub>2</sub>	Titanium dioxide
ZnO	Zinc oxide
Anatase TiO <sub>2</sub> (001)	Anatase titanium dioxide plane (001)
ZnOSL	Zinc oxide sodalite cage
PBCs	Periodic boundary conditions
DFT	Density functional theory
Ti <sub>6c</sub>	Six-fold coordinated titanium atom
Ti <sub>5c</sub>	Five-fold coordinated titanium atom
O <sub>3c</sub>	Three-fold coordinated oxygen atom
O <sub>2c</sub>	Two-fold coordinated oxygen atom
Zn <sub>3c</sub>	Three-fold coordinated zinc atom
$E_g$	Band gap energy
B3LYP	Becke's three-parameter exchange and Lee-Yang-Parr correlation hybrid functional
LVD	Low-valence dopant
HVD	High-valence dopant
SVD	Same-valence dopant
FVD	Flexible -valence dopant
ZnOSL/TiO <sub>2</sub>	ZnOSL supported on anatase TiO <sub>2</sub> (001) surface
PBE	Perdew-Burke-Ernzerh of exchange correlation functional
$\Delta E_{ads}$	Adsorption energy
DOS	Electronic density of state

Eq.	Equation
$\Delta E_{\text{reaction}}$	Reaction energy
$\Delta E_{\text{binding}}$	Binding energy
$H$	Enthalpy
$G$	Gibbs free energy
HOMO	Highest occupied molecular orbital
LUMO	Lowest unoccupied molecular orbital
SOMO	Singly occupied molecular orbital
TZVP	Triple-zeta valence with polarization quality
Mn-TiO <sub>2</sub> (001)	Manganese doped anatase titanium dioxide plane (001)
Sc-ZnOSL	Scandium doped zinc oxide sodalite cage
$\Delta G^\circ$	Gibb's free energy
$\Delta H^\circ$	Enthalpy energy

# CHAPTER I

## INTRODUCTION

Metal oxides are the key role in many aspects of our daily life, for example gas sensors [1-4], photocatalysts [5-7], and dye-sensitized solar cells [8, 9]. During the past few decades, there has been more concerned about air pollution crisis which causes health, environmental and economic problems. Nitrogen oxide ( $\text{NO}_x$ ) and carbon monoxide (CO) are two examples of common air pollutants released from motor vehicles, electric utilities, and other industries. They are toxic and rapidly react with other chemicals forming more toxic chemicals and contributing to global warming.

Due to these problems, metal oxides, such as titanium dioxide ( $\text{TiO}_2$ ) and zinc oxide (ZnO), are very fascinating compounds using for adsorption and conversion the pollutant gases to the less toxic and/or non-toxic ones.  $\text{TiO}_2$  and ZnO are two of the most widely used metal oxide, with a wide range of material applications [7, 10-12]. They also exhibit high surface reactivity and non-toxicity [12, 13]. They are well-known within the field of semiconductors, adsorption materials, and catalysts. They are substrates for metal doping and metal oxide supporting showing important catalytic properties [14-16]. As a result of their different band gaps, metal doping and metal oxide supporting affect to the electron transfer process. The electrons can move through the element or metal oxide and easily transfer to the gas adsorbate. Due to the fact that gas adsorption process is important for catalytic process on the metal oxide catalyst surface. Their gas adsorption property is closely related to its application as catalyst [17]. Hence, doping and supporting can enhance catalytic property of metal oxide [18, 19].

As various  $\text{TiO}_2$  and ZnO structures and their different surfaces may have different adsorption and reaction abilities, anatase  $\text{TiO}_2$  and ZnO sodalite-like cage, (ZnOSL) surfaces have been selected to be investigated in this work. The reason is that anatase  $\text{TiO}_2$  surface play more catalytically active compared with other  $\text{TiO}_2$  polymorphs [20-22]. Additionally, anatase  $\text{TiO}_2$  (001) surface and ZnOSL surfaces

showed higher adsorption activities for small gases showing in prior researches [23-26].

Principally, adsorption and reaction of small gases on ZnOSL cluster model have studied to investigate the nature of novel surface. Non- and element doped-ZnOSL have been also examined. In addition, modified anatase  $\text{TiO}_2$  surface by doping element and supporting with ZnOSL have studied to give more insight in enhancement of their catalytic activity. Both of cluster and periodic boundary conditions (PBCs) models of surfaces were studied with density functional theory (DFT).

The thesis contents, based on the publications, submission and preparations, are as follows:

Chapter III: First-principles investigation of ZnO sodalite-like cage binding onto  $\text{TiO}_2$  (001) surface and its ability for CO oxidation to  $\text{CO}_2$  [27]

Chapter IV: DFT investigation on molecular structures of metal and nonmetal-doped ZnO sodalite-like cage and their electronic properties [28]

Chapter V: DFT investigation on adsorption of di-, tri- and tetra-atomic gases on Sc-doped ZnO sodalite like cage for gas sensing purpose

Chapter VI: Mechanism of CO conversion to  $\text{CO}_2$  over the Mn-doped  $\text{TiO}_2$  (001) surface under  $\text{O}_2$  atmosphere

## 1.1 RESEARCH BACKGROUND AND RESEARCH RATIONALE

### 1.1.1 TiO<sub>2</sub>

TiO<sub>2</sub> is also called as titanium (IV) oxide or Titania. The oxidation states of Ti and O are formally +4 and -2, respectively. In natural, TiO<sub>2</sub> has three main different polymorphs including anatase, rutile, and brookite. Brookite is rare in natural and difficult to synthesize in the laboratory. Brookite has been considered to be brittle, hence, it is the least studied TiO<sub>2</sub> [29]. Anatase and rutile are tetragonal, in which can be explained as chain of TiO<sub>6</sub> octahedra. In bulk TiO<sub>2</sub>, the Ti<sup>4+</sup> are six-fold coordinated (Ti<sub>6c</sub>) to O<sup>2-</sup>. However, both structures have slightly different in bonding lengths and angles because of the different arrangement of atoms in their structures as depicted in **Figure 1.1** [30]. Anatase has I4<sub>1</sub>/amd space group with cell parameters of a=b=3.785 Å and c=9.514 Å. Rutile has P4<sub>2</sub>/mnm space group with cell parameters of a=b=4.594 Å and c=2.959 Å [31]. Their structure parameters were shown in **Table 1.1**. These differences in lattice structural parameters cause different mass densities and electronic structures between them. Rutile is a major phase of TiO<sub>2</sub>, while anatase and brookite are considered to be metastable phase and less dense than rutile. However, TiO<sub>2</sub> is preferable in anatase phase rather than the rutile phase at small particle size [31-33].

According to band structure, rutile and anatase have measured band gap energy ( $E_g$ ) of 3.0, and 3.2 eV, respectively [31]. The band gap of anatase is wider than one of rutile. Nevertheless, indirect band gap of anatase exhibits higher photocatalysis activity. Moreover, surface energy of anatase is lowest compared with rutile and brookite causing anatase has stronger adsorption ability [30, 34, 35].

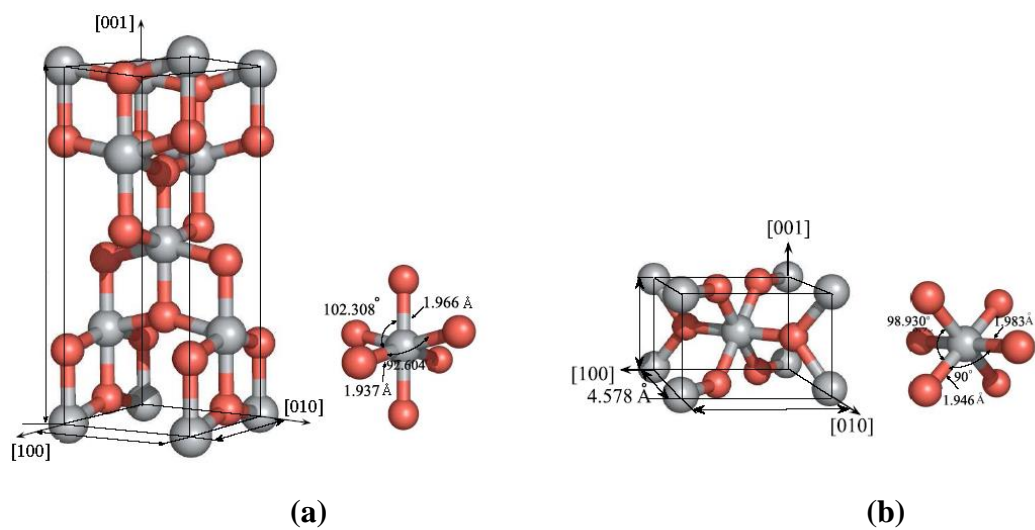


**Figure 1.1** Structures of (a) anatase and (b) rutile  $\text{TiO}_2$ .

**Table 1.1** Structural parameters of anatase and rutile  $\text{TiO}_2$

Structural parameters	Anatase	Rutile
Bravais lattice	Body-centered tetragonal	Primitive tetragonal
Space group	No. 141 $I4_1/amd$	No. 136 $P4_2/mnm$
Lattice parameters [ $\text{\AA}$ ] <sup>a</sup>		
<i>a</i>	3.785	4.594
<i>b</i>	3.785	4.594
<i>c</i>	9.514	2.959
Band gap energy [eV] <sup>b</sup>	3.2	3.0

<sup>a</sup> Taken from reference [34].

<sup>b</sup> Taken from reference [31].

### 1.1.2 Anatase TiO<sub>2</sub> (001) surface

There are two main kinds of anatase surface exposure, including (001), and (101) surfaces. Their structures were shown in

**Figure 1.2** [26, 36]. The anatase TiO<sub>2</sub> (001) surface are not stable due to excess charge and unsaturated coordination of all five-fold coordinated Ti atoms (Ti<sub>5c</sub>) and two-fold-coordinated O atoms (O<sub>2c</sub>) containing in its surface [37-39]. Therefore, it is the most reactive surface using for gas adsorption and catalytic surface [26, 40-42]. Unfortunately, anatase TiO<sub>2</sub> (001) surface is minority facet in the equilibrium state of most synthesis cases. It is thermodynamically unfavourable because of its higher surface energy (0.90 J/ m<sup>2</sup>) compared with (101) (0.44 J/m<sup>2</sup>) facets [30, 35]. But the higher surface energy demonstrated that surfaces have good performance as catalyst and gas sensing [17]. Hence, researchers attempted to the synthesis high percentages of anatase TiO<sub>2</sub> (001). For the propose of enhancement the performances of TiO<sub>2</sub>, It was successful synthesized nearly 100% exposed (001) facets [43, 44].

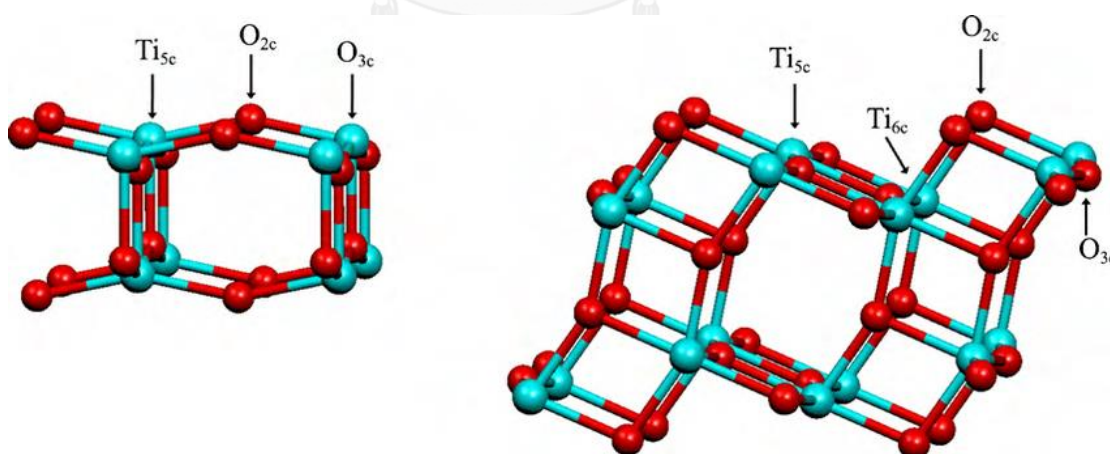


**Figure 1.2** Structures of (a) clean (101) and (b) (001) surfaces. Ti and O atoms are represented by grey and red spheres, with six-fold Ti, five-fold Ti, three-fold O and two-fold O denoted as Ti<sub>6c</sub>, Ti<sub>5c</sub>, O<sub>3c</sub>, and O<sub>2c</sub> respectively.

### 1.1.3 ZnOSL cage

ZnO nanostructures exist in several forms, such as nanotubes, nanowires, nanorods, nanoclusters, and nanoparticles. It has been found that ZnO plays an important role as gas sensor [45-47]. In 2009, Castañeda, L. prepared the ZnO nanocages and proved that ZnO nanocages is suitable for gas sensor by experimental technique [48]. In order to find out the most stable ground state geometry, the structure and thermodynamic properties of  $Zn_nO_n$  ( $n=2-16$ ) clusters was considered using DFT calculation. In case of  $n > 9$ , clusters prefer to form three-dimensional structures as cage like structures. The magic  $Zn_{12}O_{12}$  cluster have been theoretically indicated to be the most stable cluster at ground state [45, 49]. Also, it was successful synthesized since 2006 [50]. Kaewrukka, et al. stated that ZnOSL,  $Zn_{12}O_{12}$  cluster was stable. It can adsorb various gases; diatomic ( $H_2$ ,  $N_2$ ,  $O_2$ ,  $CO$ ,  $NO$ ), triatomic ( $CO_2$ ,  $N_2O$ ,  $NO_2$ ,  $H_2O$ ,  $SO_2$ ) and tetraatomic ( $NH_3$ ) gases, due to its symmetric spherical surface and high surface area [23]. It is suitable to represent spherical ZnO nanoparticle.

The coordinates of ZnOSL cage are composed of three-fold coordinated zinc atoms ( $Zn_{3c}$ ), and three-fold coordinated oxygen atoms ( $O_{3c}$ ), as shown in **Figure 1.3** [23].

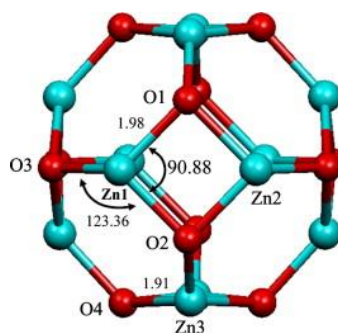


**Figure 1.3** B3LYP/LanL2DZ-optimized structure of the ZnOSL cage. Bond lengths and angles are in Å and degree, respectively.

#### 1.1.4 Adsorption and catalytic properties of transition metal oxide

Transition metal oxides comprise of transition metal bonding to oxygen in which the O atom is the more strongly electronegative component. As a result of their stability at high temperature and corrosive condition, and surface properties, they offer advantage as gas sensing and catalytic materials, especially semiconductor transition metal oxide such as TiO<sub>2</sub> and ZnO [51]. In spite of the known obvious factors leading chemical sensing and catalytic properties, it is now still complicate for choosing gas sensing and catalytic materials [52].

Numerous researchers attempt to summarize the relationship between surface properties of transition metal oxide and gas adsorbate as a rule. However, many researches probably give inconsistent results. For instance, there are well-accepted that metal oxide d<sup>5</sup>, (Fe<sub>2</sub>O<sub>3</sub>, MnO), is much higher active than the activity of d<sup>0</sup>, (TiO<sub>2</sub>, Sc<sub>2</sub>O<sub>3</sub>), and d<sup>10</sup> (ZnO, Cu<sub>2</sub>O) configurations. In contrast, metal oxide with d<sup>0</sup> and d<sup>10</sup> are more active than d<sup>5</sup> configuration [53, 54].

From many research points, we can conclude that the major factors leading the adsorption and catalytic properties of transition metal oxide are as follows,

##### 1.1.4.1 Type of transition metal oxide

The n-type semiconductor with moderate big energy gap, such as TiO<sub>2</sub> and ZnO, acts as better gas sensor. As a result of the less tendency to exchange lattice oxygen with oxygen in atmosphere, n-type semiconductor is stable [55-58].

##### 1.1.4.2 Atomic coordination of surface

The degree of coordinative unsaturated atom measures the number of bond breaking on metal oxide surface. The more degree of coordinative unsaturated atom

on surface causes bond breaking and destabilized ions. While the destabilization of the ions (particularly, transition metal ions) increases, the surface Gibb's energy increases. Correspondingly, the surface stability decreases. Hence, the more unsaturated coordination of atom on surface causes the active surface for gas adsorption and catalytic processes [59]. Different planes (facets) of transition metal oxide surface have therefore distinct adsorption and catalytic performances [37-39].

#### *1.1.4.3 Acidity and basicity of surface*

Surface of metal oxide comprises of acid–base sites. The cationic metal and anionic oxygen sites on the surface act as the Lewis acid and Lewis base sites, respectively. Cationic metal sites can accept electrons from gas adsorbate. Conversely, anionic oxygen sites can give their electrons to gas adsorbate. The catalytic activity of many metal oxide surfaces depends on the strength, the amount, and the distribution of Lewis cationic metal and anionic oxygen sites. Hence, the interaction on catalytic metal oxide surface may deal with acid–base interaction and electron transfer process. Adsorption of gas on the surface is able to perturb the adjacent sites and may cause the relaxation of the surface. In particular, chemisorption which is accompanied by charge exchange between gas adsorbate and metal oxide can change the appearance of surface charge and surface potential of metal oxide. Modification on surface, e.g. doping, can change the activity of cationic metal and anionic oxygen sites on surface as well [60-62].

Nevertheless, finding the best material does not only determining just by these factors but also other factors. Nowadays, there is no obvious rule explaining the adsorption and catalytic properties of transition metal oxide. Because of the specific performance of each oxides, researchers need to seek the most active transition metal oxide for each gas by one–to–one.

### 1.1.5 Doped metal oxide

The dopant in this thesis is foreign atom which is substituted into host metal oxide. Different dopant causes different effect on activity of metal oxide. In particular, their catalytic activity relates with the acidity or the basicity of oxides [19].

Due to its complex of definition, we have to firstly clarify the simplest definition of Lewis acid–base we use in this topic. Lewis acid is the compound that receives electron. Lewis base is the compound that donates electron. We only discuss oxidation catalytic activity of dopant substitution into binary metal oxide (with the formula  $M_xO_y$ ), not including complex oxide (e.g., perovskites).

We can classify types of dopant–oxide pair into three types which include low–valence dopant (LVD), high–valence dopant (HVD), same–valence dopant (SVD), and flexible –valence dopant (FVD).

#### 1.1.5.1 LVD

We call dopant as LVD when the valence of LVD is lower than the valence of cation the host oxide. The example in case of LVD in reducible host oxide is  $\text{La}^{3+}$  doped  $\text{CeO}_2$ . The  $\text{La}^{3+}$  dopant acts as Lewis acid when it is substituted into  $\text{Ce}^{4+}$  of  $\text{CeO}_2$ . It can activate neighboring oxygen in the  $\text{CeO}_2$  host oxide and then activated oxygen becomes to oxygen vacancy. The unpaired electron was left behind and localize at vacancy site. The oxygen vacancy is now strong Lewis base [63]. So, LVD makes doped reducible host oxide more reactive and better oxidant compared with the pristine [64-66]. Despite LVD in irreducible oxide can make oxygen vacancy on the surface, the cation in the irreducible oxide cannot lower than its formal charge. Therefore, the oxide does not have electron–accepting impurities on surface. The oxygen vacancy is still Lewis base waiting to react with Lewis acid gas in the system [67].

### 1.1.5.2 HVD

HVD is dopant which its valence is more than the valence of cation in host oxide. So, doping HVD produces excess electrons on the surface. The amount of electrons depends on the difference between valence of HVD and cation in host oxide. HVD can donate its excess electrons to reducible oxide since their metal cation can be reduced. For example,  $\text{Ti}^{4+}$  in  $\text{TiO}_2$  can be reduced to  $\text{Ti}^{3+}$  by substitution of  $\text{Ta}^{5+}$  dopant [68]. In an irreducible oxide such as  $\text{ZnO}$ , HVD such as  $\text{Al}^{3+}$  or  $\text{Ti}^{4+}$  cannot reduce  $\text{Zn}^{2+}$ . There is one excess electron localizing on Al dopant. Similarly, there are two excess electrons localizing on Ti dopant. The HVD is Lewis base in the system of irreducible oxide. It can easily adsorb Lewis acid gas such as CO [69, 70].

### 1.1.5.3 SVD and FVD

The valence of SVD is equivalent to the valence of cation in host oxide. There is no obvious rule regarding the SVD in catalysis. However, most of researches have mentioned that SVD doped oxide is efficient catalyst, such as  $\text{Sn}^{4+}$  and  $\text{Mn}^{4+}$  doped  $\text{TiO}_2$  [71, 72],  $\text{Ti}^{4+}$  and  $\text{Zr}^{4+}$  doped  $\text{CeO}_2$  [73, 74].

FVD is dopant that has several stable oxides. For example,  $\text{Nb}_2\text{O}_5$  is the most stable oxide of Nb. Likewise,  $\text{NbO}_2$  and  $\text{NbO}$  are stable. Nevertheless, a particular valence cannot be assigned to Nb oxide. However, Nb can enhance the catalytic property of  $\text{CeO}_2$  for  $(\text{NO})_x$  reduction [75]. In case of V doped  $\text{SnO}_2$ ,  $\text{V}_2\text{O}_5$  and  $\text{V}_2\text{O}_3$  are stable vanadium oxides.  $\text{V}_2\text{O}_5$  acts as HVD but  $\text{V}_2\text{O}_3$  acts as LVD when vanadium oxide is doped into  $\text{SnO}_2$ . So, it is complicate when we study the catalysis effect of FVD [76].

### 1.1.6 Research rationale

At present, reducing the concentration of pollutant gases in the atmosphere has quickly become one of the most urgent environmental issues. Using effective materials for adsorption of the pollutant gases is a type of climate engineering techniques. These techniques either directly remove toxic gases by adsorption, or alternatively seek to influence conversion reaction to remove these gases indirectly. Moreover, some natural gases are important precursors in chemical production, effective material sensor is one of the most interesting topics. To find both of gas removal and gas sensor materials, the researchers have to understand the adsorption and conversion reaction of the fundamental small gases.

Heterogeneous catalyst is the most catalyst used in these proposes. Due to the fact that the first step of heterogeneous catalyst is adsorption. Gas molecule adsorbs on the surface of catalyst. The catalyst and the molecule act as adsorbent and adsorbate, respectively. Doping  $\text{TiO}_2$  crystal with metal or non-metal can enhance its chemical reactivity, catalytic performance and many important processes such as CO and  $\text{NO}_x$  conversion [77, 78]. In addition, many researchers use both of metal and non-metal on  $\text{TiO}_2$  crystal support in the form of metal oxide nanocluster such as  $\text{Fe}_2\text{O}_3$  [79],  $\text{MnO}_x$  [80], CuO [81], and  $\text{V}_2\text{O}_5$  [82]. Lots of elements and metal oxides have not been studied clearly in some adsorption and conversion reaction mechanism.

We expect that we can study the activity of doping element and supporting metal oxide nanocluster on anatase  $\text{TiO}_2$  (001) surface by DFT approach.

## 1.2 OBJECTIVE

Adsorptions of small gases and their reactions on non- and element-doped anatase  $\text{TiO}_2$  (001), ZnOSL, and ZnOSL supported on anatase  $\text{TiO}_2$  (001) surface (ZnOSL/ $\text{TiO}_2$ ) surfaces have been investigated using DFT method. All the research studies are listed as following topics:

1. First-principles investigation of ZnOSL binding onto  $\text{TiO}_2$  (001) surface and its ability for CO oxidation to  $\text{CO}_2$
2. DFT studies of small gases adsorbed on the ZnO sodalite-like cage and its adsorption abilities
3. Mechanism of CO conversion to  $\text{CO}_2$  over the Mn-doped  $\text{TiO}_2(001)$  surface under  $\text{O}_2$  atmosphere
4. Gas adsorption over the Sc-doped zinc oxide sodalite like cage (Sc-ZnOSL) surface

### 1.3 SCOPE OF DISSERTATION

The calculation of the surface to be employed for adsorption studies can be performed by using two different approaches. ZnOSL has been investigated as the cluster model. The initial anatase  $\text{TiO}_2$  (001) surface was defined by using crystallographic concepts. All surfaces were performed by creating a single slab cutting from the bulk cell.

In this work, adsorption and reaction of small gases such as  $\text{H}_2$ ,  $\text{N}_2$ , CO, and  $\text{O}_2$  have been comprehensively studied. Adsorption abilities, in terms of binding energies of these gases, have been analyzed and reported. Scope of this research is one-by-one corresponding to the research objectives:

1. Adsorption abilities of the ZnOSL-decorated  $\text{TiO}_2$  (001) surface for adsorption of single and double molecules of CO and  $\text{CO}_2$  have been determined. The reaction mechanism of CO to  $\text{CO}_2$  interconversion on the ZnOSL-supported  $\text{TiO}_2$  (001) surface has been investigated using hybrid density functional B3LYP. All DFT calculations were performed with the CRYSTAL06 computational code.
2. Structures, electronic properties, and charge transfer of metal- and nonmetal-doped ZnOSL cage have been calculated and analyzed using hybrid density

functional B3LYP/LanL2DZ. All DFT calculations were performed with the GAUSSIAN 09 program.

3. Adsorption abilities of small gases; diatomic; H<sub>2</sub>, N<sub>2</sub>, O<sub>2</sub>, CO, NO, and polyatomic; H<sub>2</sub>O, N<sub>2</sub>O, NO<sub>2</sub>, CO<sub>2</sub>, SO<sub>2</sub>, NH<sub>3</sub> gases, on the Sc–ZnOSL surface has been investigated using B3LYP/GEN method. The LANL2DZ basis set for Zn and Sc, and 6–31G+(d,p) for all other light atoms were employed. All DFT calculations were performed with the GAUSSIAN 09 program.
4. Reaction mechanism of CO to CO<sub>2</sub> on the Mn–doped TiO<sub>2</sub> (001) surface has been investigated. All DFT calculations were performed with the CRYSTAL06 computational

#### 1.4 EXPECTED RESULTS

1. The reaction mechanism of the oxidation of CO to CO<sub>2</sub> over the ZnOSL/TiO<sub>2</sub> composite.
2. Material classification of various doped ZnOSLs into conducting and photocatalyst material based on energy gap comparison.
3. The strongest adsorption gas on the Sc–ZnOSL
4. Reaction mechanism of CO to CO<sub>2</sub> on the Mn–doped TiO<sub>2</sub> (001) surface

## CHAPTER II

### THEORETICAL BACKGROUND

Molecular modelling based on quantum mechanical (QM) method is accurate tool using for chemical investigation. QM method is categorized into semi-empirical, ab initio and DFT calculations. These methods are applied to calculate molecular structures, chemical and physical properties of chemical systems and reactions.

Here, theoretical ideas behind DFT method are briefly discussed in this chapter [83, 84]

#### 2.1 Ab initio Calculation

Ab initio method is the fundamental QM principle solving Schrödinger equation without appeal to fitting to experiment.

$$\hat{H}\Psi = E\Psi \quad (2.1)$$

where  $\hat{H}$  is Hamiltonian,  $E$  is the energy of an electron in orbital in independent-electron model, and  $\Psi$  is electronic wavefunction. Since there is no solution for many-electron systems, Hartree-Fock (HF) method is the starting point of ab initio method.

##### 2.1.1 HF Method

The first step of HF method is one-electron wavefunction approximations known as orbitals. The simplest way to represent  $\Psi$  for many-electron systems is combination of all atomic orbitals in the system as linear combination of atomic

orbitals (LCAO). The plausible approximate polyelectronic wavefunction as product of one–electron wavefunctions is written and called Hartree product

$$\Psi_0 = \psi_0(1)\psi_0(2)\psi_0(3)\dots\psi_0(n) \quad (2.2)$$

Here function  $\Psi_0$  depends on the coordinates of all electrons in the atom,  $\psi_0(1)$  is a function of the first electron,  $\psi_0(2)$  is a function of the second electron, etc., These one–electron wavefunctions.  $\psi_0(n)$  are the initial guess which can be expanded by basis set.

Due to the HF nonlinearities approximation, the equation is solved in the next step by iterative approach called self–consistent–field–procedure (SCF). The initial function,  $\Psi_0$ , is selected and solved in Schrödinger equation. The first cycle calculation gives more accurate set of orbitals as

$$\Psi_0 = \psi_0(1)\psi_0(2)\psi_0(3)\dots\psi_0(n) \quad (2.3)$$

The SCF process is continued for  $k$  cycles until self–consistency is achieved. Then, the spin orbitals and configuration state functions can be constructed by HF equation. However, HF method ignores electron correlation in the system. The electrons in the system can move independently in a mean field potential. it is difficult to perform the accurate calculations with large basis sets containing many atoms and electrons. Also, wavefunction cannot measure observable feature of molecule or atom Hence, DFT has become more popular technique using for chemical system simulation.

## 2.2 DFT Method

DFT is based on electron probability density function or electron density function. The probability to find electron in a volume element,  $dxdydz$  is designated by  $\rho(x,y,z)dxdydz$ . Owing to relationship between  $\rho(x,y,z)$  and component one-electron spatial wavefunctions,  $\Psi_i$ , the  $\Psi$  of HF is approximated as

$$\rho = \sum_{i=1}^n n_i |\Psi_i|^2 \quad (2.4)$$

### 2.2.1 Hohenberg and Kohn DFT theorems ( HK DFT)

In 1920s, E. Fermi and L. H. Thomas developed DFT theorems by expressing the energy of the chemical system with electron probability density function namely Thomas–Fermi model. This concept was confirmed by Hohenberg and Kohn so called HK DFT. The first HK DFT demonstrates that electron density function,  $F[\rho_0]$ , can determine the ground state properties functional,  $f(x)$ , e.g. energy,  $E_0$  of a many-electron system.

$$E_0 = F[\rho_0] = E[\rho_0] \quad (2.5)$$

In DFT, the electronic energy from a trial electron density,  $\rho_t$ , is the energy of the electrons moving under the nuclear potential called external potential,  $v(r)$ . The energy functional of exact ground state electron density,  $E_0$ , was stated by the second HK DFT.

$$E_v[\rho_t] \geq E[\rho_0] \quad (2.6)$$

where  $\rho_0$  is exact ground state energy according to exact electronic density.

### 2.2.2 The Kohn–Sham DFT theorems (KS DFT)

According to KS DFT, many–body problem of interacting electrons in a static external potential is assumed as non–interacting electrons moving in an effective potential. There are two main basics behind the KS DFT. The first idea is expression of the molecular energy as a sum of small term. The second idea is using the initial guess of the electron density  $\rho$  in the KS equations to calculate an initial guess of the KS orbitals. Then, KS orbitals are refined by a process that similar to HF SCF method. The final KS orbitals are used to calculate an electron density which is used to calculate the energy.

#### 2.2.2.1 The KS Energy

The ground state electronic energy is summation of kinetic energy,  $\langle T[\rho_0] \rangle$ , attraction between the nuclei and electrons,  $\langle V_{Ne}[\rho_0] \rangle$ , and electron–electron repulsion,  $\langle V_{ee}[\rho_0] \rangle$

$$E_0 = \langle T[\rho_0] \rangle + \langle V_{Ne}[\rho_0] \rangle + \langle V_{ee}[\rho_0] \rangle \quad (2.7)$$

The nucleus–electron potential energy is defined as

$$\langle V_{Ne} \rangle = \sum_{i=1}^{2n} \sum_{nucleiA} -\frac{Z_A}{r_{iA}} = \sum_{i=1}^{2n} v(r_i) \quad (2.8)$$

where  $v(r_i)$  is the external potential for the attraction between electron  $i$  and nuclei.

The density function  $\rho$  can be introduced into  $\langle V_{Ne} \rangle$  by the fact that

$$\int \Psi \sum_{i=1}^{2n} f(r_i) \Psi dt = \int \rho(r) f(r) dr \quad (2.9)$$

where  $f(r_i)$  is a function of the coordinates of the  $2n$  electrons of a system and  $\Psi$  is the total wavefunction.  $\langle V_{Ne} \rangle$  can be written as

$$\langle V_{Ne} \rangle = \int \rho_0(r) v(r_i) dr \quad (2.10)$$

The deviation of the real kinetic energy from that of the reference system is defined by

$$\Delta \langle T[\rho_0] \rangle = T[\rho_0] - T_r[\rho_0] \quad (2.11)$$

The  $\Delta \langle V_{ee} \rangle$  is the deviation of the real electron–electron repulsion energy from classical charged–cloud coulomb repulsion energy. This classical electrostatic repulsion energy is the summation of the repulsion energies for pairs of infinitesimal volume elements  $\rho(r_1)dr_1$  and  $\rho(r_2)dr_2$  separated by distance  $r_{12}$ , as

$$\Delta\langle V_{ee}[\rho_0]\rangle \equiv \langle V_{ee}[\rho_0]\rangle - \frac{1}{2} \iint \frac{\rho_0(r_1)\rho_0(r_2)}{r_{12}} dr_1 dr_2 \quad (2.12)$$

From above of all, good approximation for (2.7) is written as

$$E_0 = \int \rho_0(r)v(r)dr + \langle T[\rho_0]\rangle + \frac{1}{2} \iint \frac{\rho_0(r_1)\rho_0(r_2)}{r_{12}} dr_1 dr_2 + \Delta\langle T_r[\rho_0]\rangle + \Delta\langle V_{ee}[\rho_0]\rangle \quad (2.13)$$

The summation of last two terms is called exchange–correlation energy,  $E_{xc}$

$$E_{xc}[\rho_0] = \Delta\langle T_r[\rho_0]\rangle + \Delta\langle V_{ee}[\rho_0]\rangle \quad (2.14)$$

where  $\Delta\langle T_r\rangle$  is the kinetic correlation energy of the electrons,  $\Delta\langle V_{ee}\rangle$  is the potential correlation energy and the exchange energy.

#### 2.2.2.2 KS Equation

From the second HK theorem, KS equation is utilized by variation principle. Due to the fact that electron density of the reference system is same as that of real system, so

$$\rho_0 = \rho_r = \sum_{i=1}^{2n} |\Psi_i^{KS}(1)|^2 \quad (2.15)$$

where the  $\Psi_i^{KS}$  are the KS spatial orbital. Varying  $E_0$  which respect to the  $\Psi_i^{KS}$  subjects to the constraint that these remain orthonormal lead to the KS equation.

$$\left[ -\frac{1}{2}\nabla_i^2 - \sum_{\text{nuclei } A} \frac{Z_A}{r_{iA}} + \int \frac{\rho(r_2)}{r_2} dr_2 + v_{xc}(1) \right] \Psi_i^{KS}(1) = \varepsilon_i^{KS} \Psi_i^{KS}(1) \quad (2.16)$$

where  $\varepsilon_i^{KS}$  are the KS energy levels and  $v_{xc}(1)$  is the exchange correlation potential. The functional derivative of  $E_{xc}[\rho(r)]$  with respect to  $\rho(r)$  represents as exchange–correlation potential

$$v_{xc}(r) = \frac{\delta E_{xc}[\rho(r)]}{\delta \rho(r)} \quad (2.17)$$

The KS equation can be written as

$$\hat{h}^{KS}(1) \Psi_i^{KS}(1) = E_i^{KS}(1) \Psi_i^{KS}(1) \quad (2.18)$$

The approximated DFT for the exchange–correlation energy can be classified into the local density approximation (LDA) and generalized gradient approximation (GGA)

#### 2.2.2.2.1 LDA

The LDA exchange–correlation energy function,  $E_{xc}^{LDA}$ , can be given the same density in homogeneous electron gas model as

$$E_{xc}^{LDA} = E_{xc}^{LDA} + E_c^{LDA} \quad (2.19)$$

The correlation part,  $E_c^{LDA}$ , can be calculated by very complicated function of Vosko, Wilk, and Nusair (VWN). When the  $X\alpha$  method was developed to neglect the exchange contribution,  $E_c^{LDA}$  which is written as

$$E_{xc}^{LDA} \approx E_x^{X\alpha} = -\frac{9}{8} \left( \frac{3}{\pi} \right)^{\frac{1}{3}} \alpha \int [\rho(r)]^{\frac{4}{3}} dr \quad (2.20)$$

For one or more unpaired electrons, LDA was improved to local spin density approximation (LSDA). LSDA is unrestricted LDA method which can give better results than LDA.

#### 2.2.2.2.2 GGA

In contrast to LDA, non-local functional GGA represents the exchange-correlation functional both of electron density, and its gradient which is derivative of the density.

$$E_{xc}^{GGA}[\rho^\alpha, \rho^\beta] = \int f(\rho^\alpha(r), \rho^\beta(r), \nabla\rho^\alpha(r), \nabla\rho^\beta(r)) dr \quad (2.21)$$

The exchange-correlation energy functional can be written as summation of an exchange energy functional and correlation energy functional, both negative, i.e.

$E_{xc} = E_x + E_c$ . The  $|E_x|$  is much bigger than  $|E_c|$ . The popular functionals are Lee, Yang and Parr (LYP) and Perdew functionals.

### 2.2.2.2.3 Hybrid functional

Hybrid functional is DFT exchange–correlation energy which is improved by HF exchange calculated term but based on KS orbitals

$$E_x^{HF} = - \sum_{i=1}^n \sum_{j=1}^n \left\langle \Psi_i^{KS}(1) \Psi_j^{KS}(2) \left| \frac{1}{r_{ij}} \right| \Psi_i^{KS}(2) \Psi_j^{KS}(1) \right\rangle \quad (2.22)$$

The weighted contribution of the expression for  $E_x^{HF}$  gives a HF/DFT exchange–correlation functional. Nowadays, Becke3 LYP (B3LYP) is one of the most popular hybrid functional expressing as

$$E_{xc}^{B3LYP} = (1 - a_0 - a_x) E_x^{LSDA} + a_0 E_x^{HF} + a_x E_x^{B88} + (1 - a_c) E_c^{VWN} + a_c E_c^{LYP} \quad (2.23)$$

Here  $E_x^{LSDA}$  is the kind accurate pure LSDA,  $E_x^{HF}$  is the KS orbitals based HF exchange energy functional,  $E_x^{B88}$  is the Becke 88 exchange functional. The  $E_c^{VWN}$  is the VWN function, and  $E_c^{LYP}$  is the LYP correlation functional. The parameters give the best fit of the calculated energy to molecular atomization energies. This is thus gradient–corrected hybrid functional.

### 2.2.3 Basis set

Basis set is a set of mathematical basis functions representing the molecular orbitals. Linear combination of functions including the weights or coefficients describes molecular orbitals. It is composed of finite number of atomic orbitals within the system. This approximated molecular orbital is called LCAO approach. Moreover, the basis functions are described by the electron distribution around atom in the system.

#### 2.2.3.1 Minimal basis set

A minimal basis set is composed of one Slater functions for each inner-shell and valence-shell atomic orbitals of each atom. There are two kinds of minimal basis sets which are Slater type orbital (STO), and Gaussian type orbital (GTO). The essential idea of the minimal basis set is that one basis function for every atomic orbital is selected to describe the free atom. The most common uses are the STO-nG basis sets,  $n = 3, 4, 5,$  and  $6$ . The GTO was introduced in Gaussian product theorem.

#### 2.2.3.2 Split-valence basis set

A split-valence basis set describes two (or more) GTOs for each valence atomic orbital but only one GTO for each inner-shell (core) atomic orbital. There are many kinds of split-valence basis sets depending on the number of GTOs used for each valence atomic orbitals. For example,

#### 2.2.4 Polarization function

Polarization effect can be occurred when orbitals share qualities of its orbitals to each other. Their charge distribution causes a polarization effect because of the distortion of the shape of atomic orbital. Polarized basis sets are represented by asterisk (\*) at the end of a basis set. One asterisks (\*) or (*d*) denotes that polarization has been taken into *p* orbitals which was modified by adding a *d* orbital. Two asterisks (\*\*) or (*d,p*) denote that polarized basis set has been taken into *s* orbital which was modified by adding a *p* orbital.

For instance,  $6-31G^*$  or  $6-31G(d)$  basis set for carbon atom have *1s* function represented by six Gaussian, and inner  $2s$ ,  $2p_x$ ,  $2p_y$  and  $2p_z$  ( $2s'$ ,  $2p'_x$ ,  $2p'_y$ ,  $2p'_z$ ) function, each composed of three Gaussian, and an outer  $2s$ ,  $2p_x$ ,  $2p_y$  and  $2p_z$  ( $2s''$ ,  $2p''_x$ ,  $2p''_y$ ,  $2p''_z$ ) function, each composed of one Gaussian, and six 3d functions. That is totally 15 functions: ( $1s$ ,  $2s'$ ,  $2p'_x$ ,  $2p'_y$ ,  $2p'_z$ ,  $2s''$ ,  $2p''_x$ ,  $2p''_y$ ,  $2p''_z$ ,  $3d$ ,  $3d$ ,  $3d$ ,  $3d$ ,  $3d$ ,  $3d$ ).

#### 2.2.5 Diffuse function

There are loosely bond electrons in anion or excited atoms. They cause the energy in the tail of the wave function more important. To take responsible for this effect, diffuse functions are used to clarify the properties of the tail. Diffuse basis sets are denoted by the '+' signs. One (+) represents that *p* orbital is considered, while (++) represents that both *p* and *s* orbital are considered.

#### 2.2.6 Effective core pseudopotential (ECP)

The ECP is to replace the inner electrons of atom as one core and take account only the valence electrons. Thus, pseudopotentials are modified to the Hamiltonian. Following this approach, LanL2DZ (a split valence basis) is one of ECP basis sets which consist of double basis set and effective core potential for calculating valence

electrons and inner shell electrons, respectively. This potential is suitable for transition metals. It was confirmed with similar results compared with all electrons calculation.



# CHAPTER III

## FIRST-PRINCIPLES INVESTIGATION OF ZnO SODALITE-LIKE CAGE BINDING ONTO TiO<sub>2</sub> (001) SURFACE AND ITS ABILITY FOR CO OXIDATION TO CO<sub>2</sub>

Waranyu Pipornpong, Vithaya Ruangpornvisuti

This article has been published in Journal of Materials Science,

Volume 49, Issue 21, page 7620–7624 year: 2014.

### 3.1 ABSTRACT

The binding of ZnOSL onto the anatase TiO<sub>2</sub> (001) surface to form ZnOSL/TiO<sub>2</sub> composite was investigated using the periodic DFT–B3LYP method. The strong binding for the ZnOSL onto TiO<sub>2</sub> (001) surface to form ZnOSL/TiO<sub>2</sub> composite was found, the binding energy of which is  $-70.78$  kcal/mol. The reaction mechanism of the oxidation of carbon monoxide by oxygen to form carbon dioxide gas over the ZnOSL/TiO<sub>2</sub> composite was investigated. The reaction energies for all reaction steps are reported.

### 3.2 INTRODUCTION

The ground state of (ZnO)<sub>*n*</sub> clusters ( $n = 1-20$ ) was explored experimentally by mass spectroscopy [61]. The ground states of (ZnO)<sub>*n*</sub> clusters ( $n = 1-9$ ) [62] and their excitation states [9] were studied using DFT and time-dependent density functional theory (TDDFT) method, respectively. The optical properties of (ZnO)<sub>*n*</sub> clusters ( $n = 2-12$ ) were studied using DFT method [41]. In our previous work, the structure of ZnOSL cage, (ZnO)<sub>12</sub> cluster, and its adsorption configurations with gases H<sub>2</sub>, N<sub>2</sub>, O<sub>2</sub>, CO, NO, CO<sub>2</sub>, N<sub>2</sub>O, NO<sub>2</sub>, H<sub>2</sub>O, SO<sub>2</sub>, and NH<sub>3</sub> were studied using the DFT method. Electronic properties of all adsorption structures were investigated, and

adsorption energies ( $\Delta E_{\text{ads}}$ ) of single molecules of CO ( $\Delta E_{\text{ads}} = -10.29$  kcal/mol) and CO<sub>2</sub> ( $\Delta E_{\text{ads}} = -7.86$  kcal/mol) on the ZnOSL cage were obtained [23]. Due to adsorption data, interconversion of CO to CO<sub>2</sub> on the ZnOSL cage has interested us to study its reaction mechanism. As clean TiO<sub>2</sub> surfaces [24, 26, 85-88] and TiO<sub>2</sub>-supported metal surfaces [89-91] can adsorb and interact with CO, other metal oxides supported by TiO<sub>2</sub> surface as catalytic promoter could act as good catalyst for CO to CO<sub>2</sub> interconversion. Therefore, the ZnOSL cage immobilized on active TiO<sub>2</sub> surface, the ZnOSL-decorated TiO<sub>2</sub> surface as catalyst could facilitate the CO to CO<sub>2</sub> interconversion. Nevertheless, only a small number of works has been done on ZnO/TiO<sub>2</sub> nanocomposites and their properties. Quite a few of them have been studied such as the study of the optical band gap of the nano-hybrid TiO<sub>2</sub>/ZnO [92] and the crystalline phase of ZnO/TiO<sub>2</sub> as photocatalyst [93].

In this work, we have studied the binding of ZnOSL onto anatase TiO<sub>2</sub> (001) surface in order to immobilize the ZnOSL by TiO<sub>2</sub> (001) surface and interconversion of CO + O<sub>2</sub> to CO<sub>2</sub> on the ZnOSL-decorated TiO<sub>2</sub> (001) surface using periodic DFT computations. Therefore, adsorption abilities of the ZnOSL-decorated TiO<sub>2</sub> (001) surface for adsorption of single and double molecules of CO and CO<sub>2</sub>, and other adsorptions related with O<sub>2</sub>, in terms of adsorption and reaction energies have been determined. The reaction mechanism of CO to CO<sub>2</sub> interconversion on the ZnOSL-decorated TiO<sub>2</sub> (001) surface has been investigated, and its reaction steps have been reported.

### 3.3 METHODOLOGY

All DFT computations of two-dimensional periodic slab model have been carried out using the CRYSTAL06 computational code [94], based on the expansion of the crystalline orbitals as a linear combination of a basis set consisting of atom-centered Gaussian orbitals. The Kohn-Sham orbitals as Gaussian-type-orbital basis sets of double zeta quality as an 411(311d)G and an 8-411d11G contraction scheme have been, respectively, employed for the titanium [95] and oxygen [96] atoms on

TiO<sub>2</sub> (001) surface. Basis sets for zinc and oxygen are an 86–411d31G [97] and an 8–411d11G [95], respectively. Basis sets for carbon and oxygen atoms for adsorbent gases employed in these calculations are a 6–31d1G [98] and a 6–31d1G [98], respectively. The hybrid functional, B3LYP including Becke’s three–parameter exchange [99] and Lee–Yang–Parr correlation [100], has been employed.

Our optimized bulk lattice parameters for TiO<sub>2</sub> are  $a = 3.8192 \text{ \AA}$  and  $c = 9.6658 \text{ \AA}$ , which are quite close to the experimental results of 3.872 and 9.616  $\text{\AA}$ , respectively [101]. The Monkhorst–Pack scheme for  $8 \times 8 \times 8$  k–point mesh in the Brillouin zone was applied for anatase TiO<sub>2</sub> crystal. The anatase TiO<sub>2</sub> (001) surface was modeled by a  $(3 \times 3)$  slab of nine TiO<sub>2</sub> layers, containing altogether 27 Ti and 54 O atoms. In geometry optimizations of two–dimensional periodic slab, the two lowest TiO<sub>2</sub> layers were fixed at their bulk positions, while the positions of all Ti and O atoms were allowed to relax.

The tolerances for geometry optimization convergence have been set to the default values [94], and the coulomb–exchange screening tolerances were set to (6, 6, 6, 6, 12). All slab calculations have been performed with a Monkhorst–Pack [101] k–point grid with shrinking factors (2, 2). There are two binding sites for the anatase TiO<sub>2</sub> (001) surface: twofold–coordinated O atom (O<sub>2C</sub>) and fivefold–coordinated Ti atom (Ti<sub>5C</sub>), see **Figure 3.1(a)**. ZnOSL binds with O<sub>2C</sub> and Ti<sub>5C</sub> as shown in **Figure 3.1(b)**.

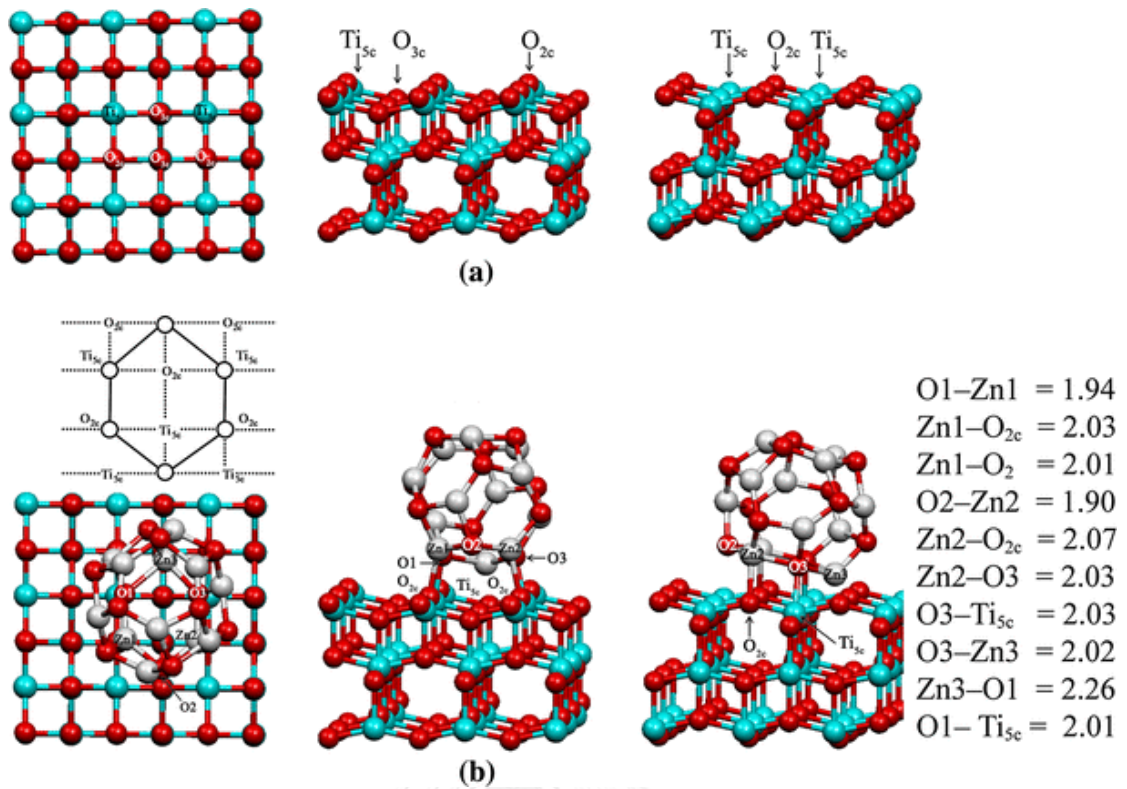


**Figure 3.1** The molecular structures optimized using the periodic slab model for (a) the anatase TiO<sub>2</sub> (001) surface and (b) the ZnOSL cage adsorbed onto the TiO<sub>2</sub> (001) surface. Left, middle, and right are top, side, and front views, respectively. For clarity, sketch drawing for the top view of ZnOSL on the TiO<sub>2</sub> (001) surface is also shown at the left. Bond lengths are in Å

The binding energy ( $\Delta E_{\text{binding}}$ ) of ZnOSL adsorbed onto TiO<sub>2</sub> (001) surface and the adsorption energies ( $\Delta E_{\text{ads}}$ ) of single molecule adsorption on the ZnOSL of ZnOSL–TiO<sub>2</sub> surface have been obtained using, (3.1) and (3.2), respectively:

$$\Delta E_{\text{binding}} = E(\text{ZnOSL-TiO}_2) - [E(\text{ZnOSL}) + E(\text{TiO}_2)] \quad (3.1)$$

where  $E(\text{ZnOSL-TiO}_2)$  is the energy of the ZnOSL–TiO<sub>2</sub>, and  $E(\text{ZnOSL})$  and  $E(\text{TiO}_2)$  are the energies of free ZnOSL and clean TiO<sub>2</sub> (001) surface, respectively.

$$\Delta E_{\text{ads}}(\text{Gas}) = E(\text{Gas}/\text{ZnOSL}-\text{TiO}_2) - [E(\text{ZnOSL}-\text{TiO}_2) + E(\text{Gas})] \quad (3.2)$$

where  $E(\text{Gas}/\text{ZnOSL}-\text{TiO}_2)$  is the total energy of gas molecule adsorbed on the ZnOSL-TiO<sub>2</sub>, and  $E(\text{Gas})$  and  $E(\text{ZnOSL}-\text{TiO}_2)$  are the total energies of free adsorbate Gas and free ZnOSL-TiO<sub>2</sub> surface, respectively.

For the reaction step, reaction energy ( $\Delta E_{\text{reaction}}$ ) was computed by the energy difference between product(s) and reaction(s) such as an example for CO adsorbed on the CO/ZnOSL-TiO<sub>2</sub> to afford 2CO/ZnOSL-TiO<sub>2</sub>, using (3.3)

$$\Delta E_{\text{reaction}} = E(2\text{CO}/\text{ZnOSL}-\text{TiO}_2) - [E(\text{CO}/\text{ZnOSL}-\text{TiO}_2) + E(\text{CO})] \quad (3.3)$$

where  $E(\text{CO}/\text{CO}/\text{ZnOSL}-\text{TiO}_2)$  and  $E(\text{CO}/\text{ZnOSL}-\text{TiO}_2)$  are total energies of single and double CO molecules adsorbed on the ZnOSL-TiO<sub>2</sub>, respectively.  $E(\text{CO})$  is the total energy of free CO molecule.

The optimized structures of atomic and molecular oxygen adsorbed onto ZnOSL surface of the ZnOSL/TiO<sub>2</sub> are shown in **Figure S3.1** (in supplementary data).

### 3.4 RESULTS AND DISCUSSION

#### 3.4.1 Binding of ZnOSL cage on TiO<sub>2</sub> surface

The optimization for binding structure of the ZnOSL cage onto the anatase TiO<sub>2</sub> (001) surface (denoted by ZnOSL/TiO<sub>2</sub>) was carried out using periodic DFT computations. As there are only two faces of the ZnOSL (tetragonal and hexagonal) for binding to the TiO<sub>2</sub> (001) surface, only two possible binding configurations were used as initial geometries in their structure optimization process. Only one structure of the ZnOSL/TiO<sub>2</sub> was found as shown in **Figure 3.1(b)**. Interaction between the

ZnOSL and TiO<sub>2</sub> (101) surface was investigated but binding between them was not found. This can be described that TiO<sub>2</sub> (101) is a corrugated surface (saw tooth) and cannot fit with the ZnOSL surface. All possible initial configurations of ZnOSL bound to TiO<sub>2</sub> (001) surface were examined, but only one configuration of ZnOSL–TiO<sub>2</sub> as shown in **Figure 3.1** was found.

The binding energy of ZnOSL adsorbed onto the anatase TiO<sub>2</sub> (001) surface,  $\Delta E_{\text{binding}} = -70.78$  kcal/mol was obtained. The binding sites of the anatase TiO<sub>2</sub> (001) surface based on the ZnOSL adsorption are two Ti<sub>5c</sub> and two O<sub>2c</sub> atoms which bind to two oxygen atoms (O1 and O3) and two zinc atoms (Zn1 and Zn2) in hexagonal ring of the ZnOSL, respectively, see line-drawing picture in **Figure 3.1(b)**. The binding characteristic of the ZnOSL on the anatase TiO<sub>2</sub> (001) surface is that the ZnOSL using its hexagonal face toward the plane according two bonds of O<sub>2c</sub>–Ti<sub>5c</sub> of the TiO<sub>2</sub> (001) surface, see the sketch drawing for the top view of ZnOSL on the TiO<sub>2</sub> (001) surface in **Figure 3.1(b)**. The bond distances which correspond with binding sites are Zn1–O<sub>2c</sub> = 2.03 Å, Zn2–O<sub>2c</sub> = 2.07 Å, O1–Ti<sub>5c</sub> = 2.01 Å, and O3–Ti<sub>5c</sub> = 2.01 Å, see **Figure 3.1(b)**. Average of these four bond distances could represent the plane-to-plane distance of 2.03 Å.

#### 3.4.2 Adsorption structures of gases on the ZnOSL–TiO<sub>2</sub> and reaction profile

Adsorption of CO and O<sub>2</sub>, and CO<sub>2</sub> on the ZnOSL was studied [23], and its results show that binding strengths of these gases are not significantly different from their adsorptions on the ZnOSL of the ZnOSL–TiO<sub>2</sub>. Nevertheless, study of oxidation mechanism of 2CO + O<sub>2</sub> to 2CO<sub>2</sub> on the ZnOSL supported by TiO<sub>2</sub> (001) aims to utilize the ZnOSL/TiO<sub>2</sub> composite as a good-quality catalyst for the ZnOSL cage immobilized on the TiO<sub>2</sub> surface. The adsorption energies of O<sub>2</sub> ( $\Delta E_{\text{ads}} = -14.09$  kcal/mol) and CO ( $\Delta E_{\text{ads}} = -10.29$  kcal/mol) [23] are not much different, and either O<sub>2</sub> or CO can adsorb on the ZnOSL. Although O<sub>2</sub> and CO can competitively be adsorbed on the ZnOSL, reaction of O<sub>2</sub>/ZnOSL + 2CO → ZnOSL + 2CO<sub>2</sub> is not possible except for 2CO/ZnOSL + O<sub>2</sub> → ZnOSL + 2CO<sub>2</sub>. The reason is that the

concerted reaction for two CO molecules simultaneously reacting with pre-adsorbed oxygen molecule to form transition-state structure is hardly ever possible. Therefore, only the reaction of  $2\text{CO}/\text{ZnOSL} + \text{O}_2 \rightarrow 2\text{CO}_2$  is promising. All configurations of single and double molecular CO adsorptions on the ZnOSL of the ZnOSL-TiO<sub>2</sub> were examined, but only one configuration of  $\text{CO}/[\text{ZnOSL-TiO}_2]$  for single molecular adsorption and only one configuration of  $2(\text{CO})/[\text{ZnOSL-TiO}_2]$  for double molecular adsorption were found.

The adsorption structures of single and double molecules of CO and CO<sub>2</sub>, and reaction of O<sub>2</sub> on double CO adsorption on the ZnOSL of the ZnOSL-TiO<sub>2</sub> were obtained. The adsorption energies of single CO and single CO<sub>2</sub> on the ZnOSL-TiO<sub>2</sub> are -7.97 and -5.21 kcal/mol, respectively.

The reaction mechanism for CO interconversion to CO<sub>2</sub> on the ZnOSL of the ZnOSL-TiO<sub>2</sub> is composed of five reaction steps: The first step is the adsorption of CO on the ZnOSL of the ZnOSL-TiO<sub>2</sub>,  $\text{CO} + [\text{ZnOSL}/\text{TiO}_2] \rightarrow \text{CO}/[\text{ZnOSL}/\text{TiO}_2]$ . The second step is the adsorption of the second CO molecule on the ZnOSL of the ZnOSL-TiO<sub>2</sub>,  $\text{CO} + \text{CO}/[\text{ZnOSL}/\text{TiO}_2] \rightarrow 2\text{CO}/[\text{ZnOSL}/\text{TiO}_2]$ . The third step is the collision of O<sub>2</sub> to two CO molecules pre-adsorbed on the ZnOSL of the ZnOSL-TiO<sub>2</sub> to afford the  $2\text{CO}_2/[\text{ZnOSL}/\text{TiO}_2]$ ,  $\text{O}_2 + 2\text{CO}/[\text{ZnOSL}/\text{TiO}_2] \rightarrow 2\text{CO}_2/[\text{ZnOSL}/\text{TiO}_2]$ . The kinetic of this step could follow an Eley-Rideal mechanism, because the O<sub>2</sub> molecule collides with two CO molecules pre-adsorbed on the ZnOSL of the ZnOSL-TiO<sub>2</sub>. The last step is the desorption of CO<sub>2</sub> from  $2\text{CO}_2/[\text{ZnOSL}/\text{TiO}_2]$ ,  $2\text{CO}_2/[\text{ZnOSL}/\text{TiO}_2] \rightarrow [\text{ZnOSL}/\text{TiO}_2] + 2\text{CO}_2$ . Reaction energies for all reaction steps are listed in **Table 3.1**. The energy of -179.76 kcal/mol for the overall reaction,  $2\text{CO} + \text{O}_2 + [\text{ZnOSL}/\text{TiO}_2] \rightarrow [\text{ZnOSL}/\text{TiO}_2] + 2\text{CO}_2$ , was obtained. The potential energy profile for the CO interconversion to CO<sub>2</sub> on the ZnOSL of the ZnOSL-TiO<sub>2</sub> is shown in **Figure 3.2**.

**Table 3.1** Binding of the ZnOSL cage onto the TiO<sub>2</sub> (001) surface to afford [ZnOSL/TiO<sub>2</sub>], its reaction for CO oxidation to CO<sub>2</sub>, and all related adsorption reactions.

Reactions	$\Delta E_{\text{reaction}}^{\text{a}}$
<i>Binding</i>	
ZnOSL + TiO <sub>2</sub> → [ZnOSL/TiO <sub>2</sub> ]	-70.78
<i>Stepwise CO interconversion</i>	
[ZnOSL/TiO <sub>2</sub> ] + CO → CO/[ZnOSL/TiO <sub>2</sub> ]	-7.97
CO/[ZnOSL/TiO <sub>2</sub> ] + CO → 2CO/[ZnOSL/TiO <sub>2</sub> ]	-7.08
2CO/[ZnOSL/TiO <sub>2</sub> ] + O <sub>2</sub> → 2CO <sub>2</sub> /[ZnOSL/TiO <sub>2</sub> ]	-172.22
2CO <sub>2</sub> /[ZnOSL/TiO <sub>2</sub> ] → 2CO <sub>2</sub> + [ZnOSL/TiO <sub>2</sub> ]	-7.52
<i>Overall</i>	
2CO + O <sub>2</sub> + [ZnOSL/TiO <sub>2</sub> ] → [ZnOSL/TiO <sub>2</sub> ] + 2CO <sub>2</sub>	-179.76
<i>CO<sub>2</sub> adsorption</i>	
[ZnOSL/TiO <sub>2</sub> ] + 2CO <sub>2</sub> → 2CO <sub>2</sub> /[ZnOSL/TiO <sub>2</sub> ]	-5.21
2CO <sub>2</sub> /[ZnOSL/TiO <sub>2</sub> ] + CO <sub>2</sub> → 2CO <sub>2</sub> + [ZnOSL/TiO <sub>2</sub> ]	-2.31

<sup>a</sup> In kcal/mol .

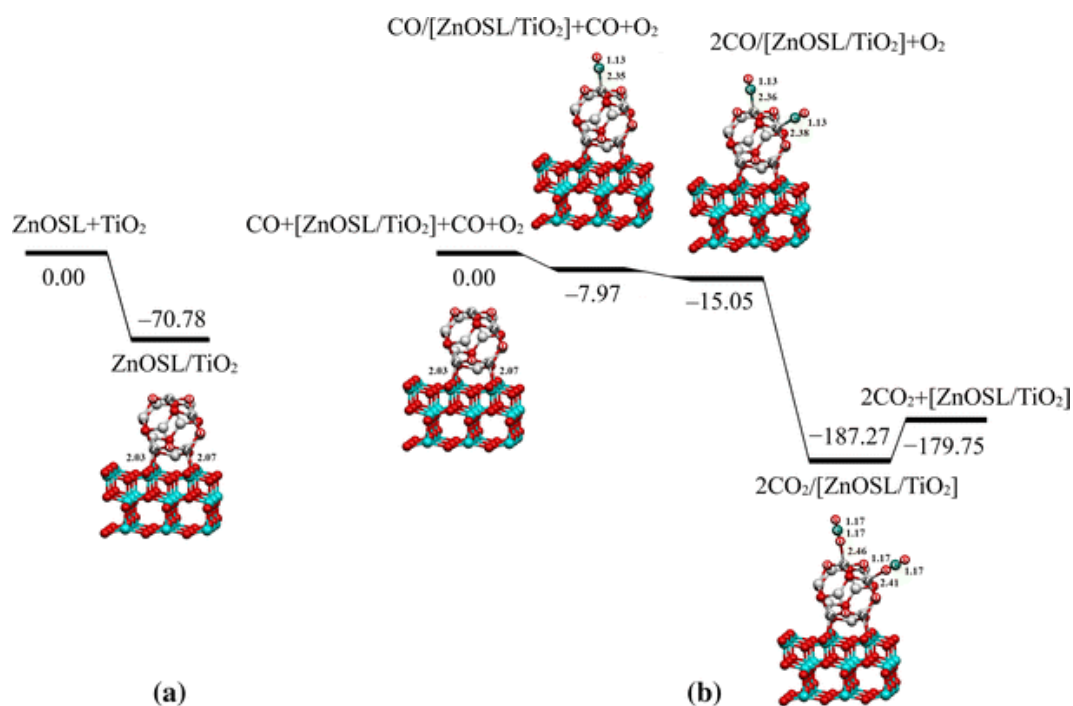


**Figure 3.2** Potential energy profiles for (a) association of ZnOSL cage onto anatase TiO<sub>2</sub> (001) surface and (b) conversion reaction of CO + O<sub>2</sub> to CO<sub>2</sub> on the ZnOSL/TiO<sub>2</sub>. Bond lengths are in Å. Relative energies are in kcal/mol.

To compare with CO oxidation on the Au- and Pt-supported TiO<sub>2</sub>(110), either on the interfacial sites of Au<sub>11</sub>/TiO<sub>2</sub>(110)<sub>OH</sub> or Au<sub>8</sub>Pt<sub>3</sub>/TiO<sub>2</sub>(110)<sub>OH</sub> or Pt<sub>11</sub>/TiO<sub>2</sub>(110)<sub>OH</sub> or the Pt site of Au<sub>8</sub>Pt<sub>3</sub>/TiO<sub>2</sub>(110)<sub>OH</sub>, their reaction steps are composed of (1) the step of co-adsorption of CO and O<sub>2</sub> on their adsorption sites and (2) the conversion step via their transition state to afford CO<sub>2</sub> molecule [102]. Even though, the CO oxidation by lattice oxygen either on the surface outside or inside the wall of V<sub>2</sub>O<sub>5</sub> (5, 5) nanotubes, the two-step reaction as similar as on the Au- and Pt-supported TiO<sub>2</sub>(110) was found [103].

The adsorption energies of CO<sub>2</sub> on the ZnOSL of the ZnOSL-TiO<sub>2</sub> to form CO<sub>2</sub>/[ZnOSL/TiO<sub>2</sub>] or 2CO<sub>2</sub>/[ZnOSL/TiO<sub>2</sub>] were obtained, and potential energy profile due to these adsorption energies is shown in **Figure 3.3**. It shows the first, CO<sub>2</sub> + [ZnOSL/TiO<sub>2</sub>] → CO<sub>2</sub>/[ZnOSL/TiO<sub>2</sub>], and the second adsorptions of CO<sub>2</sub> on

ZnOSL of the ZnOSL–TiO<sub>2</sub>, CO<sub>2</sub> + CO<sub>2</sub>/[ZnOSL/TiO<sub>2</sub>] → 2CO<sub>2</sub>/[ZnOSL/TiO<sub>2</sub>], of which stepwise adsorption energies are –5.21 and –2.31 kcal/mol, respectively. It may be concluded that CO<sub>2</sub> adsorbed on the ZnOSL/TiO<sub>2</sub> is somewhat weak interaction.

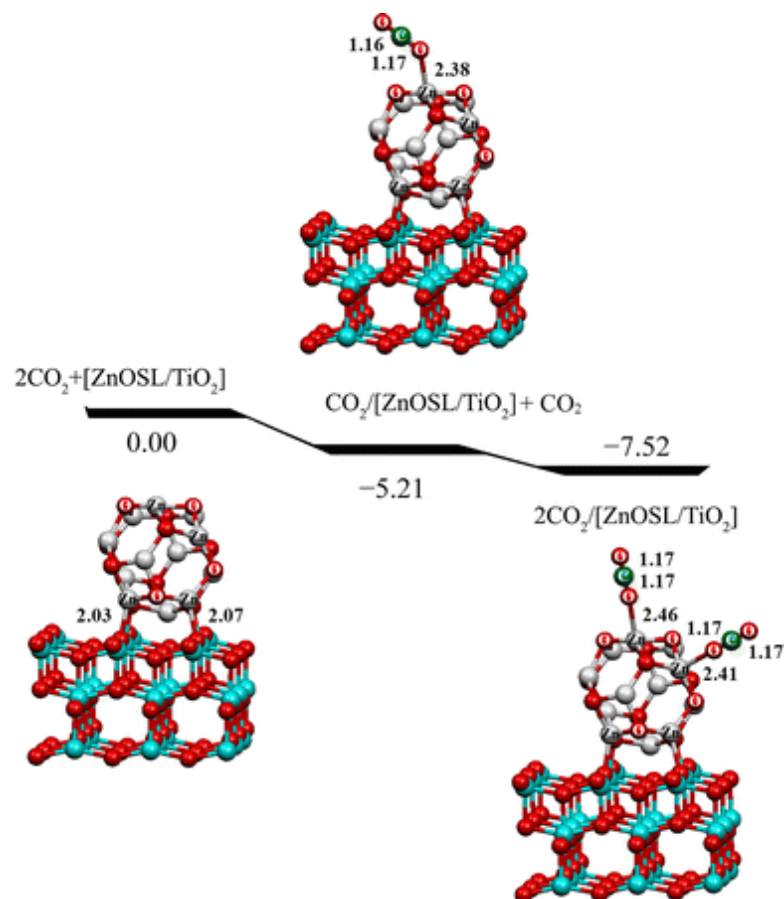


**Figure 3.3** Potential energy profile for stepwise adsorption of CO<sub>2</sub> onto ZnOSL surface of ZnOSL/TiO<sub>2</sub>. Bond lengths are in Å. Relative energies are in kcal/mol.

### 3.5 CONCLUSION

The ZnOSL adsorbed onto  $\text{TiO}_2$  (001) surface and its ability for CO to  $\text{CO}_2$  interconversion were studied using the B3LYP method. All possible initial configurations of ZnOSL bound to  $\text{TiO}_2$  (001) surface were examined, but only one configuration of ZnOSL– $\text{TiO}_2$  was found. The strong binding for the ZnOSL onto  $\text{TiO}_2$  (001) surface to form ZnOSL/ $\text{TiO}_2$  was found, the binding energy of which is  $-70.78$  kcal/mol. The binding between the ZnOSL and the  $\text{TiO}_2$  (001) surface was found that the ZnOSL employs its hexagonal face toward the plane which is constructed from two  $\text{O}_{2c}$ – $\text{Ti}_{5c}$  bonds of the  $\text{TiO}_2$  (001) surface and its average plane–to–plane distance of  $2.03 \text{ \AA}$  was found. All configurations of single and double molecular CO adsorptions on the ZnOSL of the ZnOSL– $\text{TiO}_2$  were examined, but only one configuration of  $\text{CO}/[\text{ZnOSL–TiO}_2]$  for single molecular adsorption and only one configuration of  $2(\text{CO})/[\text{ZnOSL–TiO}_2]$  for double molecular adsorption were found. The reaction mechanism for CO to  $\text{CO}_2$  interconversion on the ZnOSL of the ZnOSL– $\text{TiO}_2$  is composed of five reaction steps. The stepwise adsorption energies of the first and second  $\text{CO}_2$  adsorptions are  $-5.21$  and  $-2.31$  kcal/mol, respectively. The energy of  $-179.76$  kcal/mol for the overall reaction of  $2\text{CO} + \text{O}_2 + [\text{ZnOSL}/\text{TiO}_2] \rightarrow [\text{ZnOSL}/\text{TiO}_2] + 2\text{CO}_2$  was obtained. The adsorption energies of  $\text{CO}_2$  on the ZnOSL of the ZnOSL– $\text{TiO}_2$  to form  $\text{CO}_2/[\text{ZnOSL}/\text{TiO}_2]$  or  $2\text{CO}_2/[\text{ZnOSL}/\text{TiO}_2]$  were obtained.

## 3.6 SUPPLEMENTARY DATA

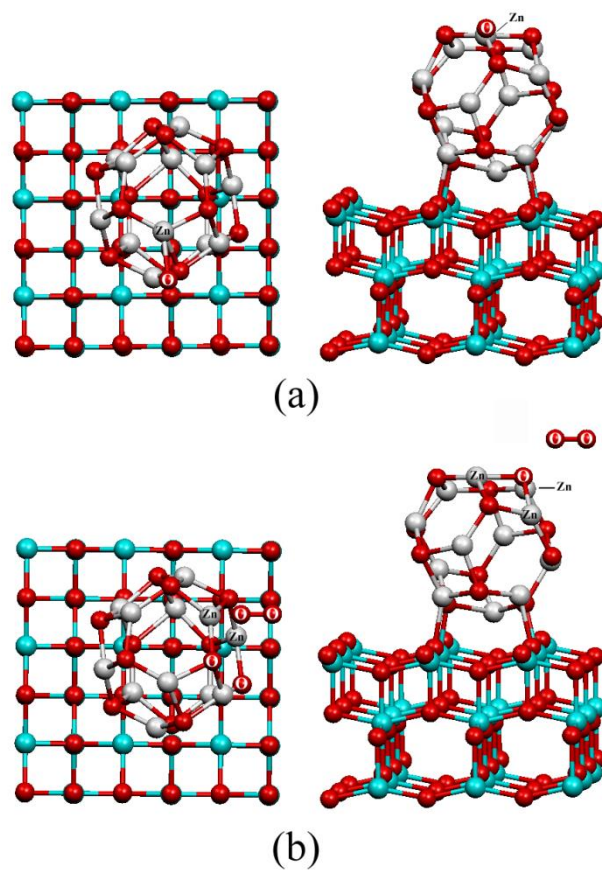


**Figure S3.1** The optimized structures of (a) O atom and (b) O<sub>2</sub> molecule adsorbed onto ZnOSL surface of the ZnOSL/TiO<sub>2</sub>. Left and right images are top and front views, respectively.

# CHAPTER IV

## DFT INVESTIGATION ON MOLECULAR STRUCTURES OF METAL AND NONMETAL–DOPED ZnO SODALITE–LIKE CAGE AND THEIR ELECTRONIC PROPERTIES

Waranyu Pipornpong, Benjawan Kaewrukksa, Vithaya Ruangpornvisuti

This article has been published in Structural Chemistry,

Volume 27, Issue 3, page 773–784 year: 2015.

### 4.1 ABSTRACT

The optimized structures of the ZnOSLs doped by single metal atoms (Sc, Ti, V, Cr, Mn, Fe, Co, Ni, Cu, Pd, Ag, Pt and Au) and single nonmetal atoms (B, C, N, Al, Si, P, Ga and Ge) were obtained using DFT/B3LYP method. The energetics and thermodynamic properties for doping processes of single metal atom to  $Zn_V$  of the Zn vacancy defect ZnOSL surface, ( $ZnOSL + Zn_V$ ) and nonmetal atom to  $O_V$  of the O vacancy defect ZnOSL surface, ( $ZnOSL + O_V$ ) were obtained. The binding abilities of transition metal dopants to  $Zn_V$  of [ $ZnOSL + Zn_V$ ] and nonmetal dopants to  $O_V$  of [ $ZnOSL + O_V$ ] surfaces are in orders:  $Cr > Ti > Sc > V > Fe > Mn > Ni > Co > Pt > Zn > Cu > Pd > Au > Ag$  and  $O > N > C > P > Si > Ge > Ga > B > Al$ , respectively. Energy gaps and NBO partial charges for low–spin and high–spin states of metal and nonmetal–doped ZnOSLs and their analyses are reported.

### 4.2 INTRODUCTION

The ground states of the ZnO diatomic molecule were investigated using photoelectron spectroscopic method [60], and the  $(ZnO)_n$  clusters ( $n = 20$ ) experimentally were explored using mass spectroscopic method [61]. The ground

states [62] and their excitation states [9] of small-sized  $(\text{ZnO})_n$  clusters with  $n = 1-15$  were studied using DFT and time-dependent DFT (TDDFT) methods, respectively. The low-spin structures and electronic properties of various sizes of  $(\text{ZnO})_n$  clusters ( $n = 9-64$ ) [29], ( $n = 2-18, 21$ ) [14], ( $n = 1-32$ ) [15], ( $n = 2-18$ ) [16], ( $n = 24, 28, 36$  and  $48$ ) [104], ( $n = 1-32$ ) [33], and  $\text{Zn}_3\text{O}_m$  ( $m = 3-5$ ) [42] were theoretically characterized using various computational methods, and the optical properties of  $(\text{ZnO})_n$  clusters ( $n = 2-12$ ) were studied using DFT method [41]. The zinc oxide clusters were studied by mass spectroscopic method, and the clusters of  $(\text{ZnO})_{34}$ ,  $(\text{ZnO})_{60}$ , and  $(\text{ZnO})_{78}$  were found as the magic number clusters [40]. One of the  $(\text{ZnO})_{60}$  cluster as the sodalite-based structure was found [105]. The ZnOSL as  $(\text{ZnO})_{12}$  cluster and its adsorption configurations with small gases were studied by DFT method, and it was found that energy gaps of gas-adsorbed ZnOSLs depend on the adsorbate gases [23]. Moreover, energy gaps of ZnO clusters were found to decrease when their size was increased [106].

Nevertheless, electronic, magnetic, and catalytic properties of metal-doped ZnO were extensively widely explored in order to be used for chemical and physical applications. Energy gaps of Ag-doped ZnO [17] and Fe-doped ZnO [53] were found to be decreased when compared to their un-doped structures. Ag-doped ZnO nanoparticles (Ag-doped ZnONPs) were studied, and effect of Ag dilute doping on the structural, optical, and photocatalytic properties of ZnO nanoparticles was investigated [54]. Cu-doped ZnO nanosheet (ZnONS) was studied, and it was found that Cu atom prefers to substitute for Zn site and is able to induce a local magnetic moment of  $1.00 \mu\text{B}$  per unit in ZnONS [63].

Co-doped ZnO nanocrystals were found to show ferromagnetism and ferromagnetic properties at room temperature, and their ordering strengths were varied with the Co concentration [64]. The ferromagnetism was also found on V-doped ZnO nanowires [80]. The Co-doped and Co-/Mn-co-doped ZnO nanocrystals were studied, and Co-/Mn-co-doped ZnO was found to be magneto-electronic material [107]. Electronic structure and optical properties of Ga-doped ZnO with various concentrations of Ga were studied, and it was found that the donor

concentration and optical band gap of Ga-doped ZnO increase with an increase in Ga content [69].

The Ni-doped ZnO was studied for its structural and electronic properties [71] magnetic properties and photoemission [72], and gas sensors [65]. The Mn-, Cu- and Co-doped  $(\text{ZnO})_{12}$  clusters were studied, and it was found that their band gaps decrease due to p-d hybridization orbitals of the dopant atom with the orbitals of the oxygen atom [66]. Geometries, electronic structures, and magnetic properties of Sc-, Ti-, V-, Cr-, Mn-, Fe-, Co-, Ni-, and Cu-doped ZnO monolayers were studied, and the results show that the doping of Cr, Mn, Fe, Co, Ni, and Cu atoms can induce magnetization, whereas there is no magnetism in the Sc-, Ti-, and V-doped ZnO monolayers [67]. Moreover, Co- and Cu-doped zinc-blended ZnO nanocrystals were found to be magnetic semiconductor [108] and ferromagnetic, respectively [73].

The magnetic properties of N-doped  $(\text{ZnO})_n$  clusters ( $n = 1-16$ ) were studied, and the total energy calculations suggest that N is more stable at the O site than at the Zn site in  $(\text{ZnO})_n$  clusters and induces a magnetic moment of 1  $\mu\text{B}/\text{N}$  atom [109]. The electronic structure and magnetic properties of N-doped ZnO with and without Zn vacancy were investigated, and the results suggest that N-doped ZnO is a weak ferromagnetism [74]. The optoelectronic properties of Ga- and Al-doped ZnO thin films were found to have the good conductivity and transparence [75]. The C-doped ZnO thin films were studied, and they were found to be ferromagnetic [76]. C-doped  $(\text{ZnO})_n$  ( $n = 1-12$ ) clusters were studied, and it was found that the substitutional C impurity is more favorable than interstitial C impurity in C-doped  $(\text{ZnO})_n$  clusters [110].

Nevertheless, the electronic properties of the ZnOSL cage can be improved by doping single atom of elements for metal and nonmetal atoms. In this work, structures of ZnOSL cage and its metal and nonmetal doping structures have been studied, and their electronic and thermodynamic properties have been investigated. Two types of dopants, as atoms of transition metals and nonmetal, have been selected. Their energy gaps and charge transfer for dopants in metal- and nonmetal-doped ZnOSLs have been analyzed and reported. Predictions for their properties have been presented.

### 4.3 COMPUTATIONAL DETAILS

Full optimizations of structures of ZnOSL cage ( $Zn_{12}O_{12}$  cluster) and its metal (Sc, Ti, V, Cr, Mn, Fe, Co, Ni, Cu, Pd, Ag, Pt and Au) and nonmetal (B, C, N, Al, Si, P, Ga and Ge) doping were carried out using DFT method. Doping principle is on a replacement of single metal atom to single Zn atom or single nonmetal atom to single O atom of ZnOSL cage. As all Zn and all O atoms of the ZnOSL cage are equivalent, and any position of Zn (or O) atom in ZnOSL doped with single metal (or nonmetal) atom must give a single structure. Therefore, metal-doped structure obtained by replacing single Zn atom at any position with single metal (dopant) atom must be only one structure and replacing single O atom at any position with nonmetal (dopant) must be also only one structure.

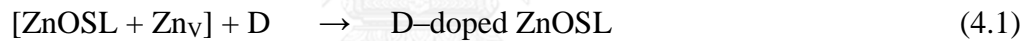
For metal doping system, total electronic states for low-spin Ti-, Cr-, Fe-, Ni-, Pd-, and Pt-doped ZnOSL as singlet state (spin multiplicity = 1) and Sc-, V-, Mn-, Co-, Cu-, Ag-, and Au-doped ZnOSL as doublet state (spin multiplicity = 2) were applied. Triplet state for high-spin Ti-, Cr-, Fe-, Ni-, Pd-, and Pt-doped ZnOSL and quartet state for high-spin Sc-, V-, Mn-, Co-, Cu-, Ag-, and Au-doped ZnOSL were employed. For nonmetal doping system, low-spin C-, Si-, and Ge-doped ZnOSL as singlet state and low-spin B-, N-, Al-, P-, and Ga-doped ZnOSL as doublet state were applied of which high-spin surfaces were treated as triplet and quartet states, respectively.

The calculations have been performed with hybrid density functional B3LYP, Becke's three-parameter exchange functional with the Lee-Yang-Parr correlation functional, B3LYP [99, 100, 111] using the Los Alamos LanL2DZ split-valence basis set [40-42]. All structures were fully optimized without any constraints and characterized by computed vibration frequency. Enthalpies ( $H$ ) and Gibbs free energies ( $G$ ) of all compounds were derived from their vibration frequency computations at 298.15 K and standard pressure [112].

The energy gaps referring the energy difference between highest occupied molecular orbital (HOMO) and the lowest unoccupied molecular orbital (LUMO)

orbitals ( $E_{\text{HOMO-LUMO}} = E_g$ ) or the singly occupied molecular orbital (SOMO) and LUMO orbitals ( $E_{\text{SOMO-LUMO}} = E_g$ ) were also investigated at the same level of theory. In addition, natural bond orbital (NBO) analysis implemented in the GAUSSIAN 09 program [113] was applied for calculations of all compounds. The molecular graphics of all compounds were generated with the MOLEKEL 4.3 program [114]. The electronic density of states (DOSs) for all studied structures was plotted by the GaussSum 2.1.4 program [115].

Metal- or nonmetal-doped ZnOSL is defined as replacing Zn or O atom of ZnOSL by metal dopant (D) or non-metal dopant (D'), respectively. Therefore, metal or nonmetal doping process can be defined as an introduction of single metal into a vacancy of Zn vacancy defect ZnOSL ( $[\text{ZnOSL} + \text{Zn}_v]$ ) or single non-metal atom into a vacancy of O vacancy defect ZnOSL ( $[\text{ZnOSL} + \text{O}_v]$ ), respectively. Doping process for metal and metal-doped ZnOSLs, denoted as D-doped ZnOSL and D'-doped ZnOSL, respectively, can be written as (4.1) and (4.2)



The binding energies ( $\Delta E_{\text{binding}}$ ), enthalpies ( $\Delta H_{\text{binding}}^{\circ}$ ), and Gibbs free energies ( $\Delta G_{\text{binding}}^{\circ}$ ) were, respectively, computed from total energies, enthalpies, and free energies of metal- and nonmetal-doped ZnOSLs, and their corresponding components are shown in (4.3)–(4.8)

$$\Delta E_{\text{binding}} = E(\text{D-doped ZnOSL}) - \{E([\text{ZnOSL} + \text{Zn}_v]) + E(\text{D})\} \quad (4.3)$$

$$\Delta H_{\text{binding}}^{\circ} = H(\text{D-doped ZnOSL}) - \{H([\text{ZnOSL} + \text{Zn}_v]) + H(\text{D})\} \quad (4.4)$$

$$\Delta G_{\text{binding}}^{\circ} = G(\text{D-doped ZnOSL}) - \{G([\text{ZnOSL} + \text{Zn}_v]) + G(\text{D})\} \quad (4.5)$$

$$\Delta E_{\text{binding}} = E(\text{D'-doped ZnOSL}) - \{E([\text{ZnOSL} + \text{O}_v]) + E(\text{D}')\} \quad (4.6)$$

$$\Delta H_{\text{binding}}^{\circ} = H(\text{D'-doped ZnOSL}) - \{H([\text{ZnOSL} + \text{O}_v]) + H(\text{D}')\} \quad (4.7)$$

$$\Delta G^{\circ}_{\text{binding}} = G(\text{D}'\text{-doped ZnOSL}) - \{G([\text{ZnOSL} + \text{O}_v]) + G(\text{D}')\} \quad (4.8)$$

where  $E$ ,  $H$  and  $G$  are total energy, enthalpy and Gibbs free energy of the individual components of the binding processes.

## 4.4 RESULTS AND DISCUSSION

### 4.4.1 Optimized structures of metal-doped ZnOSLs and their energy gaps

The B3LYP/LanL2DZ-optimized structures of Sc-, Ti-, V-, Cr-, Mn-, Fe-, Co-, Ni-, Cu-, Pd-, Ag-, Pt-, and Au-doped ZnOSLs of which formulae are therefore  $\text{ScZn}_{11}\text{O}_{12}$ ,  $\text{TiZn}_{11}\text{O}_{12}$ ,  $\text{VZn}_{11}\text{O}_{12}$ ,  $\text{CrZn}_{11}\text{O}_{12}$ ,  $\text{MnZn}_{11}\text{O}_{12}$ ,  $\text{FeZn}_{11}\text{O}_{12}$ ,  $\text{CoZn}_{11}\text{O}_{12}$ ,  $\text{NiZn}_{11}\text{O}_{12}$ ,  $\text{CuZn}_{11}\text{O}_{12}$ ,  $\text{PdZn}_{11}\text{O}_{12}$ ,  $\text{AgZn}_{11}\text{O}_{12}$ ,  $\text{PtZn}_{11}\text{O}_{12}$ , and  $\text{AuZn}_{11}\text{O}_{12}$ , respectively, are shown in **Figure 4.1**. The Zn-doped ZnOSL is identical to undoped ZnOSL as shown in **Figure 4.1(j)**. The V-doped ZnOSL is the most distorted structure as compared with undoped ZnOSL, see **Figure 4.1(c)**. The plots of frontier orbitals of the metal-doped ZnOSLs are shown in **Figure 4.2** and their DOSs are shown in **Figure 4.1**. SOMOs and HOMOs of all metal-doped ZnOSL are located around dopant atom except for Sc-doped ZnOSL, because its SOMO is distributed almost over the whole molecule see **Figure 4.2(a)**. HOMO of undoped ZnOSL, and **Figure 4.2(j)** being consistently distributed over the whole molecule was found. LUMOs in all doped and undoped ZnOSLs are distributed almost over the whole molecules, except V-, Ni-, Pd-, and Pt-doped ZnOSLs of which LUMOs are located around their dopant atom. Plots of the frontier orbitals and DOSs of the high-spin state of metal-doped ZnOSLs are, respectively, shown in **Figure S4.1** and **Figure S4.2** in supplementary data. It shows that LUMOs of the high-spin metal-doped ZnOSLs and undoped ZnOSL are distributed over the entire molecule.

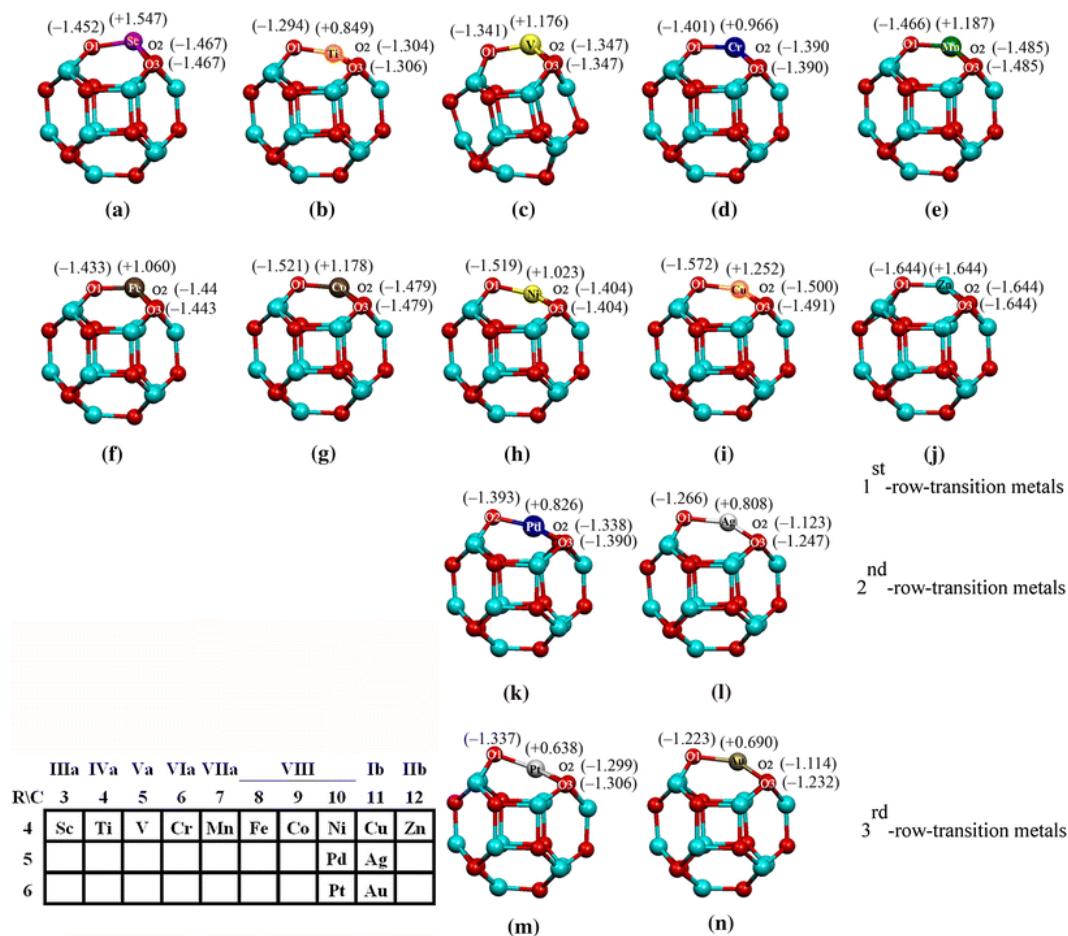


**Figure 4.1** The B3LYP/LanL2DZ-optimized structures of (a) Sc-, (b) Ti-, (c) V-, (d) Cr-, (e) Mn-, (f) Fe-, (g) Co-, (h) Ni-, (i) Cu-doped ZnOSLs, (j) undoped ZnOSL, (k) Pd-, (l) Ag-, (m) Pt- and (n) Au-doped ZnOSLs. The NBO charges for selected atoms are presented in e. a-j, k and l, and m and n are the fourth, fifth and sixth rows transition metal doping structures, respectively. All the metal-doped ZnOSLs are shown based on the periodic table as noted on the bottom left side.

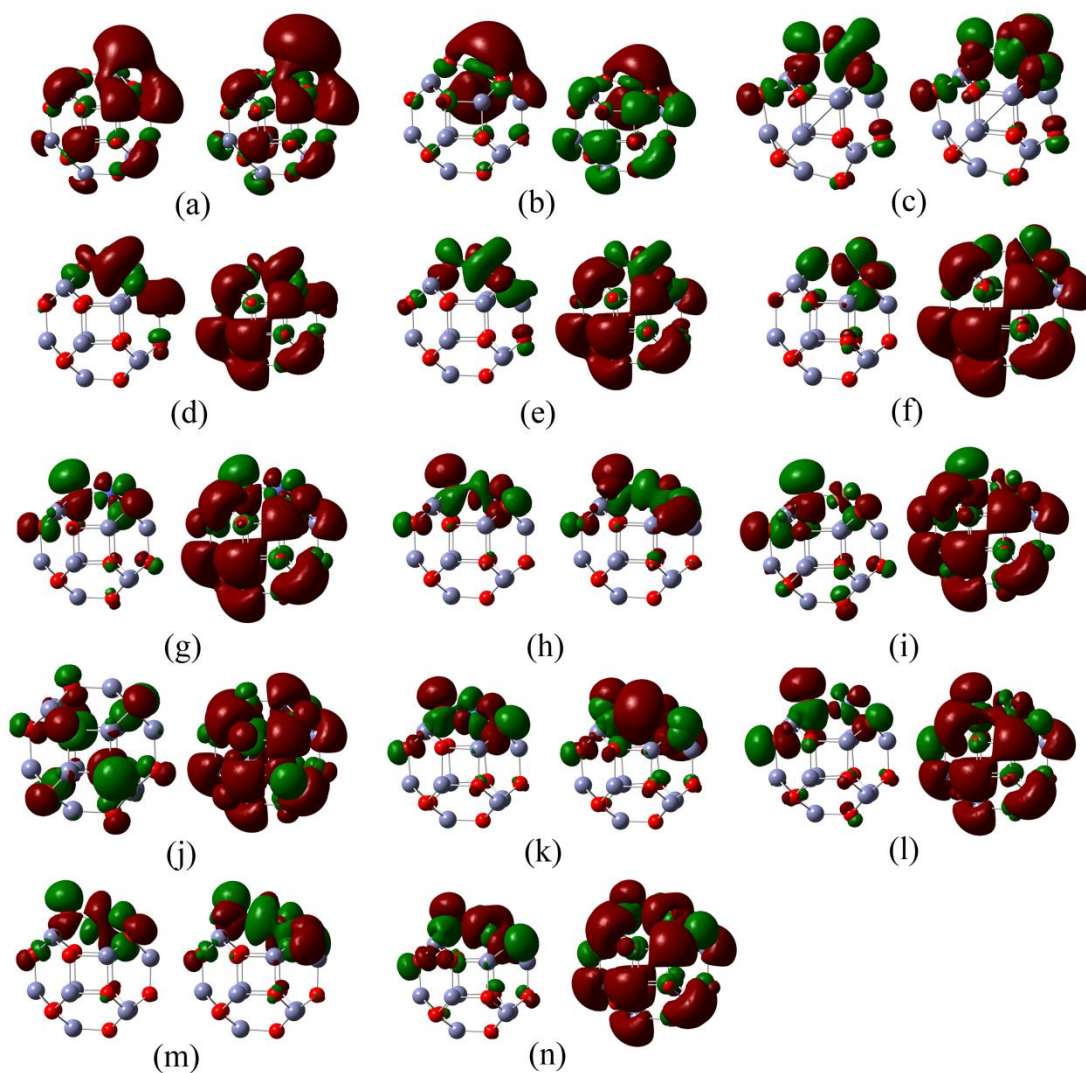


**Figure 4.2** Plots of frontier orbitals of the low-spin (a) Sc-, (b) Ti-, (c) V-, (d) Cr-, (e) Mn-, (f) Fe-, (g) Co-, (h) Ni-, (i) Cu-doped ZnOSLs, (j) undoped ZnOSL, (k) Pd-, (l) Ag-, (m) Pt- and (n) Au-doped ZnOSLs. All the orbitals of metal-doped ZnOSLs are shown at the same positions of their corresponding structures shown in **Figure 4.1**

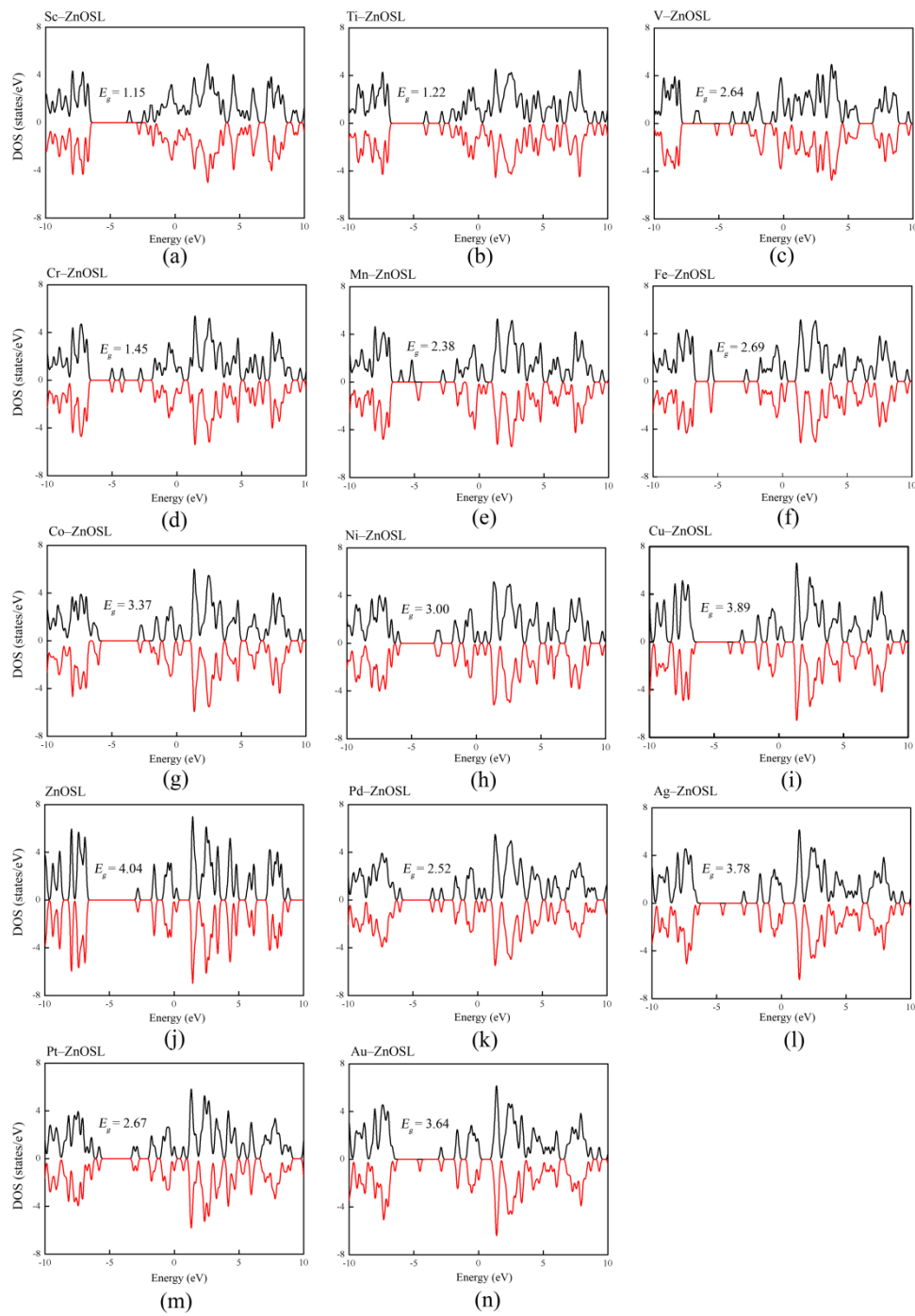


**Figure 4.3** DOSs of the low-spin (a) Sc-, (b) Ti-, (c) V-, (d) Cr-, (e) Mn-, (f) Fe-, (g) Co-, (h) Ni-, (i) Cu-doped ZnOSLs, (j) undoped ZnOSL, (k) Pd-, (l) Ag-, (m) Pt- and (n) Au-doped ZnOSLs. All the DOSs of metal-doped ZnOSLs are shown at the same positions of their corresponding structures shown in **Figure 4.1**

The selected geometrical parameters are shown in **Table S4.1**, in supplementary data. It shows that O1–D, O2–D, and O3–D bond distances of all the ZnOSLs doped by first–row transition metal are shorter than undoped ZnOSL, but bond distances of all the second– and third–row transition–metal–doped ZnOSLs are longer. These results correspond with atomic radii of dopants.

The energy gaps, energetics, binding strength, and dipole moment of low– and high–spin states of undoped and metal (D)–doped ZnOSLs are shown in **Table 4.1** and **Table 4.2**, respectively. Plots of energy gaps of the low–spin and high–spin metal–doped ZnOSLs and Gibbs free energy changes of binding of single atom of metal dopant toward  $Zn_V$  of the low–spin and high–spin  $[ZnOSL + (Zn_V)]$  surfaces are shown in **Figure 4.4**. It shows that energy gaps of all low–spin transition–metal–doped ZnOSLs are smaller than their corresponding high–spin ones, except for V–, Cu– and Zn–doped ZnOSLs (for the first–row transition metal dopants), Ag– (the second–row transition metal dopant) and Au–doped (the third–row transition metal dopant) clusters of which values are in reversed orientation. The metal–doped ZnOSLs which have remarkably low energy gaps are in the following order: low–spin Sc– < Ti– < Cr–doped ZnOSLs < high–spin Cu– < Zn–  $\approx$  Ag–  $\approx$  Au–doped ZnOSLs; their values are enclosed by blue dashed line as shown in **Figure 4.4(a)**. Free energy changes of doping reactions for high–spin metal–doped ZnOSLs are more favorable than their low–spin states, except Cr–doped ZnOSL of which values for both states are hardly ever changed. Based on low–lying energy gap, the energy gaps of metal–doped ZnOSLs are in increasing order: Sc (D: 1.15 eV) < Ti (S: 1.22 eV) < Cr (S: 1.45 eV) < V (Q: 1.55 eV) < Cu (Q: 1.63 eV) < Au (Q: 1.75 eV) < Ag (Q: 1.77 eV) < Zn (T: 1.78 eV) < Mn (D: 2.38 eV) < Pd (D: 2.52 eV) < Pt (D: 2.67 eV) < Fe (S: 2.69 eV) < Ni (S: 3.00 eV) < Co (D: 3.37 eV); S (singlet), D (doublet) and Q (quartet) symbols in parentheses are spin states of molecules. The energy gaps of high–spin V–, Cu–, Ag–, Au–doped and undoped ZnOSLs were found to be smaller than their low–spin structures by 1.09, 2.26, 2.01, 1.89, and 2.26 eV, respectively. It may be concluded that Sc–, Ti–, and Cr–doped ZnOSLs can be used as conducting materials because of their low energy gaps and V–, Cu–, Ag–, and Au–doped and undoped ZnOSLs may be employed as photocatalysts.

**Table 4.1** Energy gaps, energetics and dipole moment of undoped, metal- and nonmetal-doped ZnOSLs, computed at the B3LYP/LanL2DZ level of theory.

Metal-doped ZnOSL	$E_g^a$	$\Delta E_g^b$	DM <sup>c</sup>	Nonmetal-doped ZnOSL	$E_g^a$	$\Delta E_g^b$	DM <sup>c</sup>
Sc-doped ZnOSL	1.15	-2.89	1.931	B-doped ZnOSL	2.42	-1.62	1.128
Ti-doped ZnOSL	1.22	-2.82	2.399	C-doped ZnOSL	2.02	-2.02	0.744
V-doped ZnOSL	2.64	-1.40	1.060	N-doped ZnOSL	4.06	0.02	0.456
Cr-doped ZnOSL	1.45	-2.59	0.839	ZnOSL	4.04	0.00	0.000
Mn-doped ZnOSL	2.38	-1.66	2.612	Al-doped ZnOSL	1.64	-2.40	0.702
Fe-doped ZnOSL	2.69	-1.34	1.216	Si-doped ZnOSL	1.68	-2.36	1.206
Co-doped ZnOSL	3.37	-0.67	1.607	P-doped ZnOSL	3.55	-0.49	0.599
Ni-doped ZnOSL	3.00	-1.04	2.405	Ga-doped ZnOSL	1.63	-2.41	0.678
Cu-doped ZnOSL	3.89	-0.15	1.612	Ge-doped ZnOSL	1.64	-2.39	0.838
ZnOSL	4.04	0.00	0.000				
Pd-doped ZnOSL	2.52	-1.51	2.579				
Ag-doped ZnOSL	3.78	-0.26	1.750				
Pt-doped ZnOSL	2.67	-1.37	3.041				
Au-doped ZnOSL	3.64	-0.40	2.411				

<sup>a</sup> In eV.

<sup>b</sup> Defined as  $E_g(\text{D-ZnOSL}) - E_g(\text{ZnOSL})$ .

<sup>c</sup> Dipole moment, in Debye.

**Table 4.2** Energy gaps, energetics and dipole moment of high-spin undoped, metal- and nonmetal-doped ZnOSLs, computed at the B3LYP/LanL2DZ level of theory.

Metal-doped ZnOSL	$E_g^a$	$\Delta E_g^b$	DM <sup>c</sup>	Nonmetal-doped ZnOSL	$E_g^a$	$\Delta E_g^b$	DM <sup>c</sup>
Sc-doped ZnOSL	0.98	-0.80	0.364	B-doped ZnOSL	2.59	0.81	1.431
Ti-doped ZnOSL	1.30	-0.48	2.248	C-doped ZnOSL	3.48	1.70	1.043
V-doped ZnOSL	1.55	-0.23	1.220	N-doped ZnOSL	1.71	-0.07	2.713
Cr-doped ZnOSL	2.20	0.42	1.625	ZnOSL	1.78	0.00	0.001
Mn-doped ZnOSL	3.07	1.29	2.220	Al-doped ZnOSL	2.49	0.71	0.646
Fe-doped ZnOSL	3.42	1.64	1.585	Si-doped ZnOSL	3.07	1.29	1.364
Co-doped ZnOSL	3.75	1.97	0.800	P-doped ZnOSL	1.68	-0.10	1.991
Ni-doped ZnOSL	3.98	2.20	0.705	Ga-doped ZnOSL	2.43	0.65	0.610
Cu-doped ZnOSL	1.63	-0.15	2.166	Ge-doped ZnOSL	2.96	1.18	1.341
ZnOSL	1.78	0.00	1.364				
Pd-doped ZnOSL	3.45	1.67	1.490				
Ag-doped ZnOSL	1.77	-0.01	1.704				
Pt-doped ZnOSL	2.74	0.96	2.853				
Au-doped ZnOSL	1.75	-0.02	1.746				

<sup>a</sup> In eV.

<sup>b</sup> Defined as  $E_g(\text{D-ZnOSL}) - E_g(\text{ZnOSL})$ .

<sup>c</sup> Dipole moment, in Debye.

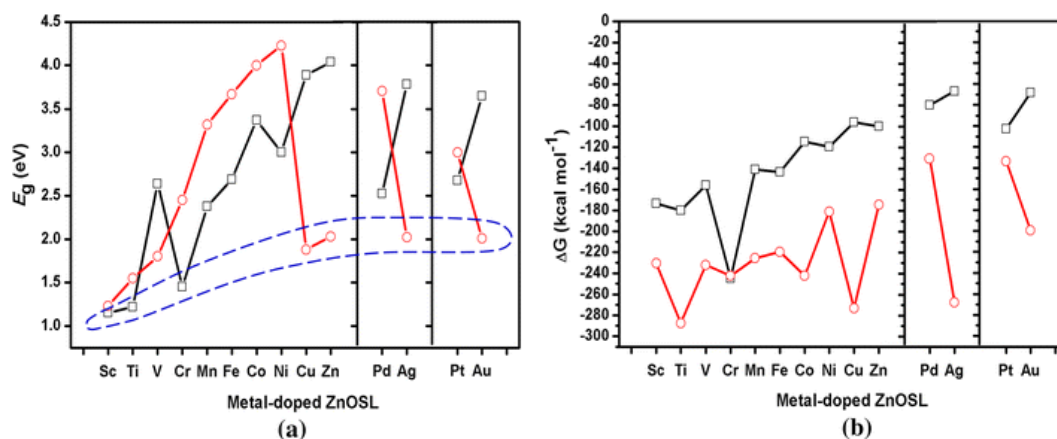


**Figure 4.4** Plots of energy gaps of (a) the low-spin (—□—) and high-spin (—○—) metal-doped ZnOSLs and (b) Gibbs free energy changes of the binding of metal dopant to Zn vacancy of the low-spin (—□—) and high-spin (—○—) Zn vacancy defect surfaces of ZnOSLs.

#### 4.4.2 Optimized structures of nonmetal-doped ZnOSLs and their energy gaps

The B3LYP/LanL2DZ-optimized structures of the low-spin B-, C-, N-, Si-, Al-, P-, Ga-, and Ge-doped ZnOSLs of which formulae are therefore  $Zn_{12}O_{11}B$ ,  $Zn_{12}O_{11}C$ ,  $Zn_{12}O_{11}N$ ,  $Zn_{12}O_{11}Si$ ,  $Zn_{12}O_{11}Al$ ,  $Zn_{12}O_{11}P$ ,  $Zn_{12}O_{11}Ga$ , and  $Zn_{12}O_{11}Ge$ , respectively, are shown in **Figure 4.5**. Plots of frontier orbitals of the low-spin state nonmetal-doped ZnOSLs are shown in **Figure 4.6** and their DOSs are shown in **Figure 4.7**.

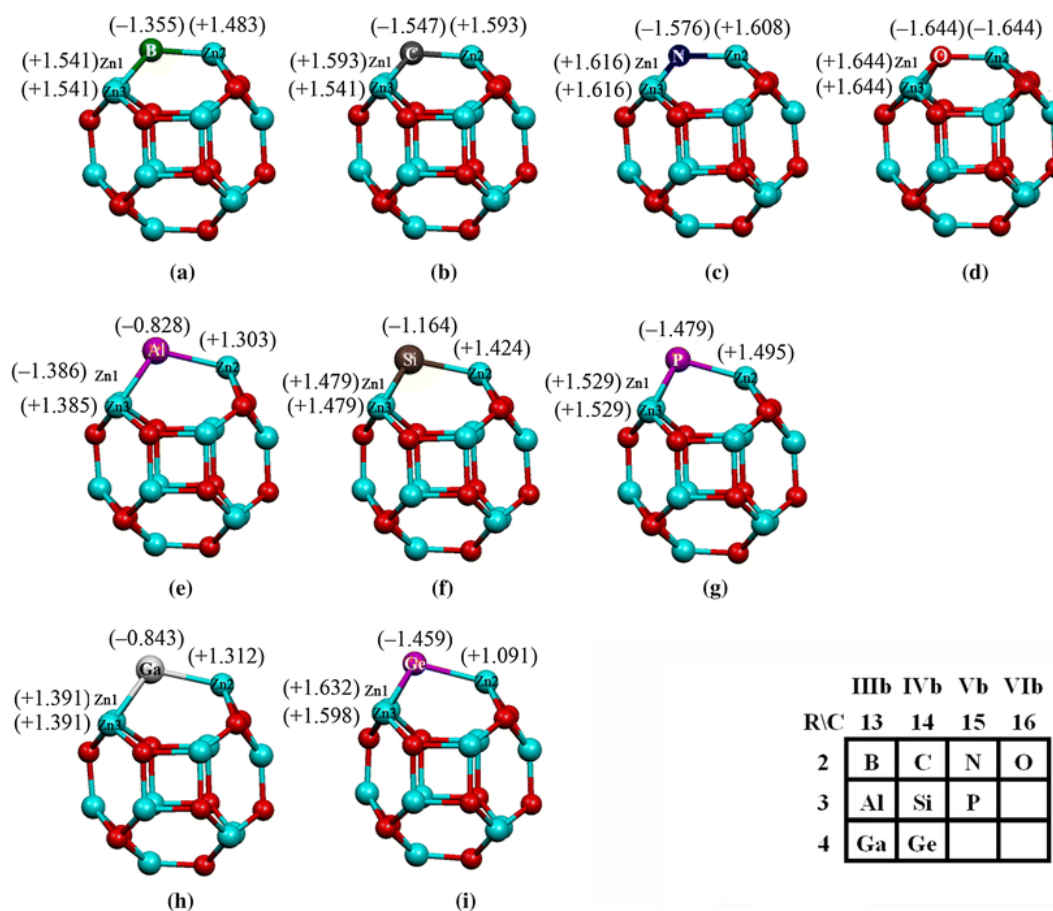


**Figure 4.5** B3LYP/LanL2DZ-optimized structures of the low-spin (a) B-, (b) C-, (c) N-doped ZnOSLs, (d) undoped ZnOSL, (e) Al-, (f) Si-, (g) P-, (h) Ga- and (i) Ge-doped ZnOSLs. The NBO charges for selected atoms are presented in e. All the nonmetal-doped ZnOSLs are shown based on the periodic table as noted on the bottom right side.

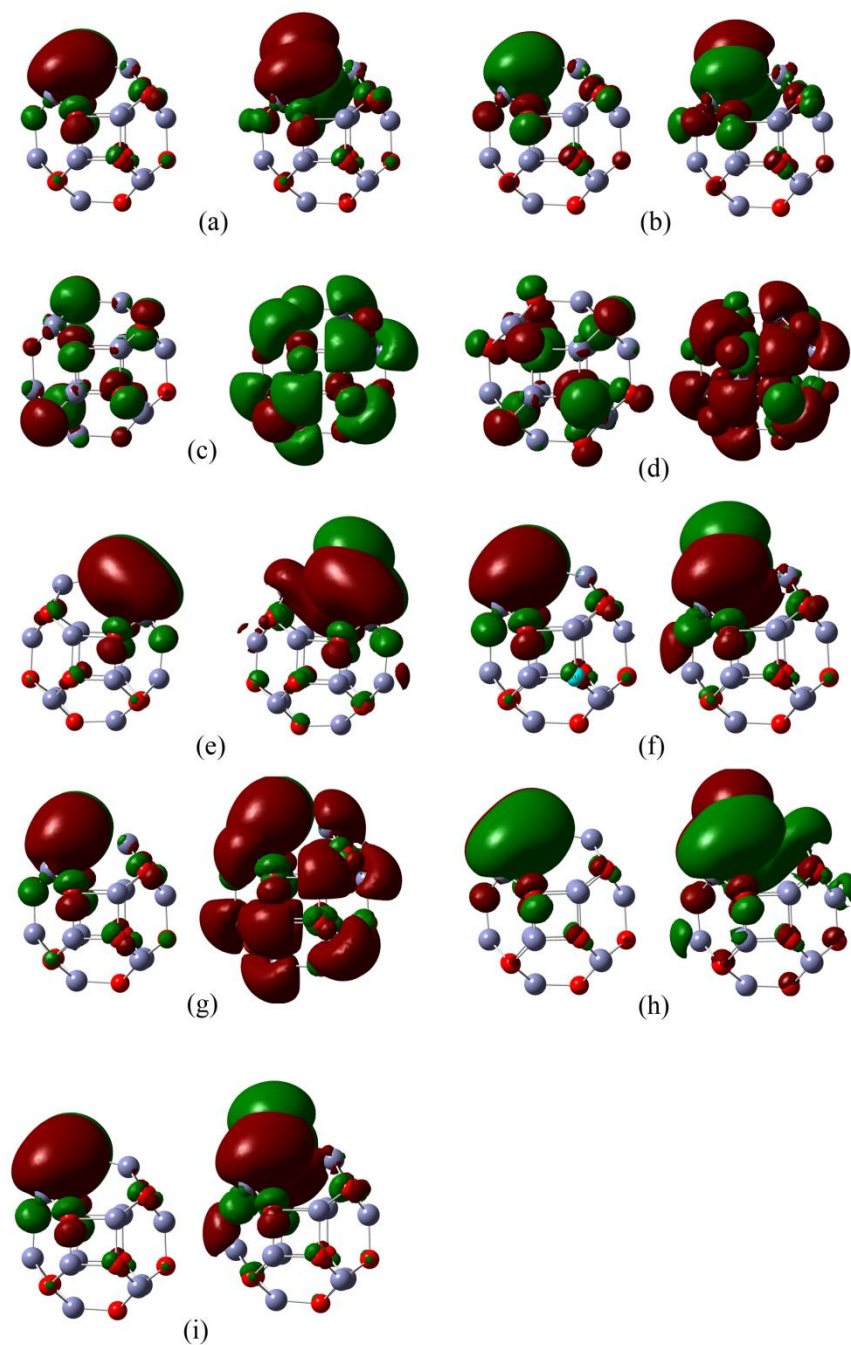


**Figure 4.6** Plots of the frontier orbitals of the low-spin (a) B-, (b) C-, (c) N-doped ZnOSLs, (d) undoped ZnOSL, (e) Al-, (f) Si-, (g) P-, (h) Ga- and (i) Ge-doped ZnOSLs. Left and right views are their HOMO and LUMO, respectively. All the orbitals of nonmetal-doped ZnOSLs are shown at the same positions of their corresponding structures shown in **Figure 4.5**

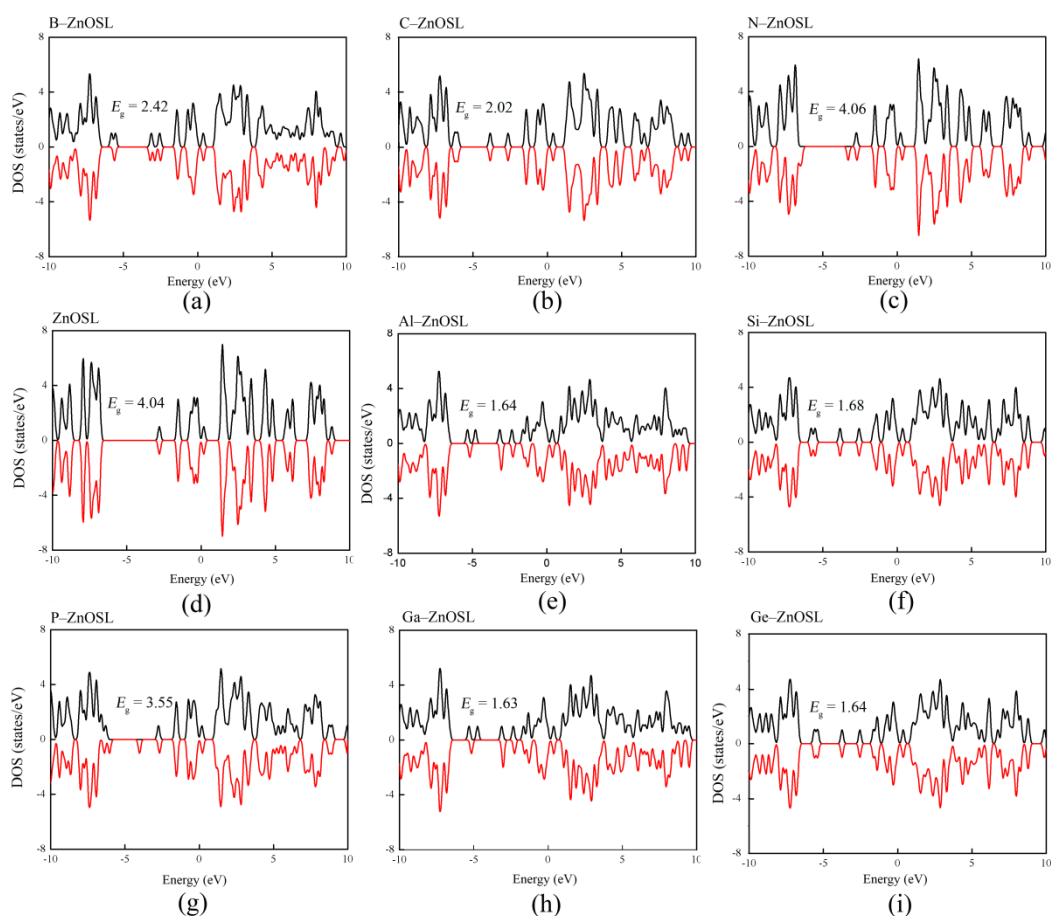


**Figure 4.7** DOSs of the low-spin (a) B-, (b) C-, (c) N-doped ZnOSLs, (d) undoped ZnOSL, (e) Al-, (f) Si-, (g) P-, (h) Ga- and (i) Ge-doped ZnOSLs. All the DOSs of nonmetal-doped ZnOSLs are shown at the same positions of their corresponding structures shown in **Figure 4.5**

SOMOs and HOMOs of all nonmetal-doped ZnOSL are located around dopant atom except for N-doped ZnOSL of which SOMO is inconsistently distributed over the molecule. LUMOs of all doped are located around their dopant atom, except N- and P-doped ZnOSLs of which LUMOs are distributed almost over the whole molecules. This means that N- and P-doped ZnOSLs are able to share LUMOs around their molecules to react with adsorbate. Plots of frontier orbitals and DOSs of the high-spin nonmetal-doped ZnOSLs are, respectively, shown in **Figure S4.3** and **Figure S4.4** in supplementary data. The selected geometrical parameters are shown in **Table S4.2** in

supplementary data which shows that Zn1–D, Zn2–D, and Zn3–D bond distances of all nonmetal–doped ZnOSLs are longer than the undoped ZnOSL. Plots of energy gaps of the low–spin and high–spin metal–doped ZnOSLs and Gibb’s free energy changes of binding of nonmetal dopant atom to  $O_V$  of the low–spin and high–spin O vacancy defect surfaces of ZnOSLs are shown in **Figure 4.8**

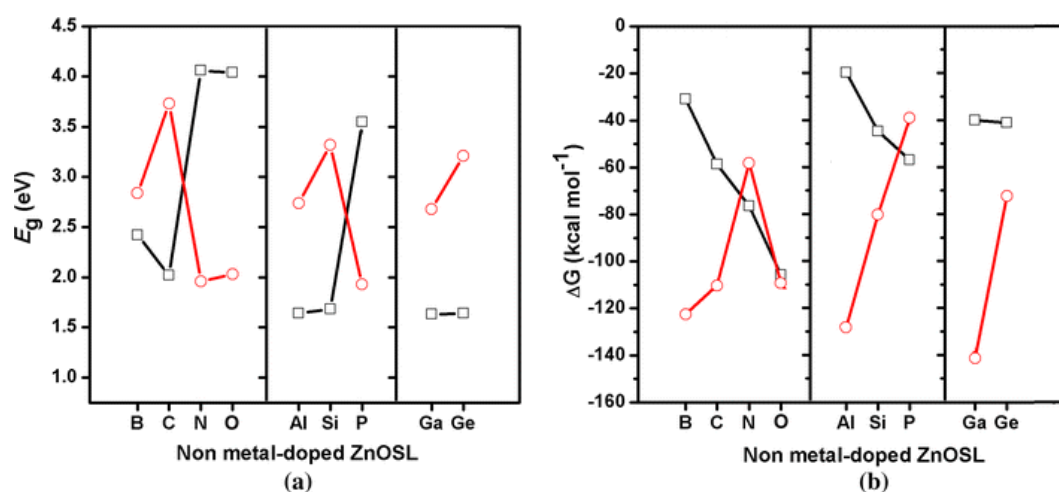


**Figure 4.8** Plots of energy gaps of (a) the low–spin (–□–) and high–spin (–○–) nonmetal–doped ZnOSLs and (b) Gibbs free energy changes of the binding of nonmetal dopant to O vacancy of the low–spin (–□–) and high–spin (–○–) O–vacancy defect surfaces of ZnOSLs

It shows that energy gaps of low–spin B–, Al–, and G–(group IIIB) and C–, Si– and Ge–(group IVB)–doped ZnOSLs are smaller than their high–spin structures but low–spin N– and P–(group VB) and O– (group VIB)–doped ZnOSLs are larger than their high–spin structures. Based on low–lying energy gap, the energy gaps of nonmetal–doped ZnOSLs are in decreasing order: B (D: 2.42 eV) > C (S: 2.02 eV) > O (T: 1.78 eV)  $\approx$  N (Q: 1.71 eV) > Si (S: 1.68 eV)  $\approx$  P (Q: 1.68 eV) > Al (D: 1.64 eV)  $\approx$  Ge (S: 1.64 eV)  $\approx$  Ga (D: 1.63 eV); S (singlet), D (doublet), T (triplet), and Q (quartet) symbols in parentheses are spin states of molecules. The most preferred doping process are binding of B, Al, and Ga (group IIIB elements) single

atom toward  $O_v$  position of high-spin oxygen vacancy ZnOSLs, see **Figure 4.8(b)**. It can be concluded that energy gaps of all the low-spin transition-metal-doped ZnOSLs are smaller than nonmetal-doped ZnOSL except for the undoped ZnOSL ( $E_g = 4.04$  eV) of which the gap is approximately equal to N-doped ZnOSL ( $E_g = 4.06$  eV). For the high-spin system, energy gaps of Sc-, Ti-, V-, Cu-, Ag-, and Au-doped ZnOSLs are smaller than undoped ZnOSL ( $E_g = 1.78$  eV). The energy gaps of high-spin N- and P-doped ZnOSLs were found to be smaller than undoped ZnOSL

#### 4.4.3 Metal and nonmetal binding for doping reactions

The energetics and thermodynamic properties of dopant atom binding to  $Zn_v$  of  $[ZnOSL + Zn_v]$  and  $O_v$  of  $[ZnOSL + O_v]$  are shown in **Table 4.3**. The binding abilities of these dopants to Zn vacancy for metal doping system and O vacancy for nonmetal doping system are in orders:  $Cr > Ti > Sc > V > Fe > Mn > Ni > Co > Pt > Zn > Cu > Pd > Au > Ag$  and  $O > N > C > P > Si > Ge > Ga > B > Al$ , respectively. Binding reactions for low-spin and high-spin state of all metal- and nonmetal-doped ZnOSLs are exothermic and spontaneous processes. The most favored binding reaction for metal doping is the binding of Cr and Ti for low-spin and high-spin state, respectively. The most favored binding reaction for nonmetal doping is binding of O and Ga for low-spin and high-spin state, respectively.

**Table 4.3** Energetic and thermodynamic properties of dopant atoms binding to  $Zn_V$  of  $[ZnOSL + Zn_V]$  for metal doping and  $O_V$  of  $[ZnOSL + O_V]$  for nonmetal doping, computed at the B3LYP/LanL2DZ level of theory.

Binding reaction	Ground state			Spin-polarized state		
	$\Delta E_{\text{binding}}^{\circ}$ <sup>a</sup>	$\Delta H_{\text{binding}}^{\circ}$ <sup>a</sup>	$\Delta G_{\text{binding}}^{\circ}$ <sup>a</sup>	$\Delta E_{\text{binding}}^{\circ}$ <sup>a</sup>	$\Delta H_{\text{binding}}^{\circ}$ <sup>a</sup>	$\Delta G_{\text{binding}}^{\circ}$ <sup>a</sup>
<i>Metal doped</i>						
$[ZnOSL + Zn_V] + Sc \rightarrow Sc\text{-doped ZnOSL}$	-177.59	-177.68	-173.30	-241.12	-242.70	-230.57
$[ZnOSL + Zn_V] + Ti \rightarrow Ti\text{-doped ZnOSL}$	-184.86	-185.24	-179.99	-297.41	-298.06	-287.54
$[ZnOSL + Zn_V] + V \rightarrow V\text{-doped ZnOSL}$	-160.27	-160.74	-155.79	-239.66	-239.30	-232.24
$[ZnOSL + Zn_V] + Cr \rightarrow Cr\text{-doped ZnOSL}$	-250.26	-250.77	-245.07	-254.36	-255.83	-242.28
$[ZnOSL + Zn_V] + Mn \rightarrow Mn\text{-doped ZnOSL}$	-145.65	-145.88	-141.03	-236.84	-238.23	-225.58
$[ZnOSL + Zn_V] + Fe \rightarrow Fe\text{-doped ZnOSL}$	-148.34	-148.67	-143.25	-232.23	-233.69	-219.72
$[ZnOSL + Zn_V] + Co \rightarrow Co\text{-doped ZnOSL}$	-119.87	-120.36	-114.64	-251.90	-252.41	-242.38
$[ZnOSL + Zn_V] + Ni \rightarrow Ni\text{-doped ZnOSL}$	-125.38	-126.13	-119.73	-192.15	-193.14	-181.13
$[ZnOSL + Zn_V] + Cu \rightarrow Cu\text{-doped ZnOSL}$	-101.37	-101.86	-96.16	-281.09	-281.15	-273.09
$[ZnOSL + Zn_V] + Zn \rightarrow ZnOSL^b$	-105.23	-105.57	-100.05	-186.28	-188.18	-174.61
$[ZnOSL + Zn_V] + Pd \rightarrow Pd\text{-doped ZnOSL}$	-85.23	-85.59	-80.12	-144.69	-145.85	-131.17
$[ZnOSL + Zn_V] + Ag \rightarrow Ag\text{-doped ZnOSL}$	-71.69	-71.92	-66.79	-278.73	-278.99	-268.33
$[ZnOSL + Zn_V] + Pt \rightarrow Pt\text{-doped ZnOSL}$	-107.97	-108.28	-102.98	-146.16	-147.73	-133.46
$[ZnOSL + Zn_V] + Au \rightarrow Au\text{-doped ZnOSL}$	-73.51	-73.72	-68.55	-209.71	-210.14	-199.43
<i>Nonmetal doped</i>						
$[ZnOSL + O_V] + B \rightarrow B\text{-doped ZnOSL}$	-35.12	-35.40	-30.96	-131.90	-132.91	-122.53
$[ZnOSL + O_V] + C \rightarrow C\text{-doped ZnOSL}$	-63.72	-64.44	-58.59	-119.76	-120.65	-110.28
$[ZnOSL + O_V] + N \rightarrow N\text{-doped ZnOSL}$	-81.64	-82.41	-76.44	-65.90	-65.99	-58.05
$[ZnOSL + O_V] + O \rightarrow ZnOSL^b$	-110.98	-111.79	-105.63	-119.79	-121.49	-109.38
$[ZnOSL + O_V] + Al \rightarrow Al\text{-doped ZnOSL}$	-24.11	-24.40	-19.56	-136.79	-136.80	-128.03
$[ZnOSL + O_V] + Si \rightarrow Si\text{-doped ZnOSL}$	-49.08	-49.24	-44.66	-89.06	-89.29	-80.01
$[ZnOSL + O_V] + P \rightarrow P\text{-doped ZnOSL}$	-61.83	-62.03	-56.81	-49.43	-49.82	-38.91
$[ZnOSL + O_V] + Ga \rightarrow Ga\text{-doped ZnOSL}$	-44.72	-44.93	-39.93	-150.10	-149.95	-141.23
$[ZnOSL + O_V] + Ge \rightarrow Ge\text{-doped ZnOSL}$	-45.28	-45.30	-40.91	-81.50	-81.50	-72.30

<sup>a</sup> In kcal/mol.

<sup>b</sup> Identical to undoped ZnOSL cage.

#### 4.4.4 NBO charge analysis for metal- and nonmetal-doped ZnOSL

The selected NBO charges (in e) of low-spin and high-spin undoped and metal-doped ZnOSLs are shown in **Table 4.4** and **Table 4.5**, respectively. It shows that in both low-spin and high-spin metal-doped ZnOSLs, charge transfers from dopant to the rest part of molecule for all the metal-doped ZnOSLs as compared with atomic charge of Zn atom in undoped ZnOSL are preferred. On the other hand, in both low-spin and high-spin nonmetal-doped ZnOSLs, charge transfers from molecule of nonmetal-doped ZnOSL to its dopant as compared with partial charge of O atom in undoped ZnOSL are preferred. All the metal dopant atoms are as electron acceptor but all the nonmetal dopant atoms are electron donor.



**Table 4.4** Selected NBO charges (in e) of metal- and nonmetal-doped ZnOSLs, computed at the B3LYP/LanL2DZ level of theory.

Doped ZnOSL	Partial charge <sup>a</sup>			PCT <sup>b</sup>	
	O1	O2	O3	Dopant	
<i>Metal doped</i>					
Sc-doped ZnOSL	-1.452	-1.467	-1.467	1.574	-0.070
Ti-doped ZnOSL	-1.294	-1.304	-1.306	0.849	-0.795
V-doped ZnOSL	-1.341	-1.347	-1.347	1.176	-0.468
Cr-doped ZnOSL	-1.401	-1.390	-1.390	0.966	-0.678
Mn-doped ZnOSL	-1.466	-1.485	-1.485	1.187	-0.457
Fe-doped ZnOSL	-1.433	-1.443	-1.443	1.060	-0.584
Co-doped ZnOSL	-1.521	-1.479	-1.479	1.178	-0.466
Ni-doped ZnOSL	-1.519	-1.404	-1.404	1.023	-0.621
Cu-doped ZnOSL	-1.572	-1.500	-1.491	1.252	-0.392
Zn-doped ZnOSL <sup>c</sup>	-1.644	-1.643	-1.644	1.644	0.000
Pd-doped ZnOSL	-1.393	-1.338	-1.390	0.826	-0.818
Ag-doped ZnOSL	-1.266	-1.123	-1.247	0.808	-0.836
Pt-doped ZnOSL	-1.337	-1.299	-1.306	0.638	-1.006
Au-doped ZnOSL	-1.223	-1.114	-1.232	0.690	-0.954
<i>Non metal doped</i>					
B-doped ZnOSL	1.541	1.483	1.541	-1.355	0.288
C-doped ZnOSL	1.593	1.574	1.593	-1.547	0.096
N-doped ZnOSL	1.616	1.608	1.616	-1.576	0.067
O-doped ZnOSL <sup>c</sup>	1.644	1.644	1.644	-1.643	0.000
Al-doped ZnOSL	1.386	1.303	1.385	-0.828	0.815
Si-doped ZnOSL	1.479	1.424	1.479	-1.164	0.479
P-doped ZnOSL	1.529	1.495	1.529	-1.299	0.344
Ga-doped ZnOSL	1.391	1.312	1.391	-0.843	0.800
Ge-doped ZnOSL	1.459	1.388	1.459	-1.091	0.552

<sup>a</sup> In e.

<sup>b</sup> Partial charge transfer, defined as difference between partial charge of dopant and Zn of undoped ZnOSL for metal doping system or O of undoped ZnOSL for nonmetal doping system.

<sup>c</sup> Identical to undoped ZnOSL cage.

**Table 4.5** Selected NBO charges (in e) of high-spin metal- and nonmetal-doped ZnOSLs, computed at the B3LYP/LanL2DZ level of theory

Doped ZnOSL	Partial charge <sup>a</sup>			PCT <sup>a</sup>	
	O1	O2	O3	Dopant	
<i>Metal doped</i>					
Sc-doped ZnOSL	-1.452	-1.478	-1.473	1.350	-0.224
Ti-doped ZnOSL	-1.313	-1.319	-1.319	1.313	-0.261
V-doped ZnOSL	-1.421	-1.417	-1.417	1.103	-0.471
Cr-doped ZnOSL	-1.448	-1.436	-1.436	1.051	-0.523
Mn-doped ZnOSL	-1.439	-1.395	-1.395	0.997	-0.577
Fe-doped ZnOSL	-1.489	-1.491	-1.474	1.163	-0.411
Co-doped ZnOSL	-1.539	-1.541	-1.541	1.321	-0.253
Ni-doped ZnOSL	-1.530	-1.539	-1.539	1.304	-0.270
Cu-doped ZnOSL	-1.153	-1.334	-1.335	1.219	-0.355
Zn-doped ZnOSL <sup>c</sup>	-1.536	-1.617	-1.534	1.574	0.000
Pd-doped ZnOSL	-1.405	-1.446	-1.441	0.987	-0.587
Ag-doped ZnOSL	-1.031	-1.252	-1.249	0.841	-0.733
Pt-doped ZnOSL	-1.328	-1.408	-1.407	0.826	-0.748
Au-doped ZnOSL	-1.210	-1.246	-1.245	0.674	-0.900
	Zn1	Zn2	Zn3	Dopant	
<i>Non metal doped</i>					
B-doped ZnOSL	1.535	1.508	1.535	-1.370	0.256
C-doped ZnOSL	1.594	1.559	1.594	-1.507	0.119
N-doped ZnOSL	1.412	1.509	1.404	-0.860	0.766
O-doped ZnOSL <sup>c</sup>	1.584	1.585	1.581	-1.626	0.000
Al-doped ZnOSL	1.363	1.302	1.363	-0.772	0.854
Si-doped ZnOSL	1.483	1.413	1.483	-1.125	0.501
P-doped ZnOSL	1.351	1.416	1.351	-0.658	0.968
Ga-doped ZnOSL	1.356	1.299	1.356	-0.756	0.870
Ge-doped ZnOSL	1.457	1.384	1.457	-1.044	0.582

a In e.

b Partial charge transfer, defined as difference between partial charge of dopant and Zn of undoped ZnOSL for metal doping system or O of undoped ZnOSL for nonmetal doping system.

c Identical to undoped ZnOSL cage.

## 4.5 CONCLUSION

The optimized structures of the low-spin ZnOSLs doped by single transition-metal atoms (Sc, Ti, V, Cr, Mn, Fe, Co, Ni, Cu, Pd, Ag, Pt and Au) and single nonmetal atoms (B, C, N, Al, Si, P, Ga and Ge) were obtained using DFT/B3LYP method. The binding abilities of these dopants to Zn vacancy for metal doping system and O vacancy for nonmetal doping system are in orders: Cr > Ti > Sc > V > Fe > Mn > Ni > Co > Pt > Zn > Cu > Pd > Au > Ag and O > N > C > P > Si > Ge > Ga > B > Al, respectively. The metal-doped ZnOSLs which have remarkably low energy gaps are in following order: low-spin Sc- < Ti- < Cr-doped ZnOSLs < high-spin Cu- < Zn-  $\approx$  Ag-  $\approx$  Au-doped ZnOSLs. It may be concluded that the Sc-, Ti-, and Cr-doped ZnOSLs can be conducting material, and the V-, Cu-, Ag-, and Au-doped and undoped ZnOSLs can be employed as photocatalysts. Based on low-lying energy gap, energy gaps of nonmetal-doped ZnOSLs are in order: B (D: 2.42 eV) > C (S: 2.02 eV) > O (T: 1.78 eV)  $\approx$  N (Q: 1.71 eV) > Si (S: 1.68 eV) = P (Q: 1.68 eV) > Al (D: 1.64 eV)  $\approx$  Ge (S: 1.64 eV)  $\approx$  Ga (D: 1.63 eV).



## 4.6 SUPPLEMENTARY DATA

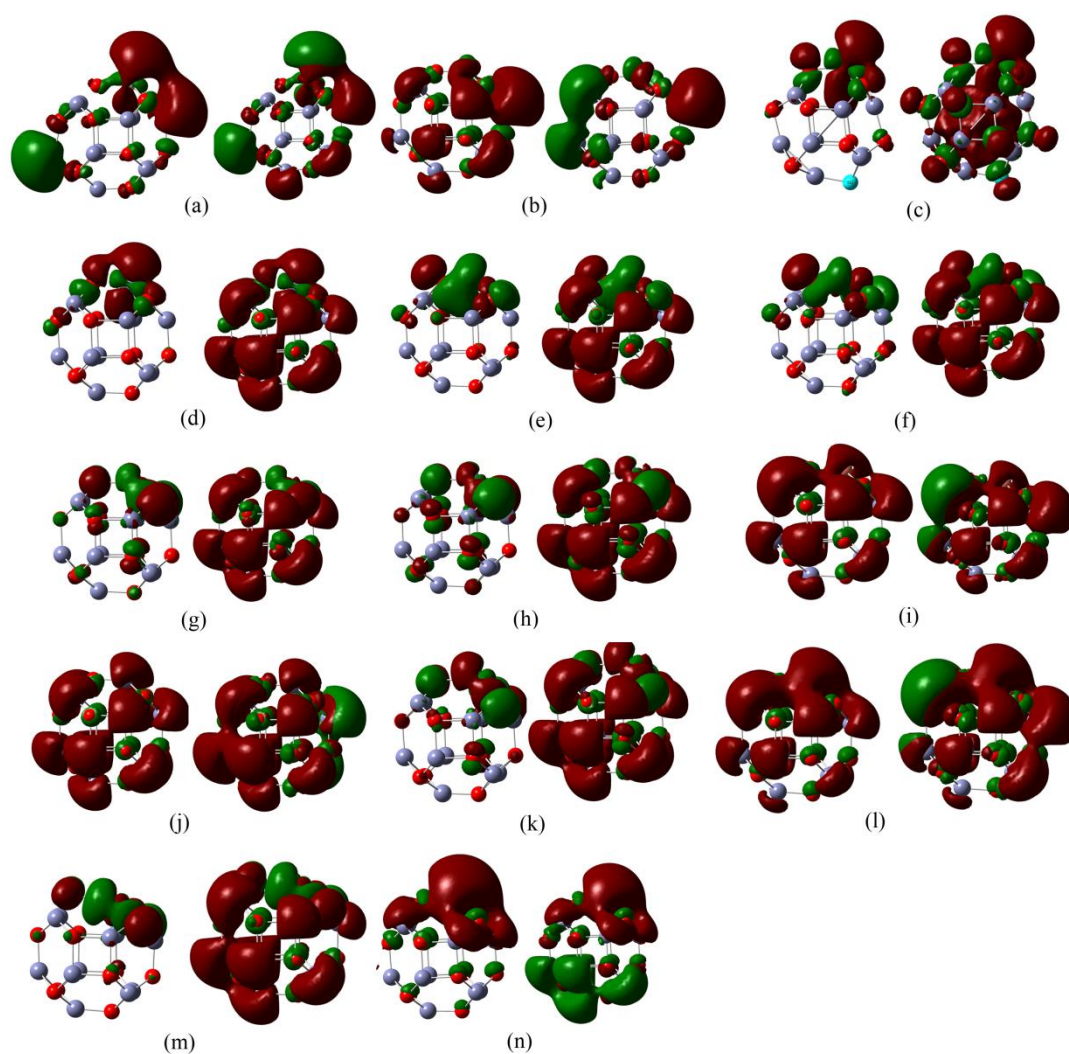


**Figure S4.1** Plots of frontier orbitals of the high-spin (a) Sc-, (b) Ti-, (c) V-, (d) Cr-, (e) Mn-, (f) Fe-, (g) Co-, (h) Ni-, (i) Cu-doped ZnOSLs, (j) undoped ZnOSL, (k) Pd-, (l) Ag-, (m) Pt- and (n) Au-doped ZnOSLs. All the orbitals of metal-doped ZnOSLs are shown at the same positions of their corresponding structures shown in **Figure 4.1**.

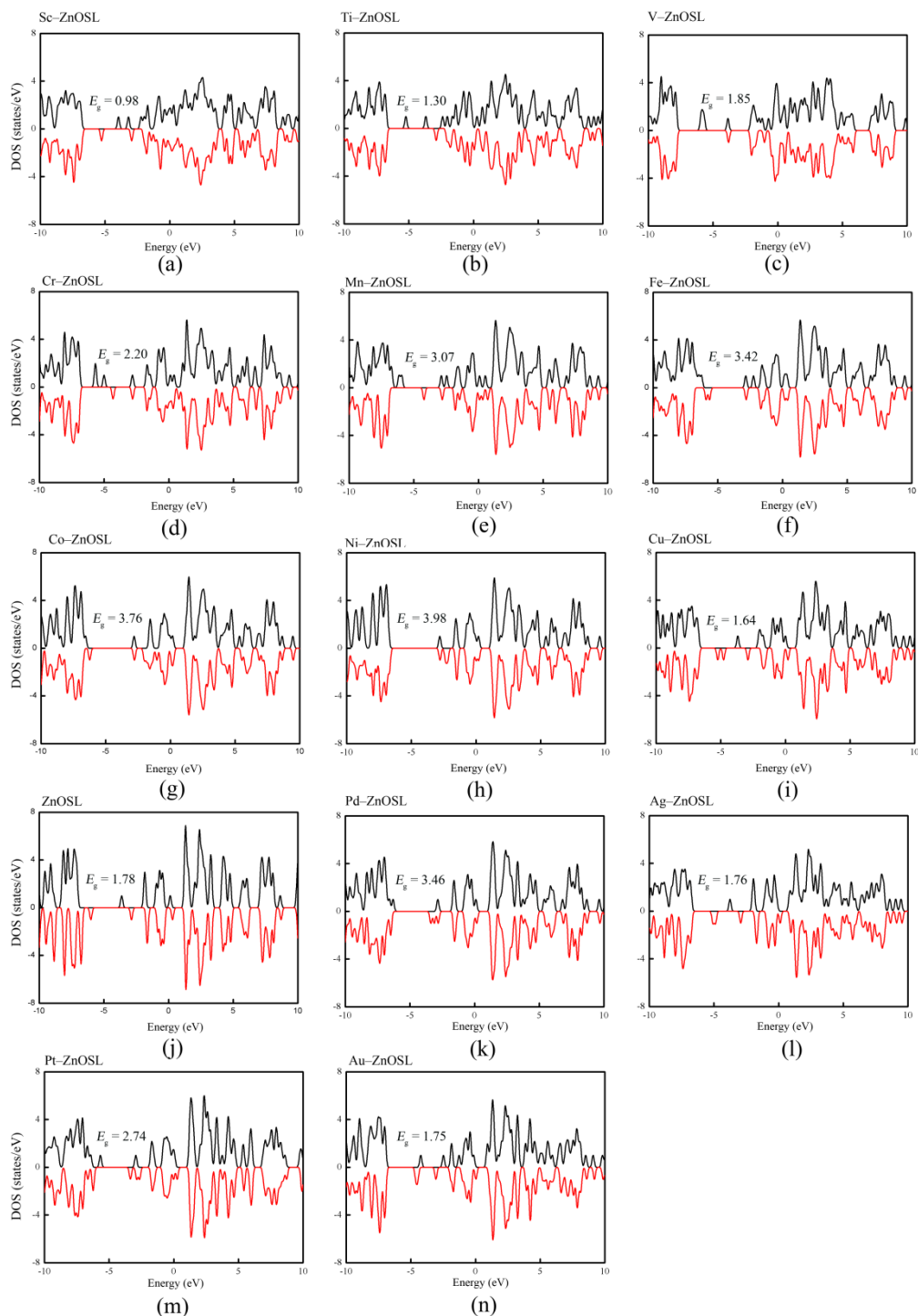


**Figure S4.2** DOSs of the high-spin (a) Sc-, (b) Ti-, (c) V-, (d) Cr-, (e) Mn-, (f) Fe-, (g) Co-, (h) Ni-, (i) Cu-doped ZnOSLs, (j) undoped ZnOSL, (k) Pd-, (l) Ag-, (m) Pt- and (n) Au-doped ZnOSLs. All the DOSs of metal-doped ZnOSLs are shown at the same positions of their corresponding structures shown in **Figure 4. 1**.

**Table S4.1** Selected geometrical data for the metal–doped ZnOSLs, computed at the B3LYP/LanL2DZ level of theory.

<b>Doped ZnOSL</b>	<b>Bond distance (Å )</b>			<b>Bond angle(deg.)</b>		
	<b>O1–D<sup>a,b</sup></b>	<b>O2–D<sup>a,b</sup></b>	<b>O3–D<sup>a,b</sup></b>	<b>O1–D–O2<sup>a,b</sup></b>	<b>O2–D–O3<sup>a,b</sup></b>	<b>O3–D–O1<sup>a,b</sup></b>
Sc–doped ZnOSL	1.8994	1.9406	1.9408	112.09	90.95	112.07
Ti–doped ZnOSL	1.8418	1.8586	1.8597	127.22	98.58	127.32
V–doped ZnOSL	1.9574	1.9640	1.9640	116.16	90.73	116.16
Cr–doped ZnOSL	1.8579	1.9272	1.9272	123.56	85.58	123.56
Mn–doped ZnOSL	1.8527	1.9247	1.9247	123.68	88.38	123.68
Fe–doped ZnOSL	1.8456	1.9076	1.9065	118.64	90.29	118.56
Co–doped ZnOSL	1.8825	1.8957	1.8957	126.57	89.08	126.57
Ni–doped ZnOSL	1.8815	1.8730	1.8731	132.99	89.22	133.17
Cu–doped ZnOSL	1.8964	1.9420	1.9414	129.27	89.35	129.04
ZnOSL	1.9112	1.9847	1.9854	123.37	90.88	123.36
Pd–doped ZnOSL	2.0433	2.0432	2.0853	111.36	84.30	157.98
Ag–doped ZnOSL	2.1204	2.2399	2.1855	117.12	82.11	144.61
Pt–doped ZnOSL	2.0071	2.0587	2.0662	138.79	79.21	140.91
Au–doped ZnOSL	2.0755	2.2977	2.1525	122.35	79.93	150.98

<sup>a</sup> O1, O2 and O3 are atoms on the ZnOSL which are defined in **Figure 4.1**.

<sup>b</sup> D is atom of dopant which is doped on the ZnOSL.

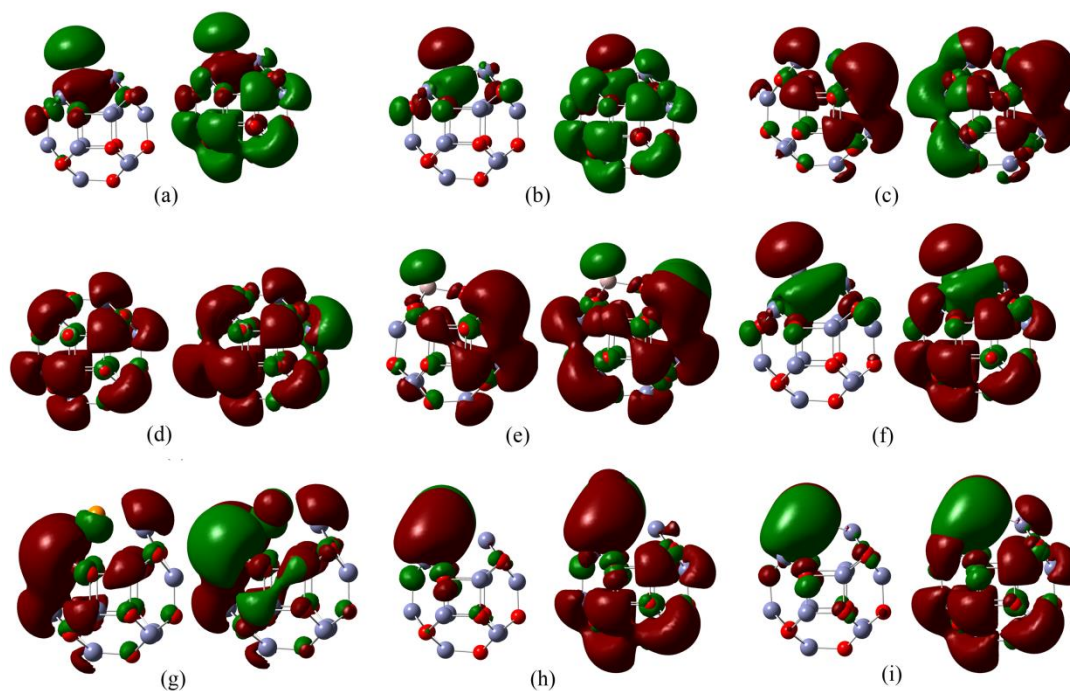


**Figure S4.3** Plots of the frontier orbitals of the high-spin (a) B-, (b) C-, (c) N-doped ZnOSLs, (d) ZnOSL, (e) Al-, (f) Si-, (g) P-, (h) Ga- and (i) Ge-doped ZnOSLs. Left and right views are their HOMO and LUMO, respectively. All the orbitals of non metal-doped ZnOSLs are shown at the same positions of their corresponding structures shown in **Figure 4.5**.

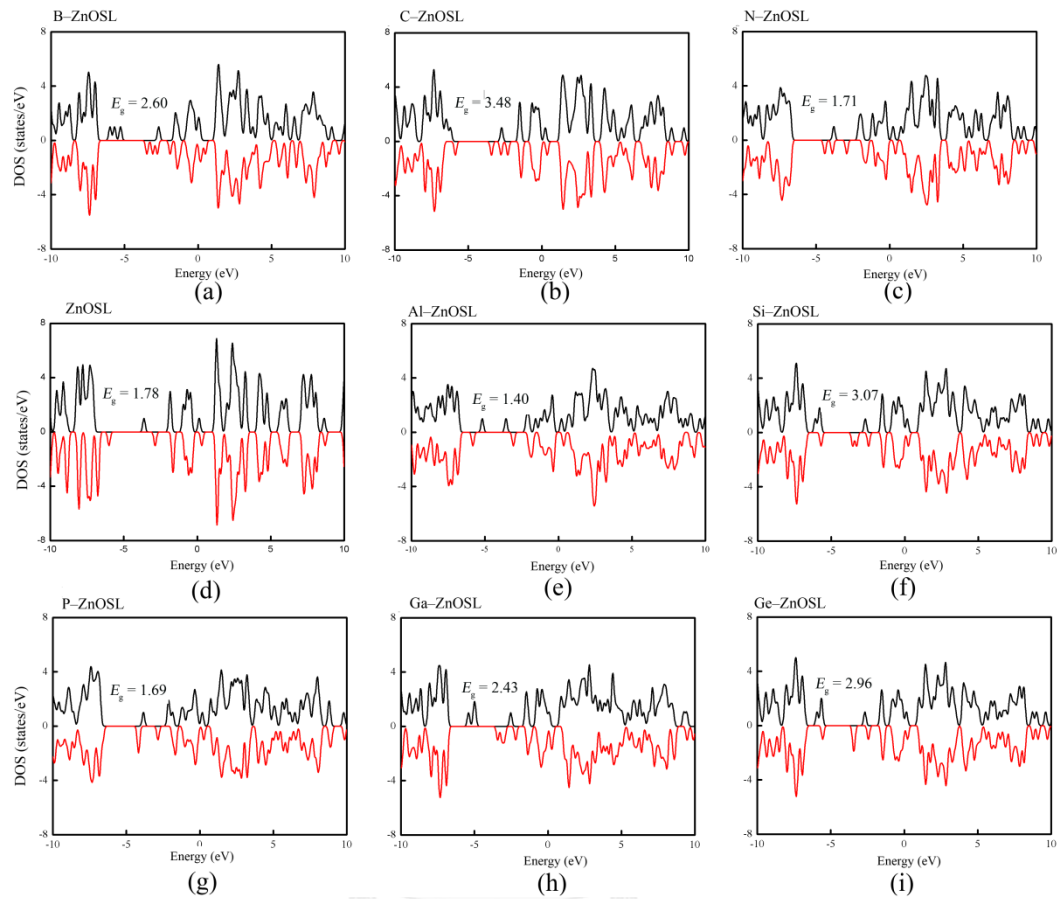


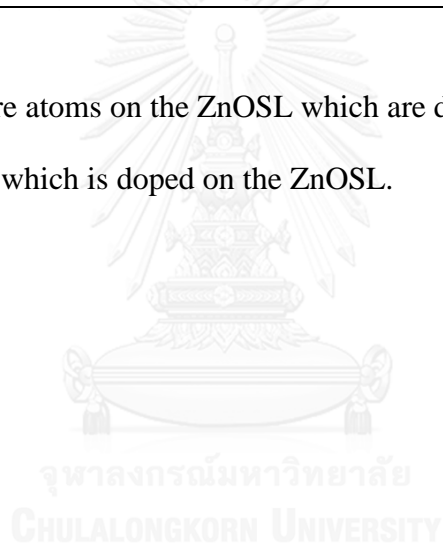
**Figure S4.4** DOSs of the high-spin (a) B-, (b) C-, (c) N-doped ZnOSLs, (d) ZnOSL, (e) Al-, (f) Si-, (g) P-, (h) Ga- and (i) Ge-doped ZnOSLs. All the DOSs of non metal-doped ZnOSLs are shown at the same positions of their corresponding structures shown in **Figure 4.5**.

**Table S4.2** Selected geometrical data for the undoped and nonmetal-doped ZnOSLs, computed at the B3LYP/LanL2DZ level of theory.

<b>Doped ZnOSL</b>	<b>Bond distance (Å)</b>			<b>Bond angle(deg.)</b>		
	<b>Zn1-D<sup>a,b</sup></b>	<b>Zn2-D<sup>a,b</sup></b>	<b>Zn3-D<sup>a,b</sup></b>	<b>Zn1-D-Zn2<sup>a,b</sup></b>	<b>Zn2-D-Zn3<sup>a,b</sup></b>	<b>Zn3-D-Zn1<sup>a,b</sup></b>
<i>Nonmetal doped</i>						
B-doped ZnOSL	2.3309	2.1708	2.3311	118.78	118.75	74.15
C-doped ZnOSL	2.1215	2.0832	2.1212	115.57	115.60	88.75
N-doped ZnOSL	2.0453	1.9834	2.0454	116.01	116.04	88.09
ZnOSL	1.9847	1.9101	1.9844	116.42	116.44	88.84
Al-doped ZnOSL	2.7575	2.5948	2.7575	107.95	107.99	65.22
Si-doped ZnOSL	2.5147	2.5016	2.5147	104.60	104.60	80.91
P-doped ZnOSL	2.5020	2.4394	2.5021	100.07	100.08	75.16
Ga-doped ZnOSL	2.7391	2.5653	2.7389	109.46	109.51	65.97
Ge-doped ZnOSL	2.5689	2.5732	2.5689	102.37	102.36	81.25

<sup>a</sup> Zn1, Zn2 and Zn3 are atoms on the ZnOSL which are defined in **Figure 4.1**.

<sup>b</sup> D is atom of dopant which is doped on the ZnOSL.



**CHAPTER V**  
**DFT INVESTIGATION ON ADSORPTION OF DI-, TRI- AND**  
**TETRA-ATOMIC GASES ON Sc-DOPED ZnO SODALITE LIKE**  
**CAGE FOR GAS SENSING PURPOSE**

Waranyu Pipornpong, Supho Phunnarungsi, Vithaya Ruangpornvisuti

This article has been submitted

### **5.1 ABSTRACT**

Structural optimizations for adsorption configurations of di-, tri- and polyatomic gases on Sc-ZnOSL were carried out using the DFT/B3LYP/GEN method. Energetics, enthalpies and Gibbs free energies of gas adsorptions were obtained. Adsorption of SO<sub>2</sub> on the Sc-ZnOSL was found to be the most energetically preferred configuration. Use of the Sc-ZnOSL as SO<sub>2</sub> storage material was suggested. Since, energy gaps for the Sc-ZnOSL and its adsorption configurations were analyzed as a function of electrical conductivity, it was found that the largest decrease of energy gap was taken place after bridge-structured adsorption of N<sub>2</sub>O on the Sc-ZnOSL. The Sc-ZnOSL used as N<sub>2</sub>O or SO<sub>2</sub> sensing material was suggested.

### **5.2 INTRODUCTION**

There are various fundamental gases in the atmosphere not only useful gases but also toxic gases. Hence, gas adsorption material has been getting more and more concerning topic that many researchers focus for many decades. The great interest material using for gas sensor is metal oxide nanoparticle (NP) such as SnO<sub>2</sub>, ZnO,

TiO<sub>2</sub>, ZrO<sub>2</sub>, and CeO<sub>2</sub> [116-118]. Among metal oxide NP, ZnO nanoparticle (ZnONP) is very attractive material because of its large surface-to-volume ratio, large specific surface area and outstanding charge carrier transfer [119, 120]. Moreover, different morphology of ZnONP showed different selectivity. Hamedani, et.al reported that CO highly responded to flower-like ZnO, while methane highly responded to the ZnO nanorod [121]. ZnONP particularly showed a distinctly gas selectivity while compared to the films [122]. Kukreja L.M. and et.al. synthesized ZnO nanoparticle as (ZnO)<sub>n</sub> cluster with n=1–20 and experimentally proven by mass spectroscopy [123]. Also, Castañeda, L. can prepared the ZnO nanocages which suitable for gas sensors by simple experimental technique [48]. Recently, theoretical calculation have been explored the geometric structure and electronic properties of (ZnO)<sub>n</sub> cluster with various sizes [104, 124-128]. Many researchers founded that (ZnO)<sub>12</sub> as ZnOSL is more favorable phase than other ZnO polymorphs [128-130]. Due to ZnOSL, it is stable and has many active sites on symmetric cage. Despite its dominant features like shape-selective property and well-defined microporous network making them attractive for catalysis, it has been less mentioned. In our previous work, the structure of ZnOSL was optimized and its good adsorption configurations with various gases were reported [23]. We also showed that doping ZnOSL with different metal and non-metal affect to the energy gap of ZnOSL [131]. Furthermore, the experimental results showed that gas sensors based on doping ZnO, such as Pt, Pd and Ag enhanced the gas adsorption activity by reducing the energy gap [132-134], but they are expensive. The Al-doped ZnOSL optimization was selective for CO gas molecule due to the energy gap decreasing and resistivity change. According to the experimental work, increasing the Al doping concentration enhanced the CO adsorption activity [135]. Various doping were reported; however, Sc-ZnOSL had the smallest energy gap compared with others [131]. Moreover, Sc ion particle size exactly fits to the size of Zn ion [136]. There is no report about the gas adsorption on Sc-ZnOSL. Here we perform DFT calculation to investigate the adsorption properties of di-atomic (H<sub>2</sub>, N<sub>2</sub>, O<sub>2</sub>, CO, NO), tri-atomic (CO<sub>2</sub>, N<sub>2</sub>O, NO<sub>2</sub>, H<sub>2</sub>O, SO<sub>2</sub>), and tetra-atomic (NH<sub>3</sub>) gases on Sc-doped ZnOSL using density functional theory. The adsorption energies, thermodynamic properties and charge transfer from various active sites have been reported.

### 5.3 COMPUTATIONAL DETAILS

Full optimizations of structure of Sc–ZnOSL cage (ScZn<sub>11</sub>O<sub>12</sub> cluster) and adsorption configurations of gases H<sub>2</sub>, N<sub>2</sub>, O<sub>2</sub>, CO, NO, CO<sub>2</sub>, N<sub>2</sub>O, NO<sub>2</sub>, H<sub>2</sub>O, SO<sub>2</sub> and NH<sub>3</sub> on the Sc–ZnOSL were carried out using density functional theory (DFT) method. Optimizations for single molecule adsorptions of NO and NO<sub>2</sub>, their total electronic states of doublet (spin multiplicity = 2) state were employed. DFT calculations have been performed with hybrid density functional B3LYP, the Becke's three-parameter exchange functional [99] with the Lee–Yang–Parr correlation functional [100], using the Los Alamos LanL2DZ split-valence basis set [137-139] for zinc atom and 6–31G(d,p) basis set [140] for remaining atoms. Calculations were performed with the GAUSSIAN 09 program [141]. All optimized structures and their electronic properties referred in this paper were obtained using the B3LYP/GEN calculations which GEN keyword was used to specify basis sets to atoms as mentioned above.

The adsorption energy ( $\Delta E_{\text{ads}}$ ) for single molecule of gas adsorbed on the Sc–ZnOSL cluster has been obtained using (5.1)

$$\Delta E_{\text{ads}}(\text{gas}) = E(\text{gas}/\text{Sc–ZnOSL}) - [E(\text{Sc–ZnOSL}) + E(\text{gas})] \quad (5.1)$$

where  $E(\text{gas}/\text{Sc–ZnOSL})$  is the total energy of gas molecule adsorbed on the Sc–ZnOSL cluster,  $E(\text{gas})$  and  $E(\text{Sc–ZnOSL})$  are the total energies of isolated gas adsorbate and free Sc–ZnOSL cluster, respectively.

Adsorption configuration of gas molecule on the Sc–doped ZnOSL specified by underline symbol is denoted by i.e. CO/Sc–ZnOSL where CO gas adsorbed on the Sc–ZnOSL by pointing C atom toward Sc atom of Sc–ZnOSL. This notation means also that CO is located close to Sc atom which [C···Sc] distance is the shortest length.

## 5.4 RESULTS AND DISCUSSION

### 5.4.1 Structure optimizations

The B3LYP/GEN-optimized structures of Sc-ZnOSL and their adsorption structures with diatomic gases, H<sub>2</sub>, N<sub>2</sub>, O<sub>2</sub>, CO and NO are shown in **Figure 5.1** and **Figure 5.2**. The B3LYP/GEN-optimized structures of Sc-doped ZnOSL and their adsorption structures with triatomic gases N<sub>2</sub>O and NO<sub>2</sub>, H<sub>2</sub>O, CO<sub>2</sub>, SO<sub>2</sub> and tetraatomic gas NH<sub>3</sub> are shown in **Figure 5.3** and **Figure 5.4**. The shortest bond-distances between gas atoms and adsorption atom of the Sc-doped ZnOSL are shown in **Table 5.1**. There are two configurations of adsorption structures of Sc-doped ZnOSL and homonuclear diatomic gases, H<sub>2</sub>, N<sub>2</sub> and O<sub>2</sub> (**Figure 5.1**). One is the configuration of pointing their atom toward Sc dopant and the other is toward to O atom of Sc-doped ZnOSL. The adsorption structures of hetero diatomic gases, CO and NO, are consist of four configurations as shown in **Figure 5.2** and their interaction distances are shown in **Table 5.1**. There are four configurations of adsorption structures of the Sc-doped ZnOSL and N<sub>2</sub>O as pointing its (a) O toward Sc and N toward Zn, (b) N toward Sc, (c) O toward Zn and N toward Sc and (d) N toward Zn which correspond to their structures shown in **Figure 5.3**. Three configurations of the Sc-doped ZnOSL and NO<sub>2</sub> were found shown in **Figure 5.3** as pointing its (e) O toward Sc and O' toward Zn, (f) O toward Sc and (g) N toward Zn. Two adsorption configurations of NH<sub>3</sub> (triatomic gas) on the Sc-doped ZnOSL were found.

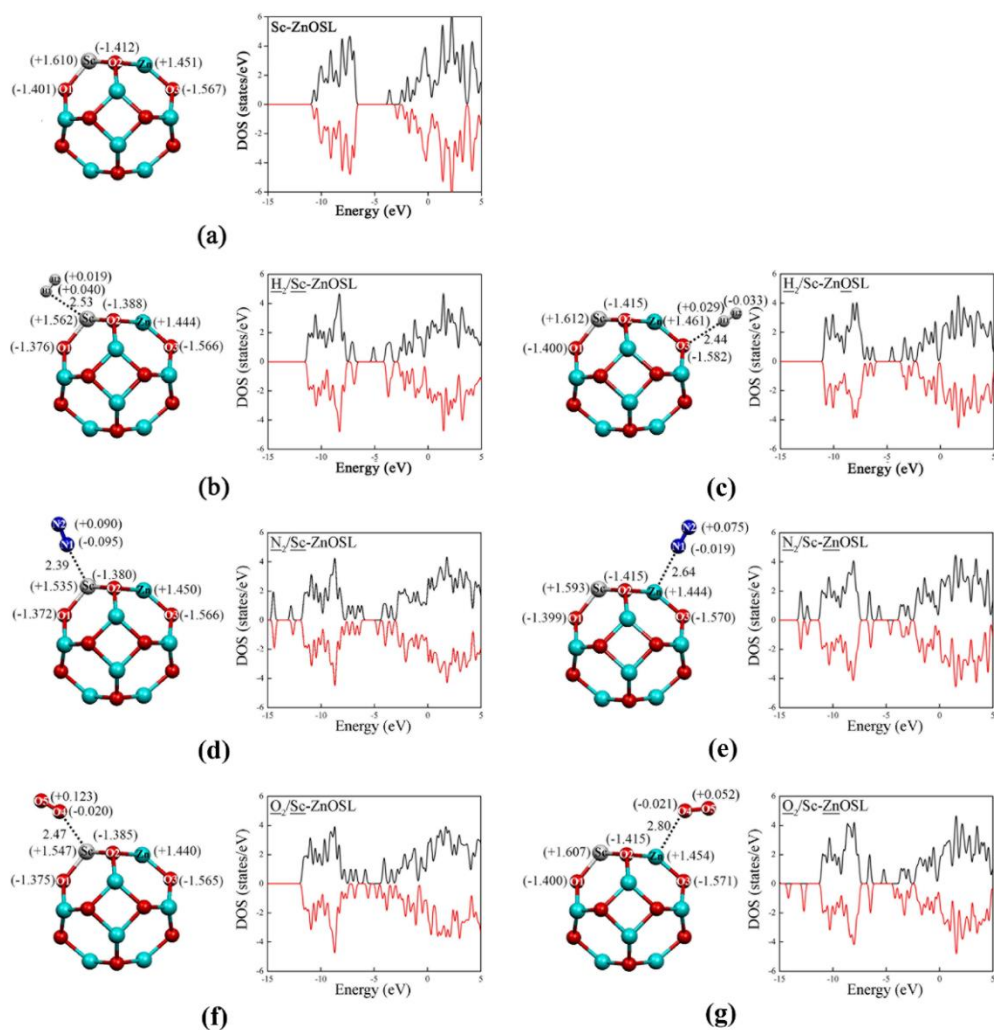


**Figure 5.1** The B3LYP/GEN-optimized structures of (a) Sc-doped ZnOSL, their adsorption structures with (b) H<sub>2</sub> (toward Sc), (c) H<sub>2</sub> (toward O), (d) N<sub>2</sub> (toward Sc), (e) N<sub>2</sub> (toward Zn), (f) O<sub>2</sub> (toward Sc) and (g) O<sub>2</sub> (toward Zn). Plots for their density of states are located beside their images. NBO atomic charges are in parentheses. Bond distances are in Å.

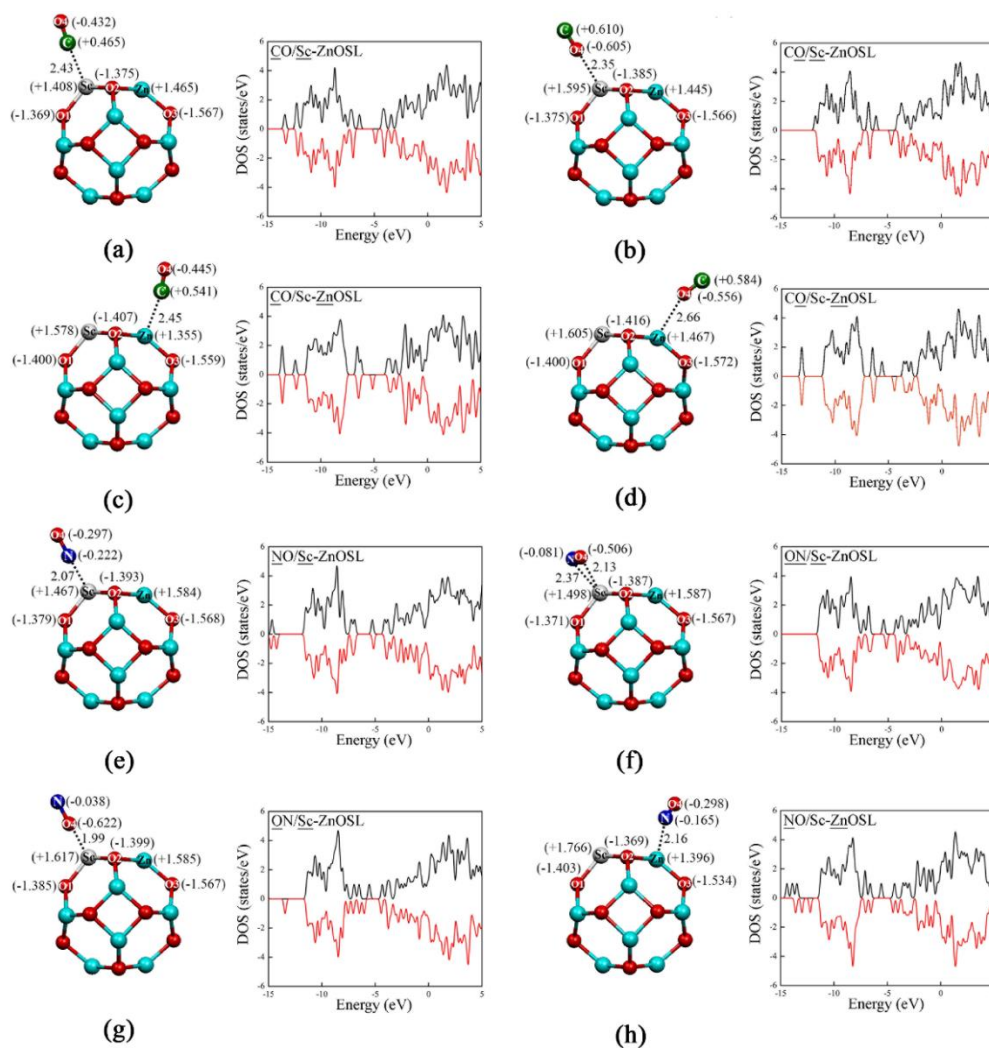
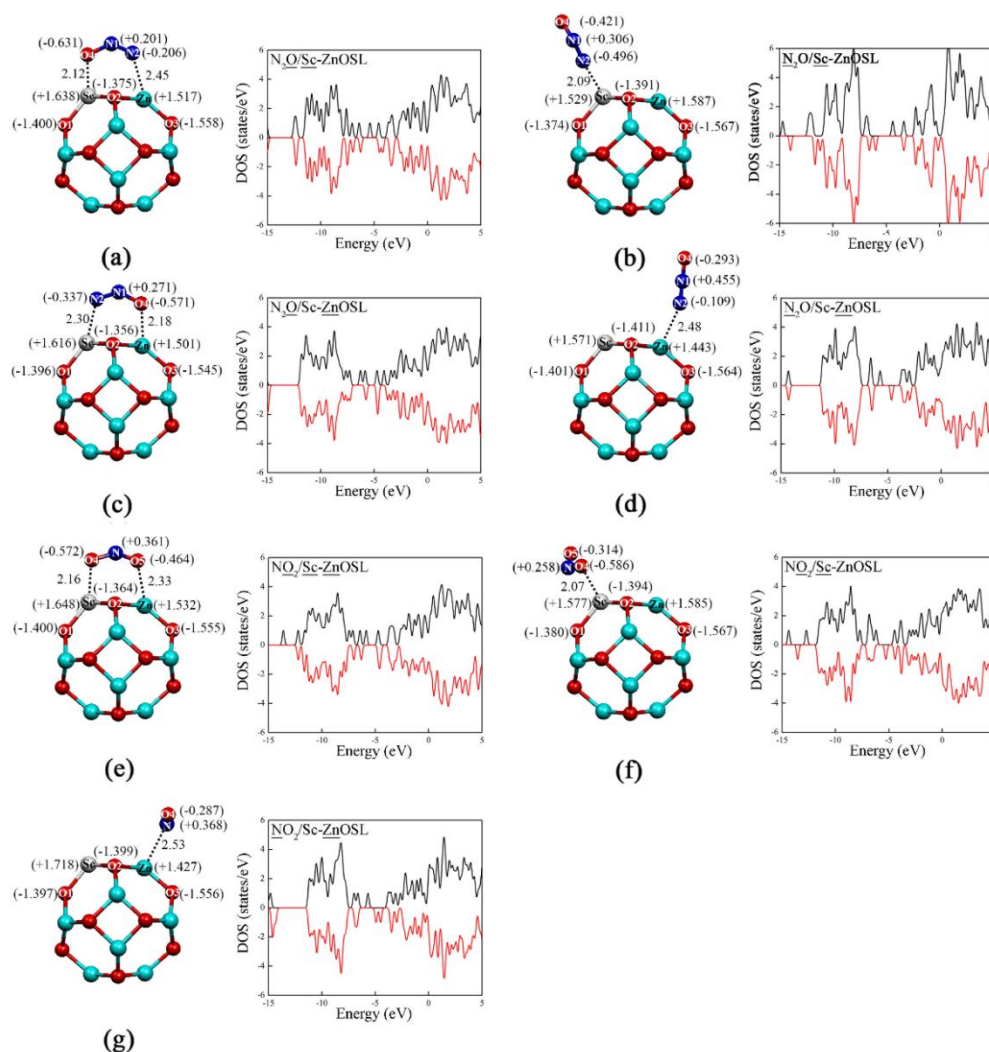


**Figure 5.2** The B3LYP/GEN-optimized structures of the Sc-doped ZnOSL adsorption with (a) CO (pointing C toward Sc), (b) CO (O toward Sc), (c) CO (C toward Zn), (d) CO (O toward Zn), (e) NO (N toward Sc), (f) NO (NO bond perpendicular to Sc), (g) NO (O toward Sc) and (h) NO (N toward Zn). Plots for their density of states are located beside their images. NBO atomic charges are in parentheses. Bond distances are in Å.



CHULALONGKORN UNIVERSITY

**Figure 5.3** The B3LYP/GEN-optimized structures of the Sc-doped ZnOSL adsorption with (a)  $\text{N}_2\text{O}$  (pointing O toward Sc and N toward Zn), (b)  $\text{N}_2\text{O}$  (N toward Sc), (c)  $\text{N}_2\text{O}$  (O toward Zn and N toward Sc), (d)  $\text{N}_2\text{O}$  (N toward Zn), (e)  $\text{NO}_2$  (O toward Sc and O' toward Zn), (f)  $\text{NO}_2$  (O toward Sc), (g)  $\text{NO}_2$  (N toward Zn). Plots for their density of states are located beside their images. NBO atomic charges are in parentheses. Bond distances are in Å.

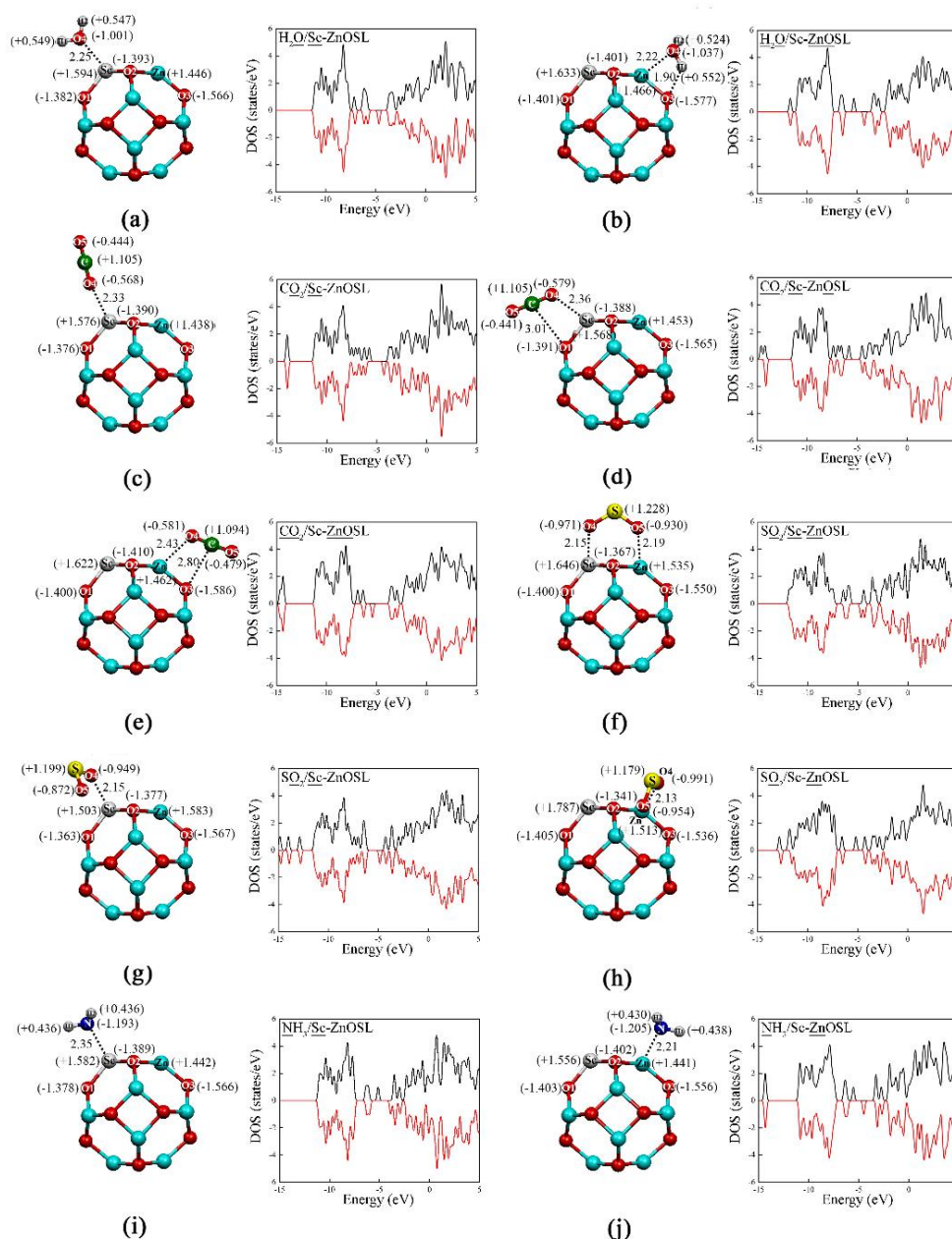


**Figure 5.4** The B3LYP/GEN-optimized structures of the Sc-doped ZnOSL adsorption with (a)  $\text{H}_2\text{O}$  (O toward Sc), (b)  $\text{H}_2\text{O}$  (O toward Zn), (c)  $\text{CO}_2$  (O toward Sc), (d)  $\text{CO}_2$  (C–O bond somewhat parallel to Sc–O bond, O toward Sc and C toward O), (e)  $\text{CO}_2$  (C–O bond somewhat parallel to Zn–O bond, O toward Zn and C toward O), (f)  $\text{SO}_2$  (O toward Sc and other O toward Zn), (g)  $\text{SO}_2$  (O toward Sc), (h)  $\text{SO}_2$  (O toward Zn), (i)  $\text{NH}_3$  (N toward Sc), (j)  $\text{NH}_3$  (N toward Zn). Plots for their density of states are located beside their images. NBO atomic charges are in parentheses. Bond distances are in Å.

**Table 5.1** The shortest bond–distances between gas atoms and adsorption atom of the Sc–doped ZnOSL.

Configuration	Bond <sup>a,b</sup>	Bond distance <sup>c</sup>	Configuration	Bond <sup>a,d</sup>	Bond distance <sup>c</sup>
<b>H<sub>2</sub>:</b>			<b>H<sub>2</sub>O:</b>		
H <sub>2</sub> /Sc–ZnOSL	H1…Sc	2.53	H <sub>2</sub> O/Sc–ZnOSL	O4…Sc	2.25
H <sub>2</sub> /Sc–ZnOSL	H1…O	2.44	H <sub>2</sub> O/Sc–ZnOSL	O4…Zn, H1…O	2.22, 1.90
<b>N<sub>2</sub>:</b>			<b>N<sub>2</sub>O:</b>		
N <sub>2</sub> /Sc–ZnOSL	N1…Sc	2.39	N <sub>2</sub> O/Sc–ZnOSL	O4…Sc, N2…Zn	2.12, 2.45
N <sub>2</sub> /Sc–ZnOSL	N1…Zn	2.64	N <sub>2</sub> O/Sc–ZnOSL	N2…Sc	2.09
<b>O<sub>2</sub>:</b>			<b>N<sub>2</sub>O/Sc–ZnOSL</b>		
O <sub>2</sub> /Sc–ZnOSL	O4…Sc	2.47	N <sub>2</sub> O/Sc–ZnOSL	O4…Zn, N2…Sc	2.18, 2.30
O <sub>2</sub> /Sc–ZnOSL	O4…Zn	2.80	N <sub>2</sub> O/Sc–ZnOSL	N2…Zn	2.48
<b>CO:</b>			<b>NO<sub>2</sub>:</b>		
CO/Sc–ZnOSL	C…Sc	2.43	NO <sub>2</sub> /Sc–ZnOSL	O4…Sc, O5…Zn	2.16, 2.33
OC/Sc–ZnOSL	O4…Sc	2.35	NO <sub>2</sub> /Sc–ZnOSL	O4…Sc	2.07
CO/Sc–ZnOSL	C…Zn	2.45	NO <sub>2</sub> /Sc–ZnOSL	N…Zn	2.53
OC/Sc–ZnOSL	O4…Zn	2.66	<b>CO<sub>2</sub>:</b>		
<b>NO:</b>			CO <sub>2</sub> /Sc–ZnOSL	O4…Sc	2.33
NO/Sc–ZnOSL	N…Sc	2.07	CO <sub>2</sub> /Sc–ZnOSL	O4…Sc, C…O1	2.36, 3.01
NO/Sc–ZnOSL	O4…Sc, N…Sc	2.13, 2.37	CO <sub>2</sub> /Sc–ZnOSL	O4…Zn, C…O3	2.43, 2.80
NO/Sc–ZnOSL	O4…Sc	1.99	<b>SO<sub>2</sub>:</b>		
NO/Sc–ZnOSL	N…Zn	2.16	SO <sub>2</sub> /Sc–ZnOSL <sup>e</sup>	O4…Sc, O5…Zn	2.15, 2.19
			SO <sub>2</sub> /Sc–ZnOSL	O4…Sc	2.15
			SO <sub>2</sub> /Sc–ZnOSL	O4…Zn	2.13
			<b>NH<sub>3</sub>:</b>		
			NH <sub>3</sub> /Sc–ZnOSL	N…Sc	2.35
			NH <sub>3</sub> /Sc–ZnOSL	N…Zn	2.21

<sup>a</sup> Bond distance (A…S) between atom A of gas and atom S of the Sc–ZnOSL surface.

<sup>b</sup> Atomic labels are defined in **Figure 5.1**.

<sup>c</sup> In Å.

<sup>d</sup> Atomic labels are defined in **Figure 5.3**.

<sup>e</sup> The strongest adsorption structure.

#### 5.4.2 Energetics and thermodynamics

Energy gaps, adsorption energies and thermodynamic quantities of gas adsorptions on Sc-doped ZnOSL are shown in **Table 5.2**. Based on adsorption energies, all homonuclear diatomic gases, H<sub>2</sub>, N<sub>2</sub>, and O<sub>2</sub> as pointing their atoms toward to Sc dopant atom of the Sc-doped ZnOSL were found to be strongest adsorptions. The adsorption strengths of homonuclear diatomic gases on the Sc-doped ZnOSL are in order: O<sub>2</sub> ( $\Delta E_{\text{ads}} = -40.65$ )  $\gg$  N<sub>2</sub> ( $\Delta E_{\text{ads}} = -6.79$ )  $>$  H<sub>2</sub> ( $\Delta E_{\text{ads}} = -0.19$  kcal/mol). Adsorption configurations with highest strengths of CO and NO on the Sc-doped ZnOSL are CO/Sc-ZnOSL and NO/Sc-ZnOSL of which C of CO and N of NO point toward Sc dopant atom in the Sc-doped ZnOSL, respectively. The adsorption strengths of heteronuclear diatomic gases on the Sc-doped ZnOSL are in order: NO ( $\Delta E_{\text{ads}} = -39.04$ )  $\gg$  CO ( $\Delta E_{\text{ads}} = -10.83$  kcal/mol).

Water adsorption on the Sc-ZnOSL, the adsorption configuration of H<sub>2</sub>O/Sc-ZnOSL was found to be most stable structure and its adsorption energy of  $-22.20$  kcal/mol. There are four configurations of adsorption structures of N<sub>2</sub>O on the Sc-ZnOSL and their stabilities are in order: N<sub>2</sub>O/Sc-ZnOSL ( $\Delta E_{\text{ads}} = -27.91$ )  $>$  N<sub>2</sub>O/Sc-ZnOSL ( $\Delta E_{\text{ads}} = -22.41$ )  $>$  N<sub>2</sub>O/Sc-ZnOSL ( $\Delta E_{\text{ads}} = -18.55$ )  $>$  N<sub>2</sub>O/Sc-ZnOSL ( $\Delta E_{\text{ads}} = -1.25$  kcal/mol). Three configurations (NO<sub>2</sub>/Sc-ZnOSL, NO<sub>2</sub>/Sc-ZnOSL and NO<sub>2</sub>/Sc-ZnOSL) of NO<sub>2</sub> adsorbed on the Sc-ZnOSL were obtained which adsorption energies of the second and third configurations are respectively  $-27.72$  and  $-27.41$  kcal/mol but the first one is unstable structure. All three adsorption configurations (CO<sub>2</sub>/Sc-ZnOSL, CO<sub>2</sub>/Sc-ZnOSL and CO<sub>2</sub>/Sc-ZnOSL) of CO<sub>2</sub> on the Sc-ZnOSL were found to be weak adsorption interactions. Three adsorption configurations (SO<sub>2</sub>/Sc-ZnOSL, SO<sub>2</sub>/Sc-ZnOSL and SO<sub>2</sub>/Sc-ZnOSL) of SO<sub>2</sub> on the Sc-ZnOSL are very stable of which adsorption energies are  $-63.57$ ,  $-57.30$  and  $-32.58$  kcal/mol, respectively. Two adsorption configurations (NH<sub>3</sub>/Sc-ZnOSL and NH<sub>3</sub>/Sc-ZnOSL) of NH<sub>3</sub> only one tetraatomic gas, on the Sc-ZnOSL were found that their adsorption energies are  $-26.91$  and  $-17.74$  kcal/mol, respectively.

Free energies of adsorptions of studied gases on the Sc–ZnOSL are shown in **Table 5.2** and the free energy profile of the Sc–doped ZnOSL and its adsorption structures with small gases is shown in **Figure 5.5**. It shows that SO<sub>2</sub> adsorbed on the Sc–ZnOSL is the most preferable spontaneous process and may suggest that the Sc–ZnOSL can be used as SO<sub>2</sub> storage material.

**Table 5.2** Energy gaps, adsorption energies and thermodynamic quantities of gas adsorptions on Sc–doped ZnOSL, computed at the B3LYP/GEN level of theory.

Configuration	$E_g^a$	$\Delta E_g^b$	$\Delta E_{ads}^c$	$\Delta H_{ads}^d$	$\Delta G_{ads}^d$	Configuration	$E_g^a$	$\Delta E_g^b$	$\Delta E_{ads}^c$	$\Delta H_{ads}^d$	$\Delta G_{ads}^d$
Sc–ZnOSL	1.19										
H <sub>2</sub> :						H <sub>2</sub> O:					
H <sub>2</sub> /Sc–ZnOSL	1.44	21.01	–0.19	–0.50	4.80	H <sub>2</sub> O/Sc–ZnOSL	1.33	11.76	–22.20	–22.31	–14.31
H <sub>2</sub> /Sc–ZnOSL	1.19	0.00	0.50	0.16	5.36	H <sub>2</sub> O/Sc–ZnOSL	1.09	–8.40	–13.64	–14.27	–4.57
N <sub>2</sub> :						N <sub>2</sub> O:					
N <sub>2</sub> /Sc–ZnOSL	0.56	–52.94	–6.79	–6.58	0.91	N <sub>2</sub> O/Sc–ZnOSL	2.16	81.51	–27.91	–27.79	–17.28
N <sub>2</sub> /Sc–ZnOSL	1.06	–10.92	–0.15	0.39	5.58	N <sub>2</sub> O/Sc–ZnOSL	1.03	–13.45	–18.55	–17.99	–9.97
O <sub>2</sub> :						N <sub>2</sub> O/Sc–ZnOSL	1.92	61.34	–22.41	–22.41	–11.42
O <sub>2</sub> /Sc–ZnOSL	1.52	27.73	–40.65	–40.67	–33.39	N <sub>2</sub> O/Sc–ZnOSL	1.05	–11.76	–1.25	–1.23	7.65
O <sub>2</sub> /Sc–ZnOSL	1.13	–5.04	–37.97	–37.87	–31.76	NO <sub>2</sub> :					
CO:						NO <sub>2</sub> /Sc–ZnOSL	1.12	–5.88	0.035	0.720	8.239
CO/Sc–ZnOSL	0.62	–47.90	–10.83	–10.73	–2.33	NO <sub>2</sub> /Sc–ZnOSL	0.79	–33.61	–27.72	–27.37	–17.72
CO/Sc–ZnOSL	0.51	–57.14	–5.60	–5.30	2.51	NO <sub>2</sub> /Sc–ZnOSL	0.61	–48.74	–27.41	–27.42	–15.67
CO/Sc–ZnOSL	0.94	–21.01	–3.38	–3.09	4.40	CO <sub>2</sub> :					
CO/Sc–ZnOSL	1.11	–6.72	–0.11	0.49	6.04	CO <sub>2</sub> /Sc–ZnOSL	1.41	18.49	–8.97	–8.47	–1.67
NO:						CO <sub>2</sub> /Sc–ZnOSL	1.53	28.57	–8.17	–7.78	–0.04
NO/Sc–ZnOSL	0.97	–18.49	–39.04	–39.04	–29.64	CO <sub>2</sub> /Sc–ZnOSL	1.12	–5.88	–3.40	–2.95	4.79
NO/Sc–ZnOSL	1.08	–9.24	–34.71	–34.62	–25.53	SO <sub>2</sub> :					
NO/Sc–ZnOSL	0.91	–23.53	–34.87	–34.72	–26.11	SO <sub>2</sub> /Sc–ZnOSL	1.95	63.87	–63.57	–63.47	–51.57
NO/Sc–ZnOSL	0.68	–42.86	–14.72	–14.58	–5.65	SO <sub>2</sub> /Sc–ZnOSL	1.67	40.34	–57.30	–56.93	–46.71
						SO <sub>2</sub> /Sc–ZnOSL	1.13	–5.04	–32.58	–32.36	–20.95
						NH <sub>3</sub> :					
						NH <sub>3</sub> /Sc–ZnOSL	1.47	23.53	–26.91	–27.12	–19.24
						NH <sub>3</sub> /Sc–ZnOSL	1.01	–15.13	–17.74	–18.03	–9.33

<sup>a</sup> In eV.

<sup>b</sup> Percentage of energy–gap change compared with clean Sc–ZnOSL.

<sup>c</sup> Based on zero–point energy correction, in kcal/mol.

<sup>d</sup> At 298.15 K, in kcal/mol.

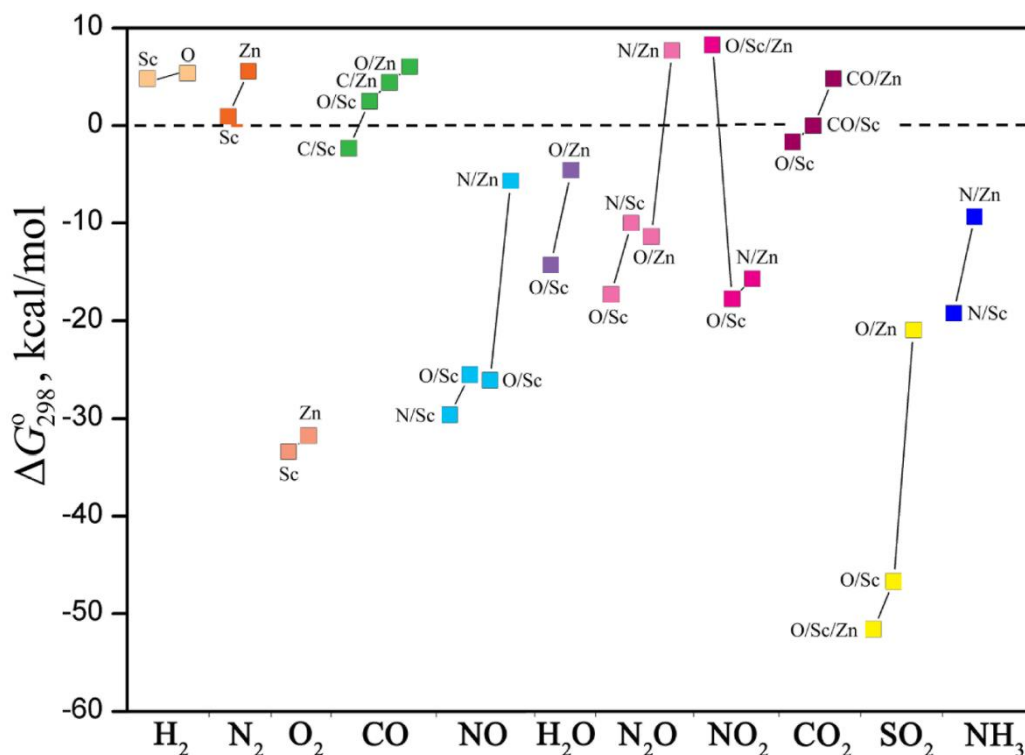


**Figure 5.5** Free energy profile of adsorptions of small gas over the Sc-doped ZnOSL. Short symbols indicate atomic site(s) of the Sc-doped ZnOSL of which full notations are defined in **Table 5.1**.

#### 5.4.3 Density of state and gap energy

Density of states (DOSs) of the B3LYP/GEN-optimized structures of Sc-doped ZnOSL and their adsorption structures with H<sub>2</sub>, N<sub>2</sub> and O<sub>2</sub> (**Figure 5.1**), CO and NO (**Figure 5.2**), N<sub>2</sub>O and NO<sub>2</sub> (**Figure 5.3**), H<sub>2</sub>O, CO<sub>2</sub>, SO<sub>2</sub>, NH<sub>3</sub> (**Figure 5.4**) were obtained. The energy gaps of all adsorption structures and their changes ( $E_g$ ) with respect to clean Sc-ZnOSL are shown in **Table 5.2**. Plot of changes in energy gaps of the Sc-ZnOSL during gas adsorptions, illustrated in **Figure 5.6**, shows that N<sub>2</sub>O gives highest positive change in energy gap (81.51%) on the Sc-ZnOSL. The second highest positive change in energy gap (63.87%) of the N<sub>2</sub>O adsorbed on the Sc-

ZnOSL was found. It may suggest that the Sc–ZnOSL can be working as  $\text{N}_2\text{O}$  or  $\text{SO}_2$  detecting material by measurement in change of its resistance.

Other way around,  $\text{N}_2$ ,  $\text{CO}$ ,  $\text{NO}$  and  $\text{NO}_2$  are candidates to give competitively high negative changes in energy gap on the Sc–ZnOSL and magnitudes of electric conductance due to these four gases adsorbed on the Sc–ZnOSL are in order:  $\text{CO}$  ( $-57.14\%$ )  $>$   $\text{N}_2$  ( $-52.94\%$ )  $>$   $\text{NO}_2$  ( $-48.74\%$ )  $>$   $\text{NO}$  ( $-42.86\%$ ). The Sc–ZnOSL is hardly ever used to significantly detect these gases in their mixtures.

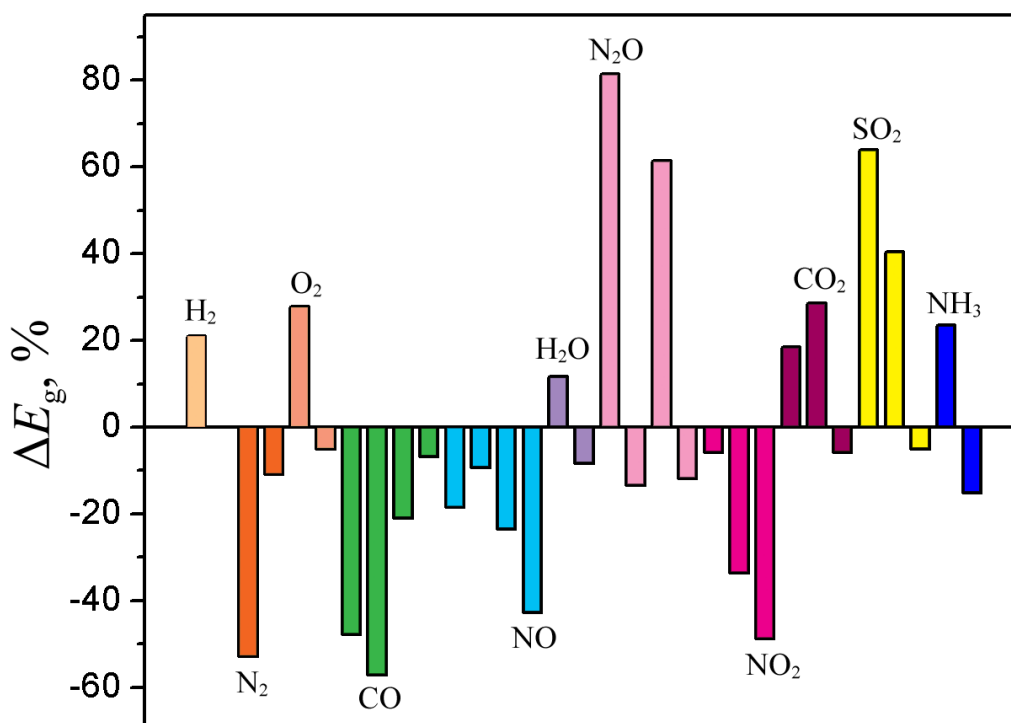


**Figure 5.6** Changes in energy gaps (in %) of the Sc–doped ZnOSL while each gas is adsorbed. Adsorption sequences correspond to data tabulated in **Table 5.2**.

#### 5.4.4 NBO atomic charges

NBO atomic charges of the B3LYP/GEN-optimized structures of the Sc-ZnOSL and their adsorption structures with H<sub>2</sub>, N<sub>2</sub> and O<sub>2</sub> (**Figure 5.1**), CO and NO (**Figure 5.2**), N<sub>2</sub>O and NO<sub>2</sub> (**Figure 5.3**), H<sub>2</sub>O, CO<sub>2</sub>, SO<sub>2</sub>, NH<sub>3</sub> (**Figure 5.4**) were obtained. NBO charges of gases atoms, atoms nearby adsorption area of the Sc-ZnOSL and partial charge transfer (PCT) of Sc and neighboring Zn atom are shown in **Table 5.3** and **Table 5.4**. As PCTs of both Sc and neighboring Zn of the Sc-ZnOSL adsorbed by N<sub>2</sub>O and SO<sub>2</sub> result high positive values which are respectively (Sc = 0.028e, Zn = 0.066e) and (Sc = 0.038e, Zn = 0.084e), their adsorption structures can be reasonably described as ON<sub>2</sub>/Sc-ZnOSL ( $\Delta E_{\text{ads}} = -27.94$  kcal/mol) and SO<sub>2</sub>/Sc-ZnOSL ( $\Delta E_{\text{ads}} = -63.57$  kcal/mol), respectively. All partial charges of Sc dopant in the Sc-ZnOSL are regularly larger than neighboring Zn atom.

**Table 5.3** NBO charges of diatomic gases atoms, atoms nearby adsorption area of the Sc-doped ZnOSL and partial charge transfer (PCT) of Sc and neighboring Zn atom, computed at the B3LYP/GEN level of theory.

Configuration	NBO partial charge <sup>a</sup>					Gas <sup>b</sup>			PCT <sup>c</sup>	
	O <sub>1</sub>	Sc	O <sub>2</sub>	Zn	O <sub>3</sub>	Atom #1	Atom #2	Atom #3	Sc	Zn
Sc-ZnOSL	-1.401	1.610	-1.412	1.451	-1.567	-	-	-	-	-
<b>H<sub>2</sub>:</b>						<b>H1</b>	<b>H2</b>			
H <sub>2</sub> /Sc-ZnOSL	-1.376	1.562	-1.388	1.444	-1.566	0.040	0.019	-	<b>-0.048</b>	-0.007
H <sub>2</sub> /Sc-ZnOSL	-1.401	1.611	-1.415	1.461	-1.571	0.003	-0.001	-	0.001	<b>0.010</b>
H <sub>2</sub> /Sc-ZnOSL	-1.400	1.612	-1.415	1.461	-1.582	0.029	-0.033	-	0.002	<b>0.010</b>
<b>N<sub>2</sub>:</b>						<b>N1</b>	<b>N2</b>			
N <sub>2</sub> /Sc-ZnOSL	-1.372	1.535	-1.380	1.450	-1.566	-0.095	0.090	-	<b>-0.075</b>	-0.001
N <sub>2</sub> /Sc-ZnOSL	-1.399	1.593	-1.415	1.444	-1.570	-0.019	-0.075	-	-0.017	<b>-0.007</b>
<b>O<sub>2</sub>:</b>						<b>O4</b>	<b>O5</b>			
O <sub>2</sub> /Sc-ZnOSL	-1.375	1.547	-1.385	1.440	-1.565	-0.020	0.123	-	<b>-0.063</b>	-0.011
O <sub>2</sub> /Sc-ZnOSL	-1.400	1.607	-1.415	1.454	-1.571	-0.021	0.052	-	-0.003	<b>0.003</b>
<b>CO:</b>						<b>C</b>	<b>O4</b>			
CO/Sc-ZnOSL	-1.369	1.408	-1.375	1.465	-1.567	0.465	-0.432	-	<b>-0.202</b>	0.014
QC/Sc-ZnOSL	-1.375	1.595	-1.385	1.445	-1.566	0.610	-0.605	-	<b>-0.015</b>	-0.006
CO/Sc-ZnOSL	-1.400	1.578	-1.407	1.355	-1.559	0.541	-0.445	-	-0.032	<b>-0.096</b>
QC/Sc-ZnOSL	-1.400	1.605	-1.416	1.467	-1.572	0.584	-0.556	-	-0.005	<b>0.016</b>
<b>NO</b>						<b>N</b>	<b>O4</b>			
NO/Sc-ZnOSL	-1.379	1.467	-1.393	1.584	-1.568	-0.022	-0.297	-	<b>-0.143</b>	0.133
QN/Sc-ZnOSL	-1.371	1.498	-1.387	1.587	-1.567	-0.081	-0.506	-	<b>-0.112</b>	0.136
QN/Sc-ZnOSL	-1.385	1.617	-1.399	1.585	-1.567	-0.038	-0.622	-	0.007	<b>0.134</b>
NO/Sc-ZnOSL	-1.403	1.766	-1.369	1.396	-1.534	-0.165	-0.298	-	0.156	<b>-0.055</b>

<sup>a</sup> In e.

<sup>b</sup> Atoms in gas, in e.

<sup>c</sup> Partial charge transfer, defined as a difference of between adsorption-site metal atom of adsorption and non-adsorption states, in e.

**Table 5.4** NBO charges of polyatomicgases atoms, atoms nearby adsorption area of the Sc-doped ZnOSL and partial charge transfer (PCT) of Sc and neighboring Zn atom, computed at the B3LYP/GEN level of theory.

Configuration	NBO partial charge <sup>a</sup>					Gas <sup>b</sup>			PCT <sup>c</sup>	
	O <sub>1</sub>	Sc	O <sub>2</sub>	Zn	O <sub>3</sub>	Atom #1	Atom #2	Atom #3	Sc	Zn
Sc-ZnOSL	-1.401	1.610	-1.412	1.451	-1.567	-	-	-	-	-
<b>H<sub>2</sub>O:</b>						<b>O4</b>	<b>H1</b>	<b>H2</b>		
H <sub>2</sub> O/Sc-ZnOSL	-1.382	1.594	-1.393	1.446	-1.566	-1.001	0.549	0.547	<b>-0.016</b>	-0.005
<u>H<sub>2</sub>O/Sc-ZnOSL</u>	-1.401	1.633	-1.401	1.466	-1.577	-1.037	0.552	0.524	0.023	<b>0.015</b>
<b>N<sub>2</sub>O:</b>						<b>N2</b>	<b>N1</b>	<b>O4</b>		
<u>ON<sub>2</sub>/Sc-ZnOSL</u>	-1.400	1.638	-1.375	1.517	-1.558	-0.206	0.201	-0.631	<b>0.028</b>	0.066
<u>N<sub>2</sub>O/Sc-ZnOSL</u>	-1.374	1.529	-1.391	1.587	-1.567	-0.496	0.306	-0.421	<b>-0.081</b>	0.136
<u>ON<sub>2</sub>/Sc-ZnOSL</u>	-1.396	1.616	-1.356	1.501	-1.545	-0.337	0.271	-0.571	0.006	<b>0.050</b>
<u>N<sub>2</sub>O/Sc-ZnOSL</u>	-1.401	1.571	-1.411	1.443	-1.564	-0.109	0.455	-0.293	-0.039	<b>-0.008</b>
<b>NO<sub>2</sub>:</b>						<b>O4</b>	<b>N</b>	<b>O5</b>		
<u>NO<sub>2</sub>/Sc-ZnOSL</u>	-1.400	1.648	-1.364	1.532	-1.555	-0.572	0.361	-0.464	<b>0.038</b>	<b>0.081</b>
<u>NO<sub>2</sub>/Sc-ZnOSL</u>	-1.380	1.577	-1.394	1.585	-1.567	-0.586	0.258	-0.314	<b>-0.033</b>	0.134
<u>NO<sub>2</sub>/Sc-ZnOSL</u>	-1.397	1.718	-1.399	1.427	-1.556	-0.287	0.368	-0.287	0.108	<b>-0.024</b>
<b>CO<sub>2</sub>:</b>						<b>O4</b>	<b>C</b>	<b>O5</b>		
<u>CO<sub>2</sub>/Sc-ZnOSL</u>	-1.376	1.576	-1.390	1.438	-1.566	-0.568	1.105	-0.444	<b>-0.034</b>	-0.013
<u>CO<sub>2</sub>/Sc-ZnOSL</u>	-1.391	1.568	-1.388	1.453	-1.565	-0.579	1.105	-0.441	<b>-0.042</b>	0.002
<u>CO<sub>2</sub>/Sc-ZnOSL</u>	-1.400	1.622	-1.410	1.462	-1.586	-0.581	1.094	-0.479	0.012	<b>0.011</b>
<b>SO<sub>2</sub>:</b>						<b>O4</b>	<b>S</b>	<b>O5</b>		
<u>SO<sub>2</sub>/Sc-ZnOSL</u>	-1.400	1.646	-1.367	1.535	-1.550	-0.971	1.228	0.930	<b>0.036</b>	<b>0.084</b>
<u>SO<sub>2</sub>/Sc-ZnOSL</u>	-1.363	1.503	-1.377	1.583	-1.567	-0.949	1.199	-0.872	<b>-0.107</b>	0.132
<u>SO<sub>2</sub>/Sc-ZnOSL</u>	-1.405	1.787	-1.341	1.513	-1.536	-0.991	1.179	-0.954	0.177	<b>0.062</b>
<b>NH<sub>3</sub>:</b>						<b>N</b>	<b>H1</b>	<b>H2</b>		
<u>NH<sub>3</sub>/Sc-ZnOSL</u>	-1.378	1.582	-1.389	1.442	-1.566	-1.193	0.436	0.436	<b>-0.028</b>	-0.009
<u>NH<sub>3</sub>/Sc-ZnOSL</u>	-1.403	1.556	-1.402	1.441	-1.556	-1.205	0.438	0.430	-0.054	<b>-0.010</b>

<sup>a</sup> In e.

<sup>b</sup> Atoms in gas, in e.

<sup>c</sup> Partial charge transfer, defined as a difference of between adsorption-site metal atom of adsorption and non-adsorption states, in e.

## 5.5 CONCLUSION

Adsorption of diatomic ( $\text{H}_2$ ,  $\text{N}_2$ ,  $\text{O}_2$ ,  $\text{CO}$  and  $\text{NO}$ ), triatomic ( $\text{N}_2\text{O}$ ,  $\text{NO}_2$ ,  $\text{H}_2\text{O}$ ,  $\text{CO}_2$ , and  $\text{SO}_2$ ) and polyatomic ( $\text{NH}_3$ ) gases on Sc–ZnOSL was studied using the B3LYP/GEN method. Energies, enthalpies and Gibbs free energies of gas adsorptions were obtained. Adsorption strengths of diatomic gases on the Sc–ZnOSL are in order:  $\text{O}_2$  ( $\Delta E_{\text{ads}} = -40.65$ ) >  $\text{NO}$  ( $\Delta E_{\text{ads}} = -39.04$ ) >>  $\text{CO}$  ( $\Delta E_{\text{ads}} = -10.83$ ) >>  $\text{N}_2$  ( $\Delta E_{\text{ads}} = -6.79$ ) >  $\text{H}_2$  ( $\Delta E_{\text{ads}} = -0.19$  kcal/mol). Adsorption strengths of tri- and tetraatomic gases the Sc–ZnOSL (the most stable configurations) are in order:  $\text{SO}_2/\text{Sc-ZnOSL}$  ( $\Delta E_{\text{ads}} = -63.57$ ) >  $\text{N}_2\text{O}/\text{Sc-ZnOSL}$  ( $\Delta E_{\text{ads}} = -27.91$ )  $\approx$   $\text{NO}_2/\text{Sc-ZnOSL}$  ( $\Delta E_{\text{ads}} = -27.72$ ) >  $\text{NH}_3/\text{Sc-ZnOSL}$  ( $\Delta E_{\text{ads}} = -26.91$  kcal/mol). It can be concluded that  $\text{SO}_2$  adsorbed on the Sc–ZnOSL is the most energetically preferred configuration and the Sc–ZnOSL can be used as  $\text{SO}_2$  storage material. It may suggest that the Sc–ZnOSL can be working as  $\text{N}_2\text{O}$  or  $\text{SO}_2$  detecting material by measurement in change of its resistance.

## 5.6 SUPPLEMENTARY DATA

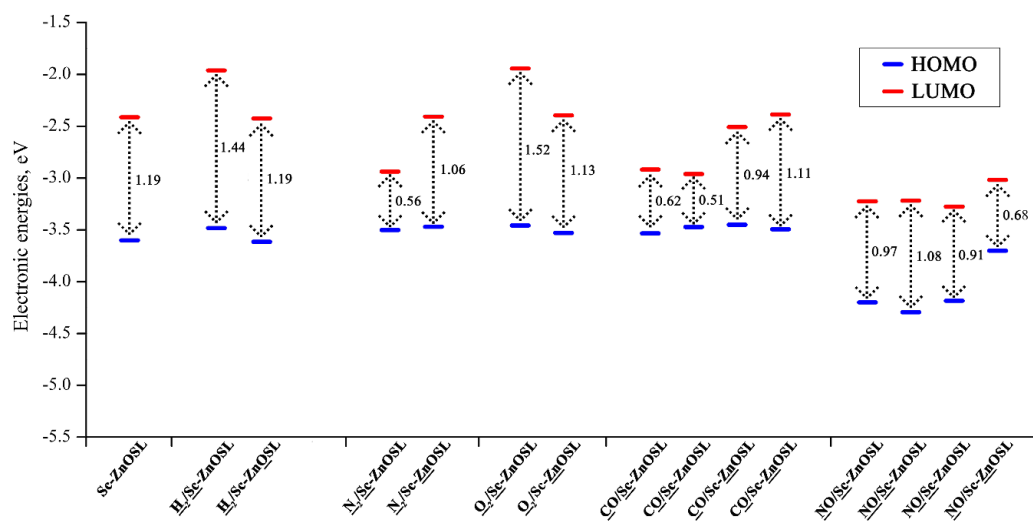


**Figure S5.1** Plot of frontier orbitals' energies against adsorption structures of Sc-doped ZnOSL with di-atomic gases. HOMO-LUMO gaps are compared with the clean Sc-doped ZnOSL.

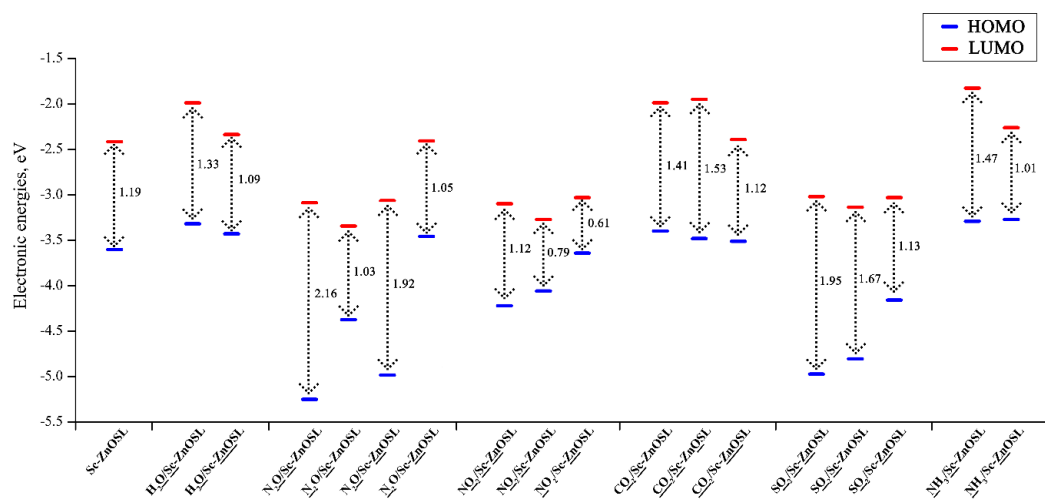


**Figure S5.2** Plot of frontier orbitals' energies against adsorption structures of Sc-doped ZnOSL with tri- and tetra gases. HOMO–LUMO gaps are compared with the clean Sc-doped ZnOSL.

# CHAPTER VI

## MECHANISM OF CO CONVERSION TO CO<sub>2</sub> OVER THE Mn-DOPED TiO<sub>2</sub> (001) SURFACE UNDER O<sub>2</sub> ATMOSPHERE

Waranyu Pipornpong, Vithaya Ruangpornvisuti

This article has been submitted

### 6.1 ABSTRACT

Mechanisms of CO oxidation by O<sub>2</sub> over the Mn-doped TiO<sub>2</sub> (001) surface to afford CO<sub>2</sub> was investigated using periodic DFT method. Two similar mechanisms of different structures of oxygen pre-adsorbed on the Mn-doped TiO<sub>2</sub> surface were found that are energetically preferred reactions. The both mechanisms were found to consist of five reaction steps of which overall reaction,  $2\text{CO} + \text{O}_2 \rightarrow 2\text{CO}_2$  and reaction energies (-199.69 kcal/mol) are obtained.

### 6.2 INTRODUCTION

There are many types of CO conversion catalysts such as precious metal particles or their supported on metal oxide [142-146]. Many researchers focus on the efficiency of metal oxide such as MnO<sub>2</sub> [147, 148], CuO [149] and ZnO [150], due to its ability to exchange lattice oxygen with the gas phase. One of the most thermally stable metal oxides is TiO<sub>2</sub>. Two main polymorphs of TiO<sub>2</sub>, rutile and anatase, have been studied in experimental and theoretical researches as CO conversion catalyst [151-154]. The high adsorption reactivity and high catalytic efficiency of anatase (001) are influenced by its higher surface area and density of surface [20, 155, 156]. Furthermore, atoms of Ti<sub>5c</sub> on the (001) surface are able to enhance the catalytic reactivity in heterogeneous reactions [157, 158].

Anatase (001) has been extensively improved by doping with transition metal (M–TiO<sub>2</sub>). The results of doping enhance the catalytic performance of anatase in the conversion reactions [19, 159, 160]. In our previous works, we found that conversion of CO to CO<sub>2</sub> occurred on oxygen vacancy defect of anatase surface [152, 153]. The dopants were selected based on the findings of McFarland's study [19]. The cation dopant with ionic radius and electronegativity close to those of Ti<sup>4+</sup> cation is the most suitable dopant owing to less distortion inside TiO<sub>2</sub>. This explanation demonstrated that Mn doping (Mn–TiO<sub>2</sub>) is particularly outstanding attributed to the resemblance in charge and radii of Ti and Mn ions [161-163]. Furthermore, the Mn–TiO<sub>2</sub> catalyst was also prepared by many techniques such as hydrothermal treatment [164], solvothermal synthesis [165] and sol–gel method [166]. A series of Mn/TiO<sub>2</sub> catalysts were prepared and investigated for the catalytic CO oxidation reaction and found to exhibit the best catalytic activity for CO oxidation [167]. In the present work, the CO oxidation with O<sub>2</sub> on Mn–TiO<sub>2</sub> to yield CO<sub>2</sub> has, therefore, been investigated using periodic DFT method. Mechanism depending on adsorption configurations of Mn–TiO<sub>2</sub> (001) surface with CO, O<sub>2</sub> and CO<sub>2</sub> for CO oxidation to CO<sub>2</sub> has been resolved.

### 6.3 COMPUTATIONAL DETAILS

The crystal model was extracted from an experimental bulk of anatase structure [168]. All DFT calculations were performed and investigated using CRYSTAL06 computational code [168] based on DFT/PBE. The basis sets, the Hay–Wadt “small–core” ECPs with the 411(311d)G level of contraction [169] and the triple–zeta valence with polarization quality (TZVP) [170] have been respectively employed for the titanium and oxygen on the TiO<sub>2</sub> (001) surface. Charges of Ti and O were set as Ti<sup>4+</sup>, and O<sup>2-</sup>, respectively. Broyden's convergence accelerator tool for geometry optimization convergence was used. The convergence threshold for energy change between optimization steps was set as default at 10<sup>-6</sup> a.u. Consequently, anatase (001) clean surface was created with nine layers from slab cut (~5.64 Å of

thickness) as shown in **Figure 6.1(a)**. To perform Mn–TiO<sub>2</sub> surface, one Ti atom on the anatase (001) surface was substituted by one Mn atom. The Hay–Wadt “small–core” ECPs with the 411(311d)G level of contraction basis set [89] was set for Mn atom. Since Mn<sup>4+</sup> was the key role of catalysis process [19, 163, 164, 171], only top three layers were allowed to relax whereas the bottom six layers were constrained at the bulk position in optimization process.

## 6.4 RESULTS AND DISCUSSION

### 6.4.1 Bulk structure of anatase TiO<sub>2</sub>

The lattice structure of anatase TiO<sub>2</sub> belongs to 141/amd space group and consists of Ti<sub>6c</sub>, O<sub>2c</sub>, and O<sub>3c</sub> in TiO<sub>2</sub> bulk. The O<sub>2c</sub> is called bridging oxygen. With full optimization performing with 8×8×8 shrinking factors, optimized coordinates in the anatase conventional cell of Ti and O were (0, 0, 0) and (0, 0, 2.06562), respectively. The optimized lattice parameters of the bulk anatase TiO<sub>2</sub>,  $a = b = 3.77596 \text{ \AA}$ ,  $c = 9.58085 \text{ \AA}$ , and  $\alpha = \beta = \gamma = 90^\circ$  were obtained.

### 6.4.2 The TiO<sub>2</sub> (001) and Mn–doped surfaces

The anatase TiO<sub>2</sub> (001) surface represent a large portion of the surface of polycrystalline TiO<sub>2</sub> which was utilized as it is the lowest energy surface of anatase TiO<sub>2</sub>, therefore (001) surface was widely investigated [172, 173]. The optimized–structure of anatase TiO<sub>2</sub>(001) surface modeled by (2×3) slab of nine layers, containing altogether 18 Ti and 36 O atoms are shown in **Figure 6.1(a)**. It shows Ti<sub>5c</sub> and O<sub>2c</sub> on slab cut layer.

The Mn-doped anatase TiO<sub>2</sub> (001) surface represented by doping Mn into the titanium-vacancy (V<sub>Ti</sub>) on the TiO<sub>2</sub>(001) surface (denoted by [TiO<sub>2</sub>+V<sub>Ti</sub>]) can be presented as following reaction equations.



After doping Mn on the TiO<sub>2</sub>(001) surface, the structure of Mn-TiO<sub>2</sub> anatase TiO<sub>2</sub> (001) surface was re-optimized by relaxing the three upper layers of slab surface. The optimized-structure Mn-doped TiO<sub>2</sub> (001) surface is shown in **Figure 6.1(b)**. It was found that Ti<sup>4+</sup> of the topmost (001) layer was easily replaced with Mn<sup>4+</sup> as depicted in **Figure 6.1(b)**. Investigation results showed that the atomic positions of re-optimized Mn-TiO<sub>2</sub> surface was closely to un-doped TiO<sub>2</sub> (001) surface. The binding energy ( $\Delta E_{\text{binding}}$ ) for Mn bound to [TiO<sub>2</sub>+V<sub>Ti</sub>],  $E(\text{Mn-TiO}_2) - \{E[\text{TiO}_2+\text{V}_{\text{Ti}}]+E(\text{Mn}^{4+})\}$ , of -750.28 kcal/mol was obtained.



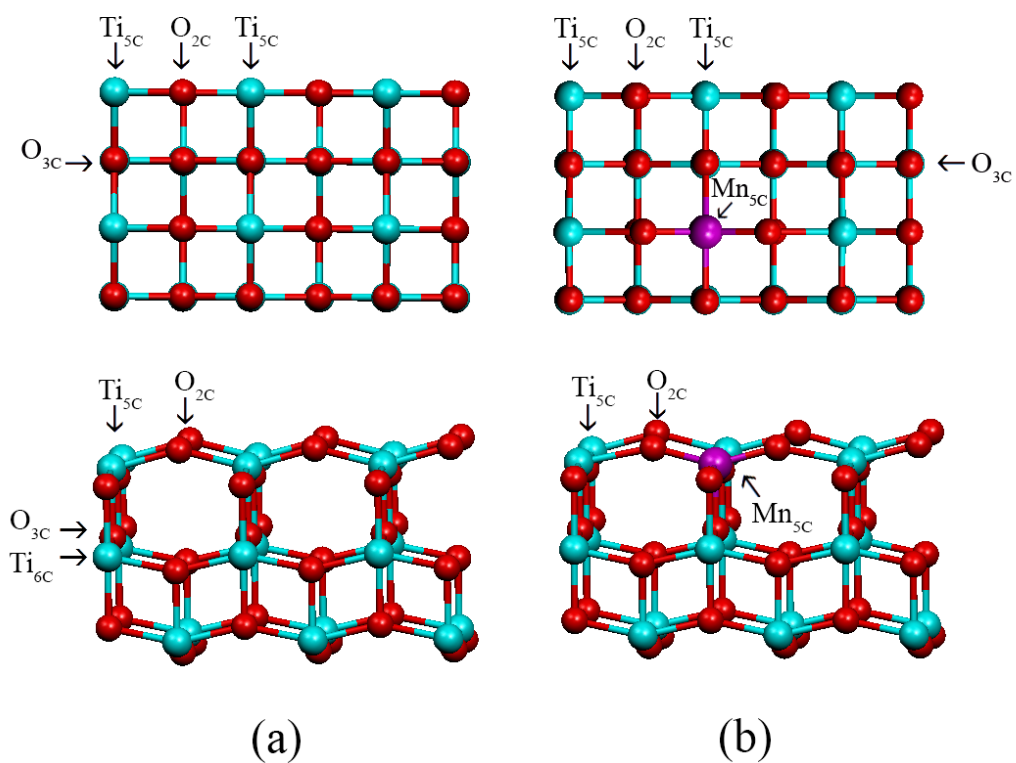


**Figure 6.1** The optimized-structures of (a) un-doped and (b) Mn-doped anatase  $\text{TiO}_2$  (001) surfaces modeled by  $(2 \times 3)$  slab of nine layers, containing altogether 18 Ti and 36 O atoms. Top and side views are shown at the top and bottom images, respectively.

### 6.4.3 Adsorption of adsorbate gases on the Mn-doped TiO<sub>2</sub> surface

#### 6.4.3.1 Adsorption of oxygen on the Mn-doped TiO<sub>2</sub> surface

Two optimized adsorption structures of oxygen molecule adsorbed on the Mn-doped TiO<sub>2</sub> surface were found. There are two configurations of O<sub>2</sub> adsorbed on the Mn-doped TiO<sub>2</sub> surface, one is the V-shape configuration (denoted by O<sub>2</sub><sup>V</sup>/Mn-TiO<sub>2</sub>) and the other is the I-shape configuration (denoted by O<sub>2</sub><sup>I</sup>/Mn-TiO<sub>2</sub>), as shown in **Figure 6.2**. The V-shape configuration (O<sub>2</sub><sup>V</sup>/Mn-TiO<sub>2</sub>) was found to be more stable than the I-shape configuration (O<sub>2</sub><sup>I</sup>/Mn-TiO<sub>2</sub>) by 18.35 kcal/mol. Accordingly, adsorption strengths of two configurations of O<sub>2</sub> adsorbed on the Mn-TiO<sub>2</sub> are in order: O<sub>2</sub><sup>V</sup>/Mn-TiO<sub>2</sub> ( $\Delta E_{\text{ads}} = -102.35$  kcal/mol) > O<sub>2</sub><sup>I</sup>/Mn-TiO<sub>2</sub> ( $\Delta E_{\text{ads}} = -84.00$  kcal/mol) of which adsorption strengths are larger than the O<sub>2</sub> adsorbed on the undoped TiO<sub>2</sub> ( $\Delta E_{\text{ads}} = -68.13$  kcal/mol), see **Table 6.2**. Only one conformation of CO gas adsorbed on the Mn-TiO<sub>2</sub> ( $\Delta E_{\text{ads}} = -66.08$  kcal/mol) was found and the adsorption strengths is much less than the adsorption of O<sub>2</sub><sup>V</sup>/Mn-TiO<sub>2</sub> and O<sub>2</sub><sup>I</sup>/Mn-TiO<sub>2</sub> as shown in **Table 6.2**. For adsorption strengths of oxygen atom on un- and the Mn-doped TiO<sub>2</sub> are in order: O/Mn-TiO<sub>2</sub> ( $\Delta E_{\text{ads}} = -216.50$  kcal/mol) > O/TiO<sub>2</sub> ( $\Delta E_{\text{ads}} = -187.70$  kcal/mol).

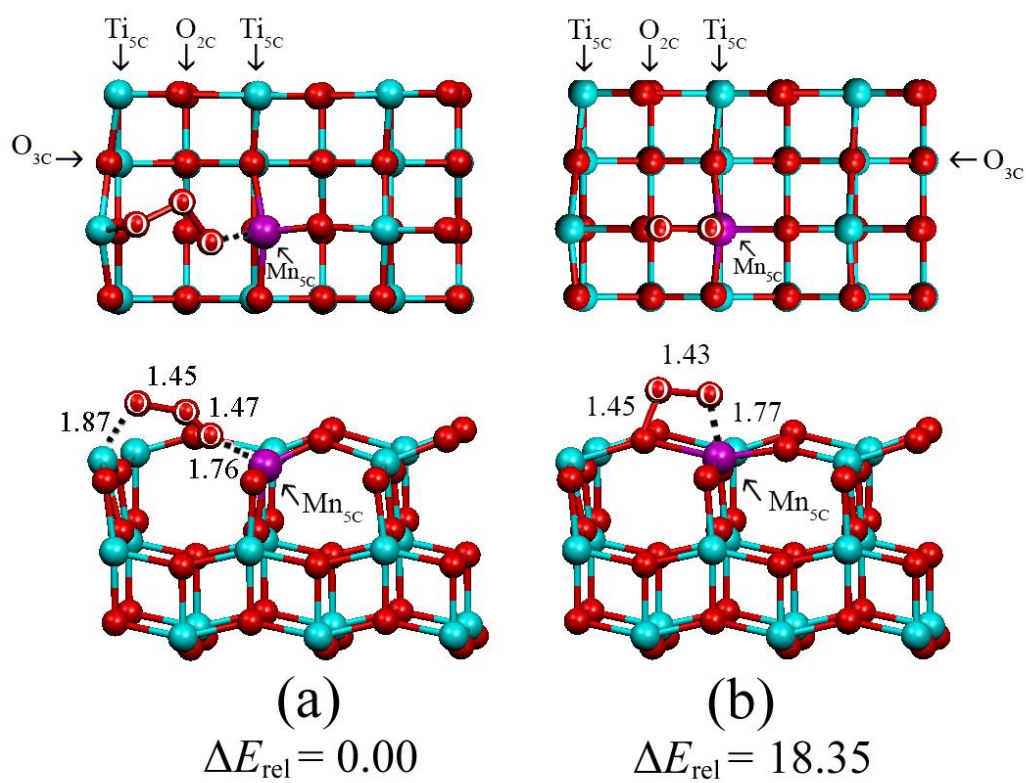


**Figure 6.2** The adsorption structures of  $\text{O}_2$  on Mn-doped  $\text{TiO}_2$  surface as (a) V-shape configuration ( $\text{O}_2^{\text{V}}/\text{Mn-TiO}_2$ ) and (b) I-shape configuration ( $\text{O}_2^{\text{I}}/\text{Mn-TiO}_2$ ). Their relative energies ( $\Delta E_{\text{rel}}$ ) are in kcal/mol and bond distances are in Å. Top and side views are shown at the top and bottom images, respectively.

**Table 6.1** Lattice parameters of the anatase TiO<sub>2</sub> crystals based (I41/amd space group), compared with other computed and observed results.

Methods	Lattice parameters <sup>a</sup>	
	<i>a</i>	<i>c</i>
DFT/PBE	3.776	9.581
DFT+U <sup>b</sup>	3.806	9.679
DFT/PBE <sup>c</sup>	3.794	9.515
DFT/B3LYP <sup>d</sup>	3.736	9.981
Exp. <sup>e</sup>	3.785	9.513
Exp. <sup>f</sup>	3.785	9.514
Exp. Mn–TiO <sub>2</sub> <sup>f</sup>	3.785	9.304
Exp. <sup>g</sup>	3.786	9.504
Exp. Mn–TiO <sub>2</sub> (0.02 wt% Mn) <sup>g</sup>	3.784	9.492
Exp. Mn–TiO <sub>2</sub> (0.04 wt% Mn) <sup>g</sup>	3.804	9.468
Exp. Mn–TiO <sub>2</sub> (0.06 wt% Mn) <sup>g</sup>	3.760	9.440
Exp. Mn–TiO <sub>2</sub> (0.08 wt% Mn) <sup>g</sup>	3.780	9.428

<sup>a</sup> The lattice constants (*a*, *c*) are in Å.

<sup>b</sup> Computed with the DFT+U method, taken from reference. [174]

<sup>c</sup> Computed with the DFT/PBE method, taken from reference. [175]

<sup>d</sup> Computed with the DFT/B3LYP method, taken from reference. [159]

<sup>e</sup> Experimental data, taken from reference. [91]

<sup>f</sup> Experimental data, taken from reference. [176]

<sup>g</sup> Experimental data, taken from reference. [166]

**Table 6.2** The adsorption energies ( $\Delta E_{\text{ads}}$ ) of gas adsorbed and co-adsorbed on un- and Mn-doped  $\text{TiO}_2$  (001) surfaces.

Adsorbates	$\Delta E_{\text{ads}}^{\text{a}}$			
	$\text{TiO}_2$	Mn- $\text{TiO}_2$		
		V-conf.	I- conf.	perfect conf.
<i>Mono adsorption:</i>				
$\text{O}_2$	-68.13	-102.35	-84.00	<sup>b</sup>
O	-187.70	-216.50 <sup>c</sup>	-216.50 <sup>c</sup>	<sup>b</sup>
CO	-27.19	<sup>b</sup>	<sup>b</sup>	-66.08
CO	<sup>d</sup>	-7.07 <sup>e</sup>	-7.20 <sup>f</sup>	<sup>b</sup>
CO	-6.33 <sup>g</sup>	-5.81 <sup>h</sup>	-2.09 <sup>i</sup>	<sup>b</sup>
<i>Co-adsorption:</i>				
$\text{CO/O}_2^{\text{j}}$	<sup>d</sup>	-109.42 <sup>k</sup>	-91.20	<sup>b</sup>
$\text{CO/O}^{\text{l}}$	-194.03	-222.31	-218.59 <sup>k</sup>	<sup>b</sup>

<sup>a</sup> In kcal/mol.

<sup>b</sup> No adsorption is obtained.

<sup>c</sup> The same configuration.

<sup>d</sup> Unreliable value is obtained.

<sup>e</sup> CO located over the Mn atom of the  $\text{O}_2/\text{Mn-TiO}_2$ .

<sup>f</sup> CO located over the Ti atom of the  $\text{O}_2/\text{Mn-TiO}_2$ .

<sup>g</sup>  $\Delta E_{\text{ads}}$  is defined as  $E(\text{CO/O-slab}) - [E(\text{O-slab}) + E(\text{CO})]$ .

<sup>h</sup> CO located over the Mn atom of the  $\text{O/Mn-TiO}_2$ .

<sup>i</sup> CO located over the Ti atom of the  $\text{O/Mn-TiO}_2$ .

<sup>j</sup>  $\Delta E_{\text{ads}}$  of co-adsorption is defined as  $E(\text{CO/O}_2/\text{slab}) - [E(\text{slab}) + E(\text{O}_2) + E(\text{CO})]$ .

<sup>k</sup> Computed based on a theoretical equation,  $\Delta E_{\text{ads}}(\text{CO/O}_2/\text{slab}) = -\Delta E_{\text{ads}}(\text{CO}/\text{slab}) + \Delta E_{\text{ads}}(\text{O}_2/\text{slab})$ .

<sup>l</sup>  $\Delta E_{\text{ads}}$  of co-adsorption is defined as  $E(\text{CO/O-slab}) - [E(\text{slab}) + E(\text{O}) + E(\text{CO})]$ .

#### 6.4.3.2 Adsorption of CO on the Mn-doped TiO<sub>2</sub> and oxygen-pre-adsorbed Mn-doped TiO<sub>2</sub> surfaces

The adsorption strength of CO adsorbed on the Mn-TiO<sub>2</sub> is obviously much less than the O<sub>2</sub> adsorbed on the Mn-TiO<sub>2</sub>, as shown in **Table 6.2**. Nevertheless, the CO adsorptions on the Mn-TiO<sub>2</sub> are stronger than on the TiO<sub>2</sub> ( $\Delta E_{\text{ads}} = -27.19$  kcal/mol). The CO adsorbs on two different configurations of oxygen molecule-pre-adsorbed Mn-doped TiO<sub>2</sub> surfaces which are O<sub>2</sub><sup>V</sup>/Mn-TiO<sub>2</sub> and O<sub>2</sub><sup>I</sup>/Mn-TiO<sub>2</sub> are quite weak.

The optimized configurations of CO adsorbed on the O<sub>2</sub><sup>V</sup>/Mn-TiO<sub>2</sub> and O<sub>2</sub><sup>I</sup>/Mn-TiO<sub>2</sub> surfaces as CO/O<sub>2</sub><sup>V</sup>/Mn-TiO<sub>2</sub> and CO/O<sub>2</sub><sup>I</sup>/Mn-TiO<sub>2</sub> surfaces of which adsorption energies (-7.07 and -7.20 kcal/mol, respectively) are quite close to each other. It was found that co-absorption energies of CO and O<sub>2</sub> on the Mn-TiO<sub>2</sub> surface as CO/O<sub>2</sub><sup>V</sup>/Mn-TiO<sub>2</sub> and CO/O<sub>2</sub><sup>I</sup>/Mn-TiO<sub>2</sub> configurations are -109.42 and -91.20 kcal/mol, respectively. For the co-absorption energies of CO molecule and O atom on the Mn-TiO<sub>2</sub> surface as CO/O/Mn-TiO<sub>2</sub> and CO'/O/Mn-TiO<sub>2</sub> configurations are -222.31 and -218.59 kcal/mol, respectively.

#### 6.4.4 The mechanism of the CO oxidation by O<sub>2</sub> to CO<sub>2</sub> on the Mn-TiO<sub>2</sub>

The oxidation reaction of CO conversion CO<sub>2</sub> on the Mn-TiO<sub>2</sub> by O<sub>2</sub> was found to be two mechanisms of which are composed of five elementary steps. The preferred mechanism of the CO oxidation by O<sub>2</sub> to CO<sub>2</sub> on the Mn-TiO<sub>2</sub> undertakes via the formation of the O<sub>2</sub><sup>V</sup>/Mn-TiO<sub>2</sub> conformation as the first step of reaction; adsorption energy of O<sub>2</sub> on the Mn-TiO<sub>2</sub> surface of -102.35 kcal/mol was found. The second step, the O<sub>2</sub><sup>V</sup>/Mn-TiO<sub>2</sub> conformation can weakly adsorb CO molecule to form CO/O<sub>2</sub><sup>V</sup>/Mn-TiO<sub>2</sub>, CO + O<sub>2</sub><sup>V</sup>/Mn-TiO<sub>2</sub> → CO/O<sub>2</sub><sup>V</sup>/Mn-TiO<sub>2</sub> of which reaction energy is -7.07 kcal/mol. The CO was found to be located over the Mn atom of the Mn-TiO<sub>2</sub> by pointing its C atom toward Mn atom of which bond distance (OC...Mn) is 2.04 Å.

The bond distance between C atom of CO and nearby O atom of O<sub>2</sub> (OC...O) is 2.44 Å. The third step is to form CO<sub>2</sub> while desorb from the O/Mn–TiO<sub>2</sub> surface which can weakly adsorb the second CO gas to form CO/O/Mn–TiO<sub>2</sub> structure as the fourth step. The last step, the second CO<sub>2</sub> was formed and desorb from the Mn–TiO<sub>2</sub> surface. The energy profile for the oxidation reaction between CO and O<sub>2</sub> to afford CO<sub>2</sub> via the O<sub>2</sub><sup>V</sup>/Mn–TiO<sub>2</sub> conformation is shown in **Figure 6.3**



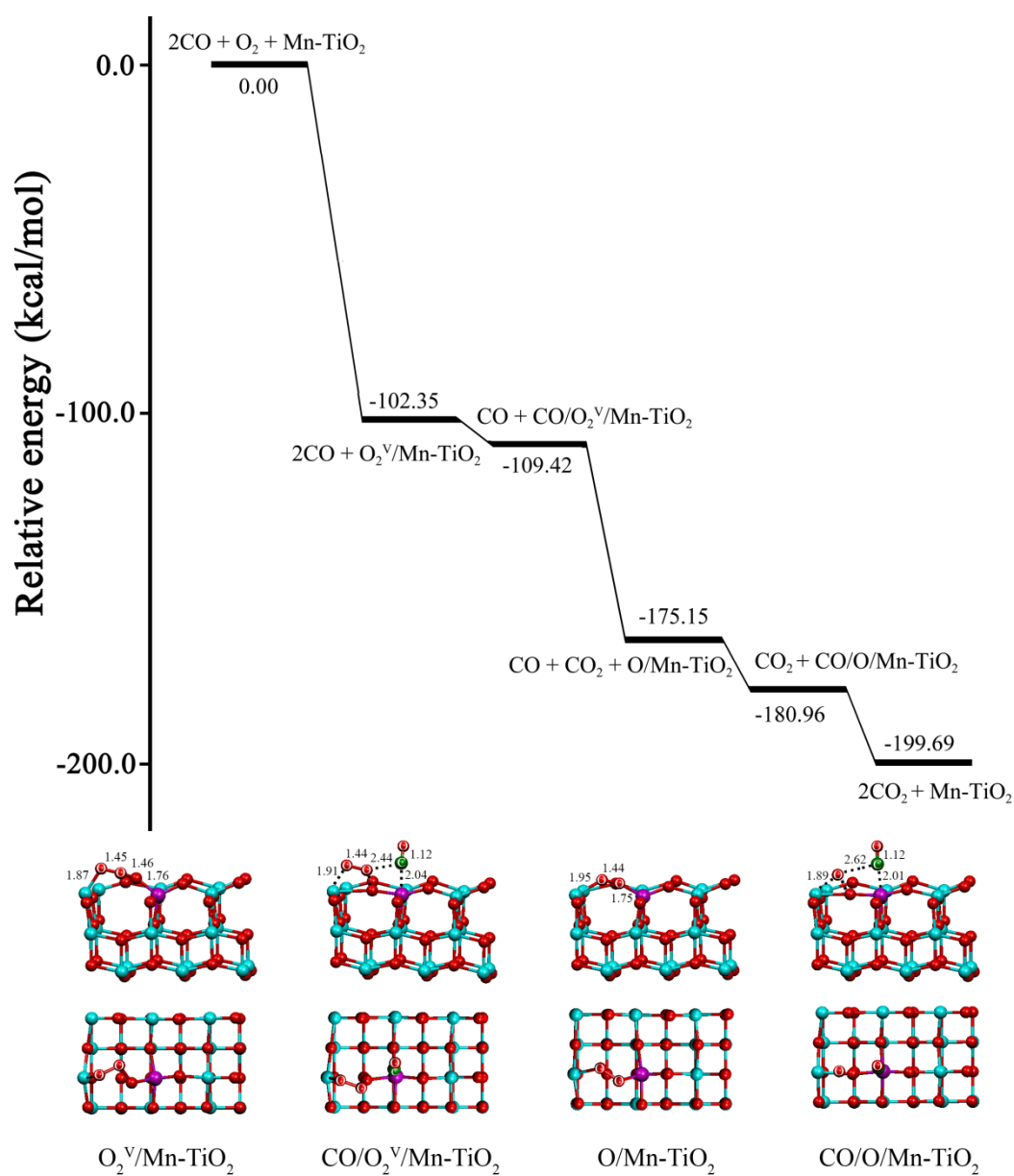


**Figure 6.3** Potential energy profile for CO oxidation to CO<sub>2</sub> on V-shape oxygen-pre-adsorbed on the Mn-TiO<sub>2</sub> (001) (O<sub>2</sub><sup>V</sup>/Mn-TiO<sub>2</sub>). Potential energies are in kcal/mol and bond distances are in Å. Top and side views are shown at the top and bottom images, respectively.

The other mechanism of the CO oxidation by O<sub>2</sub> to CO<sub>2</sub> on the Mn–TiO<sub>2</sub> undertakes via the formation of the O<sub>2</sub><sup>I</sup>/Mn–TiO<sub>2</sub> conformation as the first step of reaction; adsorption energy of O<sub>2</sub> on the Mn–TiO<sub>2</sub> surface of –84.00 kcal/mol was found. The second step, the O<sub>2</sub><sup>I</sup>/Mn–TiO<sub>2</sub> conformation can weakly adsorb CO molecule to form CO/O<sub>2</sub><sup>I</sup>/Mn–TiO<sub>2</sub>, CO + O<sub>2</sub><sup>I</sup>/Mn–TiO<sub>2</sub> → CO/O<sub>2</sub><sup>I</sup>/Mn–TiO<sub>2</sub> of which reaction energy is –7.20 kcal/mol. The CO was found to be located over the Ti atom of the Mn–TiO<sub>2</sub>, which close to the Mn atom, by pointing its C atom toward neighboring Ti atom of which bond distance (OC···Ti) is 2.40 Å. The bond distance between C atom of CO and nearby O atom of O<sub>2</sub> (OC···O) is 2.51 Å. The third step is to form CO<sub>2</sub> while desorb from the O/Mn–TiO<sub>2</sub> surface which can weakly adsorb the second CO gas to form CO'/O/Mn–TiO<sub>2</sub> structure as the fourth step. The last step, the second CO<sub>2</sub> was formed and desorb from the Mn–TiO<sub>2</sub> surface. The energy profile for the oxidation reaction between CO and O<sub>2</sub> to afford CO<sub>2</sub> via the O<sub>2</sub><sup>I</sup>/Mn–TiO<sub>2</sub> conformation is shown in **Figure 6.4**.

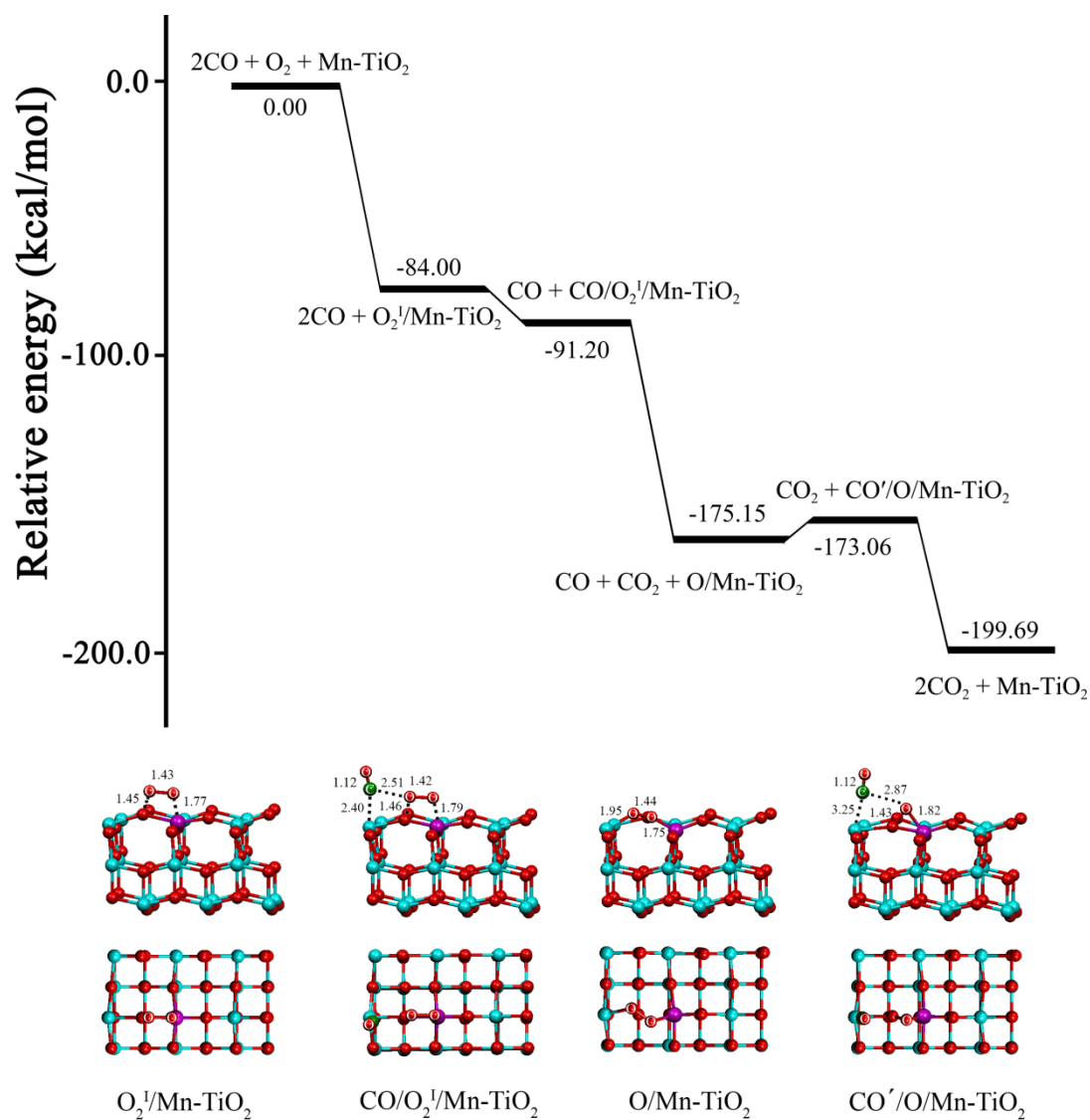


**Figure 6.4** Potential energy profile for CO oxidation to CO<sub>2</sub> on I-shape oxygen-pre-adsorbed on the Mn-TiO<sub>2</sub> (001) (O<sub>2</sub><sup>I</sup>/Mn-TiO<sub>2</sub>). Potential energies are in kcal/mol and bond distances are in Å. Top and side views are shown at the top and bottom images, respectively.

## 6.5 CONCLUSION

The binding energy for Mn bound to  $[\text{TiO}_2+V_{\text{Ti}}]$  and mechanisms of CO oxidation by  $\text{O}_2$  over the Mn-doped  $\text{TiO}_2(001)$  surface to afford  $\text{CO}_2$  was investigated using periodic DFT method. The binding energy for Mn bound to  $[\text{TiO}_2+V_{\text{Ti}}]$ , of  $-750.28$  kcal/mol was obtained. There are two similar mechanisms of different structures of oxygen pre-adsorbed on the Mn-doped  $\text{TiO}_2$  surface were found that are energetically preferred reactions of which overall reaction,  $2\text{CO}+\text{O}_2 \rightarrow 2\text{CO}_2$  and reaction energies ( $-199.69$  kcal/mol) are obtained. The Mn-doped  $\text{TiO}_2(001)$  was therefore suggested to be the efficient catalyst to conversion of CO to  $\text{CO}_2$ .



## CHAPTER VII

### CONCLUSIONS

We have studied the properties of modified anatase  $\text{TiO}_2$  (001). Due to the reason that ZnOSL show strong binding onto anatase  $\text{TiO}_2$  (001) surface, it was immobilized by anatase  $\text{TiO}_2$  (001) surface. Interconversion of  $\text{CO} + \text{O}_2$  to  $\text{CO}_2$  on the ZnOSL-decorated  $\text{TiO}_2$  (001) surface was investigated using periodic DFT computations at the B3LYP level. The reaction mechanism for  $\text{CO}$  to  $\text{CO}_2$  on the ZnOSL of the ZnOSL- $\text{TiO}_2$  is composed of five reaction steps. The stepwise adsorption energies of the first and second  $\text{CO}_2$  adsorptions are  $-5.21$  and  $-2.31$  kcal/mol, respectively. The energy of  $-179.76$  kcal/mol for the reaction of  $2\text{CO} + \text{O}_2$  to  $2\text{CO}_2$  over the ZnOSL was obtained. Moreover, the optimized and electronic structures of doped ZnOSLs by single transition-metal atoms (Sc, Ti, V, Cr, Mn, Fe, Co, Ni, Cu, Pd, Ag, Pt and Au) and single nonmetal atoms (B, C, N, Al, Si, P, Ga and Ge) doped ZnOSL were studied. The binding abilities of these dopants to Zn vacancy for metal doping system and O vacancy for nonmetal doping system are in orders:  $\text{Cr} > \text{Ti} > \text{Sc} > \text{V} > \text{Fe} > \text{Mn} > \text{Ni} > \text{Co} > \text{Pt} > \text{Zn} > \text{Cu} > \text{Pd} > \text{Au} > \text{Ag}$  and  $\text{O} > \text{N} > \text{C} > \text{P} > \text{Si} > \text{Ge} > \text{Ga} > \text{B} > \text{Al}$ , respectively. The Sc-ZnOSL has remarkably lowest energy gap. The adsorption abilities of diatomic gases on the Sc-ZnOSL surface are in the order:  $\text{O}_2/\text{Sc-ZnOSL} > \text{NO}/\text{Sc-ZnOSL} > \text{CO}/\text{Sc-ZnOSL} > \text{N}_2/\text{Sc-ZnOSL} > \text{H}_2/\text{Sc-ZnOSL}$ , respectively. The adsorption abilities of polyatomic gases on the Sc-ZnOSL surface were in the orders:  $\text{SO}_2/\text{Sc-ZnOSL} > \text{N}_2\text{O}/\text{Sc-ZnOSL} > \text{NO}_2/\text{Sc-ZnOSL} > \text{NH}_3/\text{Sc-ZnOSL} > \text{H}_2\text{O}/\text{Sc-ZnOSL} > \text{CO}_2/\text{Sc-ZnOSL}$ , respectively. It was found that the Sc active site is the stronger adsorption site than Zn site. In particular, the  $\text{SO}_2$  is the most preferred adsorbed gas on the Sc-ZnOSL. The most decreasing of energy gap for bridge-structured adsorption of  $\text{N}_2\text{O}$  on Sc-ZnOSL was found. Hence, the Sc-ZnOSL can be used as  $\text{N}_2\text{O}$  or  $\text{SO}_2$  sensing material. Finally, the conversion reaction on Mn-doped  $\text{TiO}_2$  (001) was studied. For Mn-doped  $\text{TiO}_2$  (001),  $\text{Mn}^{4+}$  strongly binds to  $[\text{TiO}_2 + \text{V}_{\text{Ti}}]$  surface because its charge to radius ratio is closely to  $\text{Ti}^4$  on the surface. The Mn-doped  $\text{TiO}_2$  is suggested to be the efficient material for  $\text{CO}$  conversion via oxygen pre-adsorbed. Two similar

mechanisms are energetically preferred reactions of which overall reactions are  $2\text{CO} + \text{O}_2 \rightarrow 2\text{CO}_2$ .

It can be concluded that the adsorption and reaction of small gases can occur on those modified anatase  $\text{TiO}_2$  (001). The doping and supporting modification can enhance the chemical properties of anatase  $\text{TiO}_2$  (001) surfaces. These studies could be useful for sensing and catalysis material application.



## REFERENCES



- [1] T. Jinkawa, G. Sakai, J. Tamaki, N. Miura, N. Yamazoe, Relationship between ethanol gas sensitivity and surface catalytic property of tin oxide sensors modified with acidic or basic oxides, *Journal of Molecular Catalysis A: Chemical*, 155 (2000) 193-200.
- [2] I.D. Kim, A. Rothschild, Nanostructured metal oxide gas sensors prepared by electrospinning, *Polymers for Advanced Technologies*, 22 (2011) 318-325.
- [3] G. Neri, Metal oxide nanostructures for solid state gas sensors: A recent patent survey, *Recent Patents on Materials Science*, 4 (2011) 146-158.
- [4] S.S. Shendage, V.L. Patil, S.A. Vanalakar, S.P. Patil, N.S. Harale, J.L. Bhosale, J.H. Kim, P.S. Patil, Sensitive and selective NO<sub>2</sub> gas sensor based on WO<sub>3</sub> nanoplates, *Sensors and Actuators, B: Chemical*, 240 (2017) 426-433.
- [5] Z.G. Zhao, M. Miyauchi, Nanoporous-walled tungsten oxide nanotubes as highly active visible-light-driven photocatalysts, *Angewandte Chemie - International Edition*, 47 (2008) 7051-7055.
- [6] Y.H. Hu, A highly efficient photocatalyst-hydrogenated black TiO<sub>2</sub> for the photocatalytic splitting of water, *Angewandte Chemie - International Edition*, 51 (2012) 12410-12412.
- [7] M. Batzill, Fundamental aspects of surface engineering of transition metal oxide photocatalysts, *Energy & Environmental Science*, 4 (2011) 3275-3286.
- [8] L. Ke, S.B. Dolmanan, L. Shen, P.K. Pallathadk, Z. Zhang, D.M. Ying Lai, H. Liu, Degradation mechanism of ZnO-based dye-sensitized solar cells, *Solar Energy Materials and Solar Cells*, 94 (2010) 323-326.
- [9] J.M. Matxain, J.M. Mercero, J.E. Fowler, J.M. Ugalde, Electronic excitation energies of ZnO clusters, *Journal of the American Chemical Society*, 125 (2003) 9494-9499.
- [10] S. Kanno, T. Arato, A. Kato, H. Yamashita, S. Azuhata, S. Tamata, Decomposition of CFC113 over TiO<sub>2</sub>-based catalysts, *Nippon Kagaku Kaishi / Chemical Society of Japan - Chemistry and Industrial Chemistry Journal*, (1996) 135.
- [11] X. Chen, S.S. Mao, Titanium Dioxide Nanomaterials: Synthesis, Properties, Modifications, and Applications, *Chemical Reviews*, 107 (2007) 2891-2959.
- [12] A. Wei, L. Pan, W. Huang, Recent progress in the ZnO nanostructure-based sensors, *Materials Science and Engineering B: Solid-State Materials for Advanced Technology*, 176 (2011) 1409-1421.

- [13] M.R. Ranade, A. Navrotsky, H.Z. Zhang, J.F. Banfield, S.H. Elder, A. Zaban, P.H. Borse, S.K. Kulkarni, G.S. Doran, H.J. Whitfield, Energetics of nanocrystalline TiO<sub>2</sub>, Proceedings of the National Academy of Sciences of the United States of America, 99 (2002) 6476-6481.
- [14] A.C. Reber, S.N. Khanna, J.S. Hunjan, M.R. Beltran, Rings, towers, cages of ZnO, European Physical Journal D, 43 (2007) 221-224.
- [15] A.A. Al-Sunaidi, A.A. Sokol, C.R.A. Catlow, S.M. Woodley, Structures of zinc oxide nanoclusters: As found by revolutionary algorithm techniques, Journal of Physical Chemistry C, 112 (2008) 18860-18875.
- [16] B. Wang, S. Nagase, J. Zhao, G. Wang, Structural growth sequences and electronic properties of zinc oxide clusters (ZnO)<sub>n</sub> (n=2-18), Journal of Physical Chemistry C, 111 (2007) 4956-4963.
- [17] S.M. Hosseini, I.A. Sarsari, P. Kameli, H. Salamati, Effect of Ag doping on structural, optical, and photocatalytic properties of ZnO nanoparticles, Journal of Alloys and Compounds, 640 (2015) 408-415.
- [18] Y. Liao, C. Xie, Y. Liu, H. Chen, H. Li, J. Wu, Comparison on photocatalytic degradation of gaseous formaldehyde by TiO<sub>2</sub>, ZnO and their composite, Ceramics International, 38 (2012) 4437-4444.
- [19] E.W. McFarland, H. Metiu, Catalysis by Doped Oxides, Chemical Reviews, 113 (2013) 4391-4427.
- [20] A. Vittadini, M. Casarin, A. Selloni, Chemistry of and on TiO<sub>2</sub>-anatase surfaces by DFT calculations: a partial review, Theoretical Chemistry Accounts, 117 (2007) 663-671.
- [21] M. Sowmiya, K. Senthilkumar, Dissociation of N<sub>2</sub>O on anatase TiO<sub>2</sub> (001) surface – The effect of oxygen vacancy and presence of Ag cluster, Applied Surface Science, 389 (2016) 1220-1232.
- [22] X.-Q. Gong, A. Selloni, Reactivity of Anatase TiO<sub>2</sub> Nanoparticles: The Role of the Minority (001) Surface, The Journal of Physical Chemistry B, 109 (2005) 19560-19562.
- [23] B. Kaewruksa, W. Pipornpong, B. Wannoo, V. Ruangpornvisuti, Density functional studies of small gases adsorbed on the ZnO sodalite-like cage and its adsorption abilities, Computational and Theoretical Chemistry, 1020 (2013) 100-107.
- [24] R. Wanbayor, V. Ruangpornvisuti, Adsorption of di-, tri- and polyatomic gases on the anatase TiO<sub>2</sub> (001) and (101) surfaces and their adsorption abilities, Journal of Molecular Structure: THEOCHEM, 952 (2010) 103-108.

- [25] G. Shukri, W.A. Diño, H.K. Dipojono, M.K. Agusta, H. Kasai, Enhanced molecular adsorption of ethylene on reduced anatase  $\text{TiO}_2$  (0 0 1): Role of surface O-vacancies, *RSC Advances*, 6 (2016) 92241-92251.
- [26] R. Wanbayor, V. Ruangpornvisuti, Adsorption of  $\text{CO}$ ,  $\text{H}_2$ ,  $\text{N}_2\text{O}$ ,  $\text{NH}_3$  and  $\text{CH}_4$  on the anatase  $\text{TiO}_2$  (0 0 1) and (1 0 1) surfaces and their competitive adsorption predicted by periodic DFT calculations, *Materials Chemistry and Physics*, 124 (2010) 720-725.
- [27] W. Pipornpong, V. Ruangpornvisuti, First-principles investigation of ZnO sodalite-like cage binding onto  $\text{TiO}_2$  (001) surface and its ability for CO oxidation to  $\text{CO}_2$ , *Journal of Materials Science*, 49 (2014) 7620-7624.
- [28] W. Pipornpong, B. Kaewruksa, V. Ruangpornvisuti, DFT investigation on molecular structures of metal and nonmetal-doped ZnO sodalite-like cage and their electronic properties, *Structural Chemistry*, 27 (2016) 773-784.
- [29] M. Zhao, Y. Xia, Z. Tan, X. Liu, L. Mei, Design and energetic characterization of ZnO clusters from first-principles calculations, *Physics Letters, Section A: General, Atomic and Solid State Physics*, 372 (2007) 39-43.
- [30] U. Diebold, The surface science of titanium dioxide, *Surface Science Reports*, 48 (2003) 53-229.
- [31] C.J. Howard, T.M. Sabine, F. Dickson, Structural and thermal parameters for rutile and anatase, *Acta Crystallographica Section B*, 47 (1991) 462-468.
- [32] H. Zhang, J. F. Banfield, Thermodynamic analysis of phase stability of nanocrystalline titania, *Journal of Materials Chemistry*, 8 (1998) 2073-2076.
- [33] X. Cheng, F. Li, Y. Zhao, A DFT investigation on ZnO clusters and nanostructures, *Journal of Molecular Structure: THEOCHEM*, 894 (2009) 121-127.
- [34] T. Luttrell, S. Halpegamage, J. Tao, A. Kramer, E. Sutter, M. Batzill, Why is anatase a better photocatalyst than rutile? - Model studies on epitaxial  $\text{TiO}_2$  films, *Scientific Reports*, 4 (2014) 4043.
- [35] M. Lazzeri, A. Vittadini, A. Selloni, Structure and energetics of stoichiometric  $\text{TiO}_2$  anatase surfaces, *Physical Review B*, 63 (2001) 155409.
- [36] F.H. Tian, X. Wang, W. Zhao, L. Zhao, T. Chu, S. Yu, Adsorption of 2-propanol on anatase  $\text{TiO}_2$  (101) and (001) surfaces: A density functional theory study, *Surface Science*, 616 (2013) 76-84.
- [37] X. Han, X. Wang, S. Xie, Q. Kuang, J. Ouyang, Z. Xie, L. Zheng, Carbonate ions-assisted syntheses of anatase  $\text{TiO}_2$  nanoparticles exposed with high energy (001) facets, *RSC Advances*, 2 (2012) 3251-3253.

- [38] D.-N. Pei, L. Gong, A.-Y. Zhang, X. Zhang, J.-J. Chen, Y. Mu, H.-Q. Yu, Defective titanium dioxide single crystals exposed by high-energy {001} facets for efficient oxygen reduction, *Nature Communications*, 6 (2015) 8696.
- [39] L. Liu, Y. Jiang, H. Zhao, J. Chen, J. Cheng, K. Yang, Y. Li, Engineering Coexposed {001} and {101} Facets in Oxygen-Deficient TiO<sub>2</sub> Nanocrystals for Enhanced CO<sub>2</sub> Photoreduction under Visible Light, *ACS Catalysis*, 6 (2016) 1097-1108.
- [40] A. Dmytruk, I. Dmitruk, I. Blonskyy, R. Belosludov, Y. Kawazoe, A. Kasuya, ZnO clusters: Laser ablation production and time-of-flight mass spectroscopic study, *Microelectronics Journal*, 40 (2009) 218-220.
- [41] L. Li, Z. Zhou, X. Wang, W. Huang, Y. He, M. Yang, First-principles study of static polarizability, first and second hyperpolarizabilities of small-sized ZnO clusters, *Physical Chemistry Chemical Physics*, 10 (2008) 6829-6835.
- [42] K.D.D. Gunaratne, C. Berkdemir, C.L. Harmon, A.W. Castleman, Investigating the relative stabilities and electronic properties of small zinc oxide clusters, *Journal of Physical Chemistry A*, 116 (2012) 12429-12437.
- [43] J.S. Chen, Y.L. Tan, C.M. Li, Y.L. Cheah, D. Luan, S. Madhavi, F.Y.C. Boey, L.A. Archer, X.W. Lou, Constructing hierarchical spheres from large ultrathin anatase TiO<sub>2</sub> nanosheets with nearly 100% exposed (001) facets for fast reversible lithium storage, *Journal of the American Chemical Society*, 132 (2010) 6124-6130.
- [44] C.Z. Wen, J.Z. Zhou, H.B. Jiang, Q.H. Hu, S.Z. Qiao, H.G. Yang, Synthesis of micro-sized titanium dioxide nanosheets wholly exposed with high-energy {001} and {100} facets, *Chemical Communications*, 47 (2011) 4400-4402.
- [45] J. Beheshtian, A.A. Peyghan, Z. Bagheri, Adsorption and dissociation of Cl<sub>2</sub> molecule on ZnO nanocluster, *Applied Surface Science*, 258 (2012) 8171-8176.
- [46] N.L. Hadipour, A. Ahmadi Peyghan, H. Soleymanabadi, Theoretical study on the Al-doped ZnO nanoclusters for CO chemical sensors, *Journal of Physical Chemistry C*, 119 (2015) 6398-6404.
- [47] S. Aslanzadeh, Transition metal doped ZnO nanoclusters for carbon monoxide detection: DFT studies, *Journal of Molecular Modeling*, 22 (2016) 160.
- [48] L. Castañeda, Synthesis and characterization of ZnO micro- and nano-cages, *Acta Materialia*, 57 (2009) 1385-1391.
- [49] I.A. Sarsari, S.J. Hashemifar, S. Hadi, First-principles study of ring to cage structural crossover in small ZnO Clusters, *Journal of Physics: Condensed Matter*, 24 (2012) 505502.

- [50] S. Wu, N. Yuan, H. Xu, X. Wang, Z.A. Schelly, Synthesis and bandgap oscillation of uncapped, ZnO clusters by electroporation of vesicles, *Nanotechnology*, 17 (2006) 4713-4718.
- [51] G. Korotcenkov, Gas response control through structural and chemical modification of metal oxide films: state of the art and approaches, *Sensors and Actuators B: Chemical*, 107 (2005) 209-232.
- [52] G. Korotcenkov, Metal oxides for solid-state gas sensors: What determines our choice?, *Materials Science and Engineering: B*, 139 (2007) 1-23.
- [53] A. Cattellani, A. Ruini, G. Cicero, A. Calzolari, First principles description of the electronic properties of doped ZnO, *Physica Status Solidi (B) Basic Research*, 250 (2013) 2106-2109.
- [54] S.A. Siddiqui, M.M. Abdullah, Quantum chemical study of Fe doped ZnO nanoclusters, *Micro and Nanosystems*, 5 (2013) 14-21.
- [55] M.J. Madou, S.R. Morrison, 3 - Solid/Gas Interfaces, in: *Chemical Sensing with Solid State Devices*, Academic Press, San Diego, 1989, pp. 67-104.
- [56] M.J. Madou, S.R. Morrison, 5 - Catalysis Background, in: *Chemical Sensing with Solid State Devices*, Academic Press, San Diego, 1989, pp. 159-196.
- [57] M.J. Madou, S.R. Morrison, 12 - Gas Sensors Based on Semiconductor Powders, in: *Chemical Sensing with Solid State Devices*, Academic Press, San Diego, 1989, pp. 479-516.
- [58] M.J. Gordon, S. Gaur, S. Kelkar, R.M. Baldwin, Low temperature incineration of mixed wastes using bulk metal oxide catalysts, *Catalysis Today*, 28 (1996) 305-317.
- [59] Chapter 4 Surface Coordinative Unsaturation, in: H.K. Harold (Ed.) *Studies in Surface Science and Catalysis*, Elsevier, 1989, pp. 53-71.
- [60] J.H. Kim, X. Li, L.S. Wang, H.L. De Clercq, C.A. Fancher, O.C. Thomas, K.H. Bowen, Vibrationally resolved photoelectron spectroscopy of MgO- and ZnO- and the low-lying electronic states of MgO, MgO-, and ZnO, *Journal of Physical Chemistry A*, 105 (2001) 5709-5718.
- [61] L.M. Kukreja, A. Rohlfing, P. Misra, F. Hillenkamp, K. Dreisewerd, Cluster formation in UV laser ablation plumes of ZnSe and ZnO studied by time-of-flight mass spectrometry, *Applied Physics A: Materials Science and Processing*, 78 (2004) 641-644.
- [62] J.M. Matxain, J.E. Fowler, J.M. Ugalde, Small clusters of II-VI materials:  $Zn_nSi_i$ ,  $i = 1-9$ , *Physical Review A - Atomic, Molecular, and Optical Physics*, 61 (2000) 532011-532018.

- [63] F. Li, C. Zhang, M. Zhao, Magnetic and optical properties of Cu-doped ZnO nanosheet: First-principles calculations, *Physica E: Low-Dimensional Systems and Nanostructures*, 53 (2013) 101-105.
- [64] A. Kaushik, B. Dalela, R. Rathore, V.S. Vats, B.L. Choudhary, P.A. Alvi, S. Kumar, S. Dalela, Influence of Co doping on the structural, optical and magnetic properties of ZnO nanocrystals, *Journal of Alloys and Compounds*, 578 (2013) 328-335.
- [65] A.P. Rambu, L. Ursu, N. Iftimie, V. Nica, M. Dobromir, F. Iacomi, Study on Ni-doped ZnO films as gas sensors, *Applied Surface Science*, 280 (2013) 598-604.
- [66] O.V. Bovgyra, R.V. Bovgyra, M.V. Kovalenko, D.I. Popovych, A.S. Serednytski, The density functional theory study of structural and electrical properties of zno clusters, *Journal of Nano- and Electronic Physics*, 5 (2013).
- [67] J. Ren, H. Zhang, X. Cheng, Electronic and magnetic properties of all 3d transition-metal-doped ZnO monolayers, *International Journal of Quantum Chemistry*, 113 (2013) 2243-2250.
- [68] F.C. Zhang, J.T. Dong, W.H. Zhang, Z.Y. Zhang, Ferromagnetism of V-doped ZnO nanowires, *Chinese Physics B*, 22 (2013).
- [69] H.C. Wu, Y.C. Peng, C.C. Chen, Effects of Ga concentration on electronic and optical properties of Ga-doped ZnO from first principles calculations, *Optical Materials*, 35 (2013) 509-515.
- [70] J. Zhang, K.L. Yao, Z.L. Liu, G.Y. Gao, First principles calculations of Co-doped zinc-blende ZnO magnetic semiconductor, *Physica B: Condensed Matter*, 405 (2010) 1447-1451.
- [71] B.U. Haq, R. Ahmed, A. Afaq, A. Shaari, M. Zarshenas, Structural and electronic properties of Ni-doped ZnO in zinc-blende phase: A DFT investigations, in: *AIP Conference Proceedings*, 2012, pp. 54-57.
- [72] Z. Yin, N. Chen, F. Yang, S. Song, C. Chai, J. Zhong, H. Qian, K. Ibrahim, Structural, magnetic properties and photoemission study of Ni-doped ZnO, *Solid State Communications*, 135 (2005) 430-433.
- [73] X.F. Li, J. Zhang, B. Xu, K.L. Yao, Half-metallic ferromagnetism in Cu-doped zinc-blende ZnO from first principles study, *Journal of Magnetism and Magnetic Materials*, 324 (2012) 584-587.
- [74] Y.F. Chen, Q.G. Song, H.Y. Yan, The electronic structures and magnetic properties of N-doped ZnO with and without Zn vacancy, *Computational and Theoretical Chemistry*, 983 (2012) 65-68.

- [75] Z.Z. Li, Z.Z. Chen, W. Huang, S.H. Chang, X.M. Ma, The transparence comparison of Ga- and Al-doped ZnO thin films, *Applied Surface Science*, 257 (2011) 8486-8489.
- [76] X. Wang, X. Chen, R. Dong, Y. Huang, W. Lu, Ferromagnetism in carbon-doped ZnO films from first-principle study, *Physics Letters, Section A: General, Atomic and Solid State Physics*, 373 (2009) 3091-3096.
- [77] A. Folli, S.B. Campbell, J.A. Anderson, D.E. MacPhee, Role of TiO<sub>2</sub> surface hydration on NO oxidation photo-activity, *Journal of Photochemistry and Photobiology A: Chemistry*, 220 (2011) 85-93.
- [78] J. Ma, H. Wu, Y. Liu, H. He, Photocatalytic removal of NO<sub>x</sub> over visible light responsive oxygen-deficient TiO<sub>2</sub>, *Journal of Physical Chemistry C*, 118 (2014) 7434-7441.
- [79] F. Mazille, A. Lopez, C. Pulgarin, Synergistic effect of TiO<sub>2</sub> and iron oxide supported on fluorocarbon films. Part 2: Long-term stability and influence of reaction parameters on photoactivated degradation of pollutants, *Applied Catalysis B: Environmental*, 90 (2009) 321-329.
- [80] M. Zhang, C. Li, L. Qu, M. Fu, G. Zeng, C. Fan, J. Ma, F. Zhan, Catalytic oxidation of NO with O<sub>2</sub> over FeMnO<sub>x</sub>/ TiO<sub>2</sub>: Effect of iron and manganese oxides loading sequences and the catalytic mechanism study, *Applied Surface Science*, 300 (2014) 58-65.
- [81] M. Liu, X. Qiu, M. Miyauchi, K. Hashimoto, Cu(II) Oxide Amorphous Nanoclusters Grafted Ti<sup>3+</sup> Self-Doped TiO<sub>2</sub>: An Efficient Visible Light Photocatalyst, *Chemistry of Materials*, 23 (2011) 5282-5286.
- [82] H.Y. Kim, H.M. Lee, H. Metiu, Oxidative Dehydrogenation of Methanol to Formaldehyde by a Vanadium Oxide Cluster Supported on Rutile TiO<sub>2</sub>(110): Which Oxygen is Involved?, *The Journal of Physical Chemistry C*, 114 (2010) 13736-13738.
- [83] N.I. Levine, *Quantum Chemistry*, in, University of New York, Prentice Hall, 2000.
- [84] E.G. Lewars, *Computational chemistry: Introduction to the theory and applications of molecular and quantum mechanics*, 2011.
- [85] P. Bera, M.S. Hegde, *Catal. Lett.*, 79 (2002) 75.
- [86] P. Bera, S. Malwadkar, A. Gayena, C.V.V. Satyanarayanab, B.S. Raob, M.S. Hegde, *Catal. Lett.*, 96 (2004) 213.
- [87] P. Bera, K.R. Priolkar, P.R. Sarode, M.S. Hegde, S. Emura, R. Kumashiro, N.P. Lalla, *Chem. Mater.*, 14 (2002) 3591.

- [88] T. Bredow, L. Giordano, F. Cinquini, G. Pacchini, *Phys. Rev. B.*, 70 (2004) 035419.
- [89] T. Bredow, K. Jug, R.A. Evarestov, Electronic and magnetic structure of ScMnO<sub>3</sub>, *Physica Status Solidi (B) Basic Research*, 243 (2006) R10-R12.
- [90] N. Bronsted, *Chem. Rev.*, 5 (1928) 231.
- [91] J.K. Burdett, T. Hughbanks, G.J. Miller, J.W. Richardson, J.V. Smith, Structural-electronic relationships in inorganic solids: powder neutron diffraction studies of the rutile and anatase polymorphs of titanium dioxide at 15 and 295 K, *Journal of the American Chemical Society*, 109 (1987) 3639-3646.
- [92] O.V. Buyevskaya, D. Wolf, M. Baerns, *Catal. Today*, 62 (2000) 91.
- [93] C. Cacho, O. Geiss, J. Barrero-Moreno, V.D. Binas, G. Kiriakidis, L. Botalico, D. Kotzias, Studies on photo-induced NO removal by Mn-doped TiO<sub>2</sub> under indoor-like illumination conditions, *Journal of Photochemistry and Photobiology A: Chemistry*, 222 (2011) 304-306.
- [94] J.T. Calla, R.J. Davis, *J. Phys. Chem. B*, 109 (2005) 2307.
- [95] S.A.C. Carabineiro, A.M.T. Silva, G. Dražić, P.B. Tavares, J.L. Figueiredo, Gold nanoparticles on ceria supports for the oxidation of carbon monoxide, *Catalysis Today*, 154 (2010) 21-30.
- [96] J.L. Carreon-Macedo, J.N. Harvey, *J. Am. Chem. Soc.*, 126 (2004) 5789.
- [97] S. Carrettin, A. Corma, M. Iglesias, F. Sanchez, *Appl. Catal., A*, 291 (2005) 247.
- [98] J.S. Chen, X.W. Lou, *Electrochem. Commun.*, 11 (2009) 2332.
- [99] A.D. Becke, Density-functional thermochemistry. III. The role of exact exchange, *The Journal of Chemical Physics*, 98 (1993) 5648-5652.
- [100] C. Lee, W. Yang, R.G. Parr, Development of the Colle-Salvetti correlation-energy formula into a functional of the electron density, *Physical Review B*, 37 (1988) 785-789.
- [101] J.S. Chen, T. Zhu, C.M. Li, X.W. Lou, *Angew. Chem., Int. Ed.*, 50 (2011) 650.
- [102] S. Chen, J. Duan, M. Jaroniec, S.Z. Qiao, *Angew. Chem., Int. Ed.*, 52 (2013) 13567.
- [103] X. Chen, S. Mao, *Chem. Rev.*, 107 (2007) 2891.

- [104] B. Wang, X. Wang, G. Chen, S. Nagase, J. Zhao, Cage and tube structures of medium-sized zinc oxide clusters  $(\text{ZnO})_n$  ( $n=24, 28, 36,$  and  $48$ ), *Journal of Chemical Physics*, 128 (2008).
- [105] B. Wang, X. Wang, J. Zhao, Atomic structure of the magic  $(\text{ZnO})_{60}$  cluster: First-principles prediction of a sodalite motif for ZnO nanoclusters, *Journal of Physical Chemistry C*, 114 (2010) 5741-5744.
- [106] D.K. Pandey, P.S. Yadav, S. Agrawal, B.K. Agrawal, Structural and electronic properties of ZnO nanoclusters: A B3LYP DFT study, in: *Advanced Materials Research*, 2013, pp. 29-33.
- [107] J. Dai, C. Meng, Q. Li, First-principles study on the magnetism of Mn and Co codoped ZnO, *Physica B: Condensed Matter*, 409 (2013) 5-9.
- [108] Y. Zhang, M.K. Ram, E.K. Stefanakos, D.Y. Goswami, Synthesis, characterization, and applications of ZnO nanowires, *Journal of Nanomaterials*, 2012 (2012).
- [109] N. Kapila, V.K. Jindal, H. Sharma, *J. Phys. Condens. Matt.*, 23 (2011).
- [110] H. Sharma, R. Singh, First-principles investigation into ferromagnetism in C-doped zinc oxide clusters  $(\text{ZnO})_n$ ;  $n = 1-12$ , *International Journal of Nanoscience*, 10 (2011) 577-580.
- [111] A.D. Becke, Density-functional exchange-energy approximation with correct asymptotic behavior, *Physical Review A*, 38 (1988) 3098-3100.
- [112] J.W. Ochterski, *Thermochemistry in Gaussian*, Gaussian, Inc, (2000).
- [113] M.J. Frisch, G.W. Trucks, H.B. Schlegel, G.E. Scuseria, M.A. Robb, J.R. Cheeseman, G. Scalmani, V. Barone, B. Mennucci, G.A. Petersson, H. Nakatsuji, M. Caricato, X. Li, H.P. Hratchian, A.F. Izmaylov, J. Bloino, G. Zheng, J.L. Sonnenberg, M. Hada, M. Ehara, K. Toyota, R. Fukuda, J. Hasegawa, M. Ishida, T. Nakajima, Y. Honda, O. Kitao, H. Nakai, T. Vreven, J.A. Montgomery, J.E. Peralta, F. Ogliaro, M. Bearpark, J.J. Heyd, E. Brothers, K.N. Kudin, V.N. Staroverov, R. Kobayashi, J. Normand, K. Raghavachari, A. Rendell, J.C. Burant, S.S. Iyengar, J. Tomasi, M. Cossi, N. Rega, M.J. Millam, M. Klene, J.E. Knox, J.B. Cross, V. Bakken, C. Adamo, J. Jaramillo, R. Gomperts, R.E. Stratmann, O. Yazyev, A.J. Austin, R. Cammi, C. Pomelli, J.W. Ochterski, R.L. Martin, K. Morokuma, V.G. Zakrzewski, G.A. Voth, P. Salvador, J.J. Dannenberg, S. Dapprich, A.D. Daniels, Ö. Farkas, J.B. Foresman, J.V. Ortiz, J. Cioslowski, D.J. Fox, Gaussian, Inc., Wallingford CT, 2009, Gaussian 09, Revision D.01, Gaussian, Inc Wallingford CT, (2009) 2009.
- [114] P. Flükiger, H.P. Lüthi, S. Portmann, MOLEKEL 43 Swiss center for scientific computing Manno, Switzerland, (2000).

- [115] N.M. O'Boyle, A.L. Tenderholt, K.M. Langner, Cclib: A library for package-independent computational chemistry algorithms, *Journal of Computational Chemistry*, 29 (2008) 839-845.
- [116] H.J. Kim, J.H. Lee, Highly sensitive and selective gas sensors using p-type oxide semiconductors: Overview, *Sensors and Actuators, B: Chemical*, 192 (2014) 607-627.
- [117] S. Das, V. Jayaraman, SnO<sub>2</sub>: A comprehensive review on structures and gas sensors, *Progress in Materials Science*, 66 (2014) 112-255.
- [118] Y. Peng, W. Yu, W. Su, X. Huang, J. Li, An experimental and DFT study of the adsorption and oxidation of NH<sub>3</sub> on a CeO<sub>2</sub> catalyst modified by Fe, Mn, La and Y, *Catalysis Today*, 242, Part B (2015) 300-307.
- [119] X.W. Sun, Y. Yang, ZnO nanostructures and their applications, 2011.
- [120] B.L. Zhu, C.S. Xie, D.W. Zeng, W.L. Song, A.H. Wang, Investigation of gas sensitivity of Sb-doped ZnO nanoparticles, *Materials Chemistry and Physics*, 89 (2005) 148-153.
- [121] N.F. Hamedani, A.R. Mahjoub, A.A. Khodadadi, Y. Mortazavi, Microwave assisted fast synthesis of various ZnO morphologies for selective detection of CO, CH<sub>4</sub> and ethanol, *Sensors and Actuators B: Chemical*, 156 (2011) 737-742.
- [122] J. Eriksson, V. Khranovskyy, F. Söderlind, P.O. Käll, R. Yakimova, A.L. Spetz, ZnO nanoparticles or ZnO films: A comparison of the gas sensing capabilities, *Sensors and Actuators, B: Chemical*, 137 (2009) 94-102.
- [123] L.M. Kukreja, A. Rohlfing, P. Misra, F. Hillenkamp, K. Dreisewerd, Cluster formation in UV laser ablation plumes of ZnSe and ZnO studied by time-of-flight mass spectrometry, *Applied Physics A*, 78 (2004) 641-644.
- [124] H.-p. Chen, J.-n. Ding, N.-y. Yuan, X.-q. Wang, C.-l. Chen, D. Weng, First-principle study of interaction of H<sub>2</sub> and H<sub>2</sub>O molecules with (ZnO)<sub>n</sub> (n=3-6) ring clusters, *Progress in Natural Science: Materials International*, 20 (2010) 30-37.
- [125] D.K. Pandey, P.S. Yadav, S. Agrawal, B.K. Agrawal, Structural and electronic properties of ZnO nanoclusters: A B3LYP DFT study, in: *Advanced Materials Research*, 2013, pp. 29-33.
- [126] H. Zhao, X. Chen, R. Dong, W. Lu, The stability and optical gap of Zinc Oxide clusters (ZnO)<sub>n</sub> (n = 2-18), *Journal of Nanoscience and Nanotechnology*, 12 (2012) 138-142.

- [127] C. Caddeo, G. Mallocci, F. De Angelis, L. Colombo, A. Mattoni, Optoelectronic properties of  $(\text{ZnO})_{60}$  isomers, *Physical Chemistry Chemical Physics*, 14 (2012) 14293-14298.
- [128] A.C. Reber, S.N. Khanna, J.S. Hunjan, M.R. Beltran, Rings, towers, cages of ZnO, *The European Physical Journal D*, 43 (2007) 221-224.
- [129] M. Alberto Flores-Hidalgo, D. Glossman-Mitnik, D.H. Galvan, D. Barraza-Jimenez, Computational study of cage like  $(\text{ZnO})_{12}$  cluster using hybrid and hybrid meta functionals, *Journal of the Chinese Chemical Society*, 60 (2013) 1082-1091.
- [130] B. Wang, X. Wang, J. Zhao, Atomic Structure of the Magic  $(\text{ZnO})_{60}$  Cluster: First-Principles Prediction of a Sodalite Motif for ZnO Nanoclusters, *The Journal of Physical Chemistry C*, 114 (2010) 5741-5744.
- [131] W. Pipornpong, B. Kaewruksa, V. Ruangpornvisuti, DFT investigation on molecular structures of metal and nonmetal-doped ZnO sodalite-like cage and their electronic properties, *Structural Chemistry*, (2015).
- [132] C. Siriwong, C. Liewhiran, N. Wetchakun, S. Phanichphant, Characterization and photocatalytic activity of Pd-doped ZnO nanoparticles synthesized by flame spray pyrolysis, in: 2008 2nd IEEE International Nanoelectronics Conference, INEC 2008, 2008, pp. 869-874.
- [133] O.A. Yildirim, H.E. Unalan, C. Durucan, Highly efficient room temperature synthesis of silver-doped zinc oxide ( $\text{ZnO:Ag}$ ) nanoparticles: Structural, optical, and photocatalytic properties, *Journal of the American Ceramic Society*, 96 (2013) 766-773.
- [134] H.M. Chiu, T.H. Yang, Y.C. Hsueh, T.P. Perng, J.M. Wu, Fabrication and characterization of well-dispersed plasmonic Pt nanoparticles on Ga-doped ZnO nanopagodas array with enhanced photocatalytic activity, *Applied Catalysis B: Environmental*, 163 (2015) 156-166.
- [135] M. Hjiri, L. El Mir, S.G. Leonardi, A. Pistone, L. Mavilia, G. Neri, Al-doped ZnO for highly sensitive CO gas sensors, *Sensors and Actuators B: Chemical*, 196 (2014) 413-420.
- [136] L. Michael, S. Christian, B. Gabriele, B. Tammo, H. Holger, B. Rolf, P. Andreas, S. Daniel, G. Marius, Degenerate interface layers in epitaxial scandium-doped ZnO thin films, *Journal of Physics D: Applied Physics*, 46 (2013) 065311.
- [137] W.R. Wadt, P.J. Hay, Ab initio effective core potentials for molecular calculations. Potentials for main group elements Na to Bi, *The Journal of Chemical Physics*, 82 (1985) 284-298.

- [138] P.J. Hay, W.R. Wadt, Ab initio effective core potentials for molecular calculations. Potentials for K to Au including the outermost core orbitals, *The Journal of Chemical Physics*, 82 (1985) 299-310.
- [139] P.J. Hay, W.R. Wadt, Ab initio effective core potentials for molecular calculations. Potentials for the transition metal atoms Sc to Hg, *The Journal of Chemical Physics*, 82 (1985) 270-283.
- [140] W.J. Hehre, K. Ditchfield, J.A. Pople, Self-consistent molecular orbital methods. XII. Further extensions of gaussian-type basis sets for use in molecular orbital studies of organic molecules, *The Journal of Chemical Physics*, 56 (1972) 2257-2261.
- [141] M.J. Frisch, et al., Gaussian 09, Revision D.01, in, Gaussian, Inc., Wallingford, CT, 2014.
- [142] P.V. Gosavi, R.B. Biniwale, Catalytic preferential oxidation of carbon monoxide over platinum supported on lanthanum ferrite/ceria catalysts for cleaning of hydrogen, *Journal of Power Sources*, 222 (2013) 1-9.
- [143] P. Kast, M. Friedrich, F. Girgsdies, J. Kröhnert, D. Teschner, T. Lunkenbein, M. Behrens, R. Schlögl, Strong metal-support interaction and alloying in Pd/ZnO catalysts for CO oxidation, *Catalysis Today*, 260 (2016) 21-31.
- [144] J.L. Ayastuy, E. Fernández-Puertas, M.P. González-Marcos, M.A. Gutiérrez-Ortiz, Transition metal promoters in CuO/CeO<sub>2</sub> catalysts for CO removal from hydrogen streams, *International Journal of Hydrogen Energy*, 37 (2012) 7385-7397.
- [145] G. Dong, J. Wang, Y. Gao, S. Chen, A novel catalyst for CO oxidation at low temperature, *Catalysis Letters*, 58 (1999) 37-41.
- [146] Y.H. Kim, E.D. Park, H.C. Lee, D. Lee, Selective CO removal in a H<sub>2</sub>-rich stream over supported Ru catalysts for the polymer electrolyte membrane fuel cell (PEMFC), *Applied Catalysis A: General*, 366 (2009) 363-369.
- [147] S. Ching, D.A. Kriz, K.M. Luthy, E.C. Njagi, S.L. Suib, Self-assembly of manganese oxide nanoparticles and hollow spheres. Catalytic activity in carbon monoxide oxidation, *Chemical Communications*, 47 (2011) 8286-8288.
- [148] N.D. Ivanova, S.V. Ivanov, E.I. Boldyrev, G.V. Sokol'skii, I.S. Makeeva, High-performance manganese oxide catalysts for CO oxidation, *Russian Journal of Applied Chemistry*, 75 (2002) 1420-1423.
- [149] U.R. Pillai, S. Deevi, Room temperature oxidation of carbon monoxide over copper oxide catalyst, *Applied Catalysis B: Environmental*, 64 (2006) 146-151.

- [150] P.J. Møller, S.A. Komolov, E.F. Lazneva, E.H. Pedersen, CO<sub>2</sub> - intermediates in the CO/ZnO(0001) interface, *Surface Science*, 323 (1995) 102-108.
- [151] M. Ferus, L. Kavan, M. Zukulová, A. Zukal, M. Klementová, S. Civiš, Spontaneous and Photoinduced Conversion of CO<sub>2</sub> on TiO<sub>2</sub> Anatase (001)/(101) Surfaces, *The Journal of Physical Chemistry C*, 118 (2014) 26845-26850.
- [152] W. Pipornpong, R. Wanbayor, V. Ruangpornvisuti, Adsorption CO<sub>2</sub> on the perfect and oxygen vacancy defect surfaces of anatase TiO<sub>2</sub> and its photocatalytic mechanism of conversion to CO, *Applied Surface Science*, 257 (2011) 10322-10328.
- [153] R. Wanbayor, P. Deák, T. Frauenheim, V. Ruangpornvisuti, First principles theoretical study of the hole-assisted conversion of CO to CO<sub>2</sub> on the anatase TiO<sub>2</sub>(101) surface, *Journal of Chemical Physics*, 134 (2011).
- [154] H.Y. Kim, H.M. Lee, R.G.S. Pala, V. Shapovalov, H. Metiu, CO Oxidation by Rutile TiO<sub>2</sub>(110) Doped with V, W, Cr, Mo, and Mn, *The Journal of Physical Chemistry C*, 112 (2008) 12398-12408.
- [155] T. Sun, Y. Wang, H. Zhang, P. Liu, H. Zhao, Adsorption and oxidation of oxalic acid on anatase TiO<sub>2</sub> (0 0 1) surface: A density functional theory study, *Journal of Colloid and Interface Science*, 454 (2015) 180-186.
- [156] X.H. Yang, Z. Li, C. Sun, H.G. Yang, C. Li, Hydrothermal stability of {001} faceted anatase TiO<sub>2</sub>, *Chemistry of Materials*, 23 (2011) 3486-3494.
- [157] A. Vittadini, A. Selloni, F.P. Rotzinger, M. Grätzel, Structure and energetics of water adsorbed at TiO<sub>2</sub> anatase (101) and (001) surfaces, *Physical Review Letters*, 81 (1998) 2954-2957.
- [158] H.G. Yang, C.H. Sun, S.Z. Qiao, J. Zou, G. Liu, S.C. Smith, H.M. Cheng, G.Q. Lu, Anatase TiO<sub>2</sub> single crystals with a large percentage of reactive facets, *Nature*, 453 (2008) 638-641.
- [159] R. Wanbayor, V. Ruangpornvisuti, A periodic DFT study on binding of Pd, Pt and Au on the anatase TiO<sub>2</sub> (0 0 1) surface and adsorption of CO on the TiO<sub>2</sub> surface-supported Pd, Pt and Au, *Applied Surface Science*, 258 (2012) 3298-3301.
- [160] E. Escamilla-Roa, V. Timón, A. Hernández-Laguna, DFT study of the adsorption of Ni on Anatase (0 0 1) surface, *Computational and Theoretical Chemistry*, 981 (2012) 59-67.
- [161] T. Ye, S. Li, X. Wu, M. Xu, X. Wei, K. Wang, H. Bao, J. Wang, J. Chen, Sol-gel preparation of efficient red phosphor Mg<sub>2</sub>TiO<sub>4</sub>:Mn<sup>4+</sup> and XAFS investigation on the substitution of Mn<sup>4+</sup> for Ti<sup>4+</sup>, *Journal of Materials Chemistry C*, 1 (2013) 4327-4333.

- [162] K.S. Siddhapara, D.V. Shah, Study of photocatalytic activity and properties of transition metal ions doped nanocrystalline TiO<sub>2</sub> prepared by sol-gel method, *Advances in Materials Science and Engineering*, 2014 (2014).
- [163] L. Wang, J. Fan, Z. Cao, Y. Zheng, Z. Yao, G. Shao, J. Hu, Fabrication of predominantly Mn<sup>4+</sup>-Doped TiO<sub>2</sub> nanoparticles under equilibrium conditions and their application as visible-light photocatalysts, *Chemistry - An Asian Journal*, 9 (2014) 1904-1912.
- [164] L. Wang, X. Zhang, P. Zhang, Z. Cao, J. Hu, Photoelectric conversion performances of Mn doped TiO<sub>2</sub> under 420 nm visible light irradiation, *Journal of Saudi Chemical Society*, 19 (2015) 595-601.
- [165] M.-V. Sofianou, M. Tassi, V. Psycharis, N. Boukos, S. Thanos, T. Vaimakis, J. Yu, C. Trapalis, Solvothermal synthesis and photocatalytic performance of Mn<sup>4+</sup>-doped anatase nanoplates with exposed {0 0 1} facets, *Applied Catalysis B: Environmental*, 162 (2015) 27-33.
- [166] A.K. Tripathi, M.C. Mathpal, P. Kumar, M.K. Singh, M.A.G. Soler, A. Agarwal, Structural, optical and photoconductivity of Sn and Mn doped TiO<sub>2</sub> nanoparticles, *Journal of Alloys and Compounds*, 622 (2015) 37-47.
- [167] K.Z. Hedjazi, R.; Cui, R.; Liu, N.; Chen, B., Synthesis of TiO<sub>2</sub> with diverse morphologies as supports of manganese catalysts for CO oxidation, *Appl Petrochem Res*, 6 (2016) 89-96.
- [168] R. Dovesi, R. Orlando, B. Civalleri, C. Roetti, V.R. Saunders, C.M. Zicovich-Wilson, CRYSTAL: A computational tool for the ab initio study of the electronic properties of crystals, *Zeitschrift fur Kristallographie*, 220 (2005) 571-573.
- [169] S. Piskunov, E. Heifets, R.I. Eglitis, G. Borstel, Bulk properties and electronic structure of SrTiO<sub>3</sub>, BaTiO<sub>3</sub>, PbTiO<sub>3</sub> perovskites: An ab initio HF/DFT study, *Computational Materials Science*, 29 (2004) 165-178.
- [170] M.F. Peintinger, D.V. Oliveira, T. Bredow, Consistent Gaussian basis sets of triple-zeta valence with polarization quality for solid-state calculations, *Journal of Computational Chemistry*, 34 (2013) 451-459.
- [171] Y.F. Zhao, C. Li, S. Lu, R.X. Liu, J.Y. Hu, Y.Y. Gong, L.Y. Niu, Electronic, optical and photocatalytic behavior of Mn, N doped and co-doped TiO<sub>2</sub>: Experiment and simulation, *Journal of Solid State Chemistry*, 235 (2016) 160-168.
- [172] A. Selloni, Crystal growth: Anatase shows its reactive side, *Nature Materials*, 7 (2008) 613-615.

[173] M. Lazzeri, A. Vittadini, A. Selloni, Erratum: Structure and energetics of stoichiometric TiO<sub>2</sub> anatase surfaces (Physical Review B (2001) 63 (155409)), Physical Review B - Condensed Matter and Materials Physics, 65 (2002) 1199011.

[174] D. Ren, H. Li, X. Cheng, Tailoring the electronic and optical properties of anatase TiO<sub>2</sub> by (S, Nb) co-doping from a DFT plus U calculation, Solid State Communications.

[175] N.H. Linh, T.Q. Nguyen, W.A. Diño, H. Kasai, Effect of oxygen vacancy on the adsorption of O<sub>2</sub> on anatase TiO<sub>2</sub>(001): A DFT-based study, Surface Science, 633 (2015) 38-45.

[176] M.V. Sofianou, M. Tassi, V. Psycharis, N. Boukos, S. Thanos, T. Vaimakis, J. Yu, C. Trapalis, Solvothermal synthesis and photocatalytic performance of Mn<sup>4+</sup>-doped anatase nanoplates with exposed {001} facets, Applied Catalysis B: Environmental, 162 (2015) 27-33.



## VITA

### PERSONAL DATA

Name Waranyu Pipornpong

Date of birth 23 April 1988

E-mail waranyu.lab@gmail.com

### ACADEMIC EDUCATION AND SCHOLARSHIP

2011 - 2017 Ph.D. in Physical chemistry, Chulalongkorn University.

2010 B.Sc., Chulalongkorn University.

2004 – 2006 The Promotion of Academic Olympiads and Development of Science Education Foundation under the Patronage of Her Royal Highness Princess Galyani Vadhana Krom Luang Naradhiwas Rajanagarindra

### ACADEMIC EXPERIENCES

2012 Short-term research visitor scholarship at Japan Advanced Institute of Science and Technology (JAIST) from Japan Student Services Organization (JASSO)

2016 Presentation at the PACCON 2016, Thailand

2016 Presentation at the E-MRS 2016 Spring Meeting, France

2016 Short-term research visitor scholarship at Nanyang Technological University (NTU)

2017 Short-term research visitor at Department of Materials science, University of Milano-Bicocca (UNIMIB)

### REWARD

2010 Best Bachelor's research from Department of Chemistry, Faculty of Science, Chulalongkorn University

